The Institute of Space and Astronautical Science
Report No. 672, March 1999

A Measurement of Vibrational - Rotational Temperature and Density of Molecular Nitrogen in the Upper Atmosphere by Rocket-Borne Electron Beam Induced Luminescence

By

Takahiro KAWASHIMA*, Kohichiro OYAMA**
and Katsuhisa SUZUKI***

(October 22, 1998)

ABSTRACT: The vibrational temperature, the rotational temperature and the density of atmospheric molecular nitrogen in the lower thermosphere between 100 - 150 km were measured in situ by a sounding rocket S-310-24, over Uchinoura, Kagoshima, Japan, at 20:00 JST on February 11, 1996. Molecular nitrogen was first ionized using an electron gun and the emission of the first negative band of ionized molecular nitrogen in the wavelength range of 356nm - 442nm was measured by a sensitive spectrometer. To analyze the spectra obtained in the rocket experiment, the synthetic spectra were calculated for the resolution of the rocket instrument and fitted to spectra data for various rotational temperature and vibrational temperature by non-linear square method. The number density was deduced from intensities of rocket spectra. The descending ionized intermediate layer was also observed at 135 - 140km on rocket ascent by the impedance probe which simultaneously is borne on the rocket.

Observed vibrational temperature was determined to be 400K with upper limit of 800K at 100km, 800K with upper limit of 1000K at 130km and 1000K with upper limit of 2000K at 150km.

Observed rotational temperature showed the sinusoidal structure in altitude, whose vertical wavelength was about 50 km. Difference in the amplitude of the height varying temperature from kinetic temperature of MSIS model was about 100K. Number density showed fine vertical structure with the vertical wavelength of 5-20km superimposed on major sinusoidal structure in altitude whose major vertical wavelength was about 50km. These large-scale perturbation was probably induced by a semidiurnal tidal wind. For this wind field, the altitude profile of temperature was calculated using the conservation law of the potential temperature, and the altitude profile of ion density was also calculated using by the continuity equation. Numerical results showed the observed altitude profile of the number density , rotational temperature of molecular nitrogen, and ion density could be explained consistently by the same wind field mentioned above.

* Institute of Space and Astronautical Science, Yoshinodai, Kanagawa, Japan (Now at NEC Corporation, Yokohama, Kanagawa, Japan)
** Institute of Space and Astronautical Science, Yoshinodai, Kanagawa, Japan
*** Yokohama National University, Hodogaya, Yokohama, Japan

I GENERAL INTRODUCTION AND HISTORICAL REVIEW

I-1 Temperature in the Lower Thermosphere

Lower thermosphere, the altitude region between 90 and 150km is very important for understanding the structure of the thermosphere, because the energy input from outer space comes into contact with energy flow from lower atmosphere. Figure 1-1 shows temperature in the lower thermosphere. The solid line in Figure 1-1 is obtained from Mass Spectrometer Incoherent Scatter (MSIS86) model [Hedin, 1987] at 20:00 LT at the period of solar minimum. There is steep temperature gradient in this region since radiative cooling mainly from CO_2, NO, O_3 and O infrared emissions is occurring at lower altitude and heating is occurring throughout the ionosphere by the absorption of solar UV and EUV radiation, Joule dissipation of ionospheric currents, release of chemical energy and dissipation of wave disturbances propagating upward from the lower atmosphere. Temperature in the lower thermosphere is usually inferred from models such as MSIS because of difficulty of the direct measurement . But MSIS model describes only average state of the atmosphere and does not explain disturbed state such as temperature fluctuation induced by the tidal wave or by the internal gravity wave. Ion temperature measurement is one of the most common method to infer the neutral temperature because the ion-neutral collision frequency being 10 - 10^4 Hz in the altitude of 100 - 150km is high enough to realize equilibrium between ion and neutral temperatures. Another useful method to infer the kinetic temperature is measurement of rotational temperature of molecules by the vibrational - rotational band spectrum over this altitudes where the collision frequency is sufficiently large to be in translational - rotational equilibrium as shown in Figure 1-2. As an example in the case of molecular nitrogen, rotational - translational exchange processes require time of the order of 10 collisions to reach equilibration. The characteristic that the rotational temperature is free from Joule heating induced by electromagnetic field in the thermosphere has more advantage in determining the neutral kinetic temperature rather than ion temperature in spite of lower rotational - kinetic collision frequency than ion - neutral collision frequency by 1/10. On the contrary to rotational temperature,

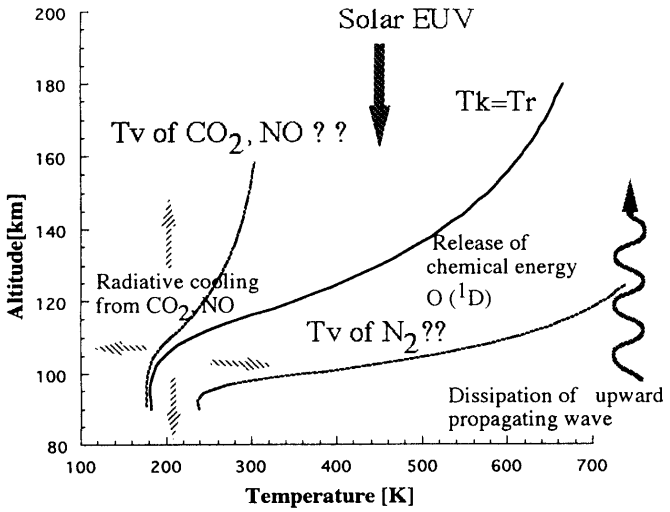

Fig. 1-1: Schematic representation of the thermal sturucture in the lower thermosphere
The solid line indicates Tk Kinetic temperature from MSIS86 model.
Tv and Tr means Vibrational temperature and Rotational temperature respectively.

the fact that relaxation time between translation - vibration energy exchange is significantly larger than that of translational - translational energy exchange suggests the vibration temperature is far from local thermal equilibrium (LTE). In the case of infrared active molecules such as CO_2 and NO, their vibrational temperature are significantly lower than kinetic temperature by radiative cooling when collisions between molecules are infrequent enough that the radiative lifetimes of the vibrational energy states of a molecule become comparable to the mean time between collisions. This arises above 70km in the case of 15μm of CO_2 [Lopes-Puertas, 1986]. In the case of N_2, the generally slow nature of the reactions in which vibrational quanta are lost from the homonuclear infrared inactive molecules has resulted in several estimates [Walker,1968; Harris, 1983; Pavlov, 1994] that nitrogen vibrational temperature may significantly exceed the kinetic temperature at altitudes greater than 100km. The relaxation time of translation - vibration energy exchange for N_2 is 10^3 - 10^4 sec as shown in Figure 1-2. These vibrational temperatures expected from theoretical works are indicated in Figure 1-1 by dashed lines.

I-2 Historical Review of Vibrationally Excited Molecular Nitrogen in the Upper Atmosphere

Impact on the Ionosphere Physics and Chemistry

The role of vibrationally excited molecular nitrogen in the upper atmosphere is important in thinking of the both energy budget of the thermosphere and electron temperature and density in the ionosphere. But the question of whether the vibrational temperature of N_2 is enhanced over kinetic thermospheric temperature has not been conclusively answered. In the lower E region, electron temperature higher than neutral kinetic temperature have been occasionally observed by rocket experiments [Oyama et al. 1980, Oyama et al., 1983, Amemiya et al. 1985, Oyama and Hirao,1985].

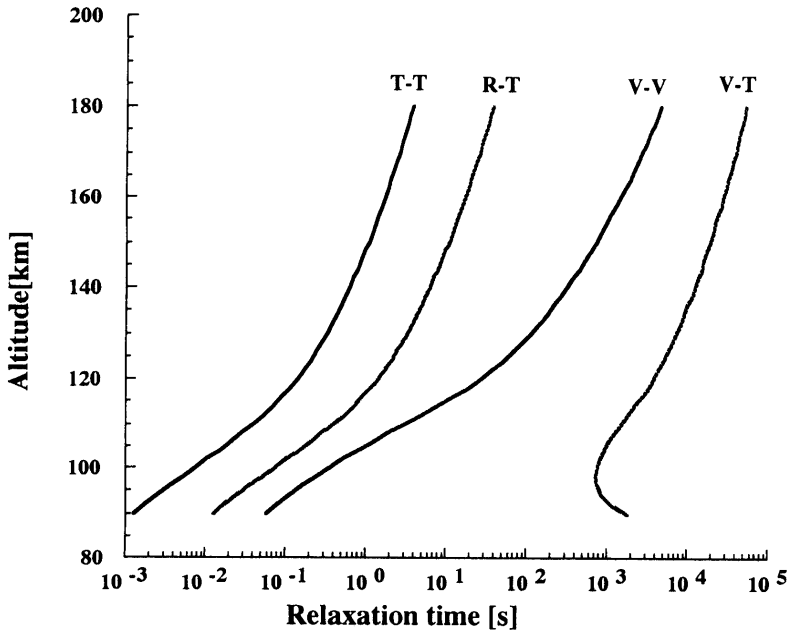

Fig. 1-2: Relaxation time[s] for each energy exchange collision process for molecular nitrogen. T: Translation, V: Vibration, R:Rotation. R-T means Rotational - Translational energy exchange process and so on.

In earlier studies, Walker[1968] , Walker et al. [1969], Kummler and Bortner [1972], and Newton et al. [1974] have all inferred higher vibrational temperatures for N_2 than neutral kinetic temperature which could seriously affect the cooling rate of thermal electrons. Walker [1968] invoked vibrationally excited N_2 as a source of heat to explain observations of elevated electron temperatures in the E region. Walker et al.[1969] pointed out that the exothermic energy stored in the quenching of metastable atomic oxygen $O(^1D)$ by N_2, that is,

$$O(^1D) + N_2 \rightarrow O(^3P) + N_2^* \quad (1\text{-}1)$$

could potentially provide a major source of N_2^*. They conclude that if the bulk of the exothermic energy of the reaction were transferred to N_2^*, with vibrational temperatures as large at 3000K being possible at higher altitudes in the absence of significant quenching. His result is shown in Figure 1-3 in the case of all the $O(^1D)$ energy transfered into vibrational energy of N_2. Several groups [e.g, Slanger and Black, 1974] have determined that the yield of N_2^* from reaction (1-1) is $\sim$30%. Harris and Adams [1983] described approximately 25% of the total $O(^1D)$ energy is transferred into vibrationally excited N_2. Other sources of vibrationally excited N_2 in the thermosphere include photoelectron impact and chemical reactions

$$e + N_2 \rightarrow e + N_2^* \quad (1\text{-}2)$$

$$N + NO \rightarrow N_2^* + O \quad (1\text{-}3)$$

As for the reaction (1-2), transfer of thermal electron energy to N_2 occurs through a shape resonance process for electrons in the tail of the electron distribution between 2 and 4eV in energy. Lee et al.[1980] analyzed the ambient photoelectron spectrum below 300km for the data of AE-E satellite, and described the N_2 vibration - rotation excitation dip at 2.3eV is strongest of the lowest altitudes in the measurement and decreases with increasing altitude. Richards et al. [1986a] have shown that under conditions of enhanced electron densities and low electron temperature, the rate of energy

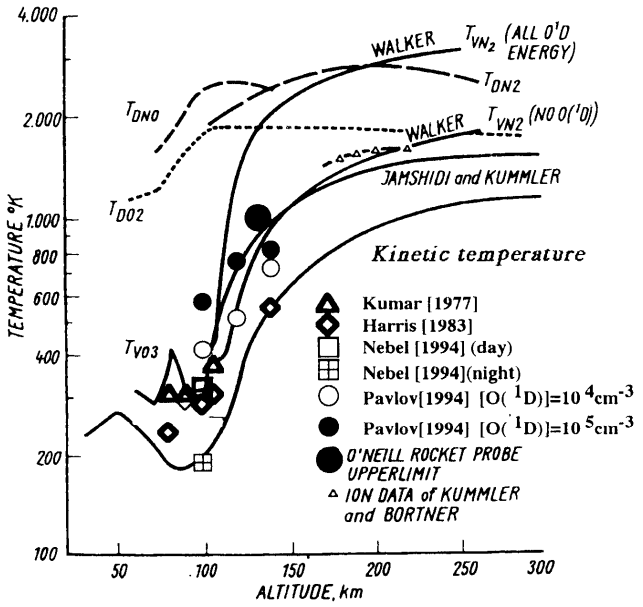

Fig. 1-3: Summary of vibrational temperatures mentioned in the text (Modified from Kummler and Bortner, 1972).

transfer from thermal electrons to N_2 is greatly reduced and even reversed. They stated the enhanced vibrational excitation of N_2 increases the electron temperature by about 100K throughout the F region ionosphere at solar minimum.

If indeed vibrational temperature is high, there might be an impact on the photochemistry via the temperature dependence of reaction rate coefficients for processes involving interactions with N_2*[Schmeltekopf et al, 1967].

$$O^+ + N_2^* \rightarrow NO^+ + N \quad (1\text{-}4)$$

They found that the rate coefficient varies with vibrational temperature in much the same way as the reaction of O^+ with ground state N_2 varies with kinetic temperature. Thus the presence of significant amounts of N_2* in the thermosphere would increase the loss rate of O^+ via this process. As the recombination coefficient for NO^+ is $4.2\times10^{-7}(T_e/300)^{-0.85}$ [cm^3s^{-1}] by Rees [1987] , which is much larger than the recombination coefficient for O^+ of $3\times10^{-12}(T/300)^{-0.7}$ [cm^3s^{-1}], enhanced vibrational temperature results in less the electron density in the ionosphere. This aspect was examined for stable auroral red (SAR) arc conditions by Newton et al. [1974], who expanded the earlier models of the vibrational population for levels $v< 5$. They concluded that under SAR arc conditions, that is, enhanced electron temperatures, sufficient N_2* is produced to have a significant impact on the ion-atom interchange reaction (1-4) of O^+ with N_2. Richards and Torr [1986b] obtained N_2 vibrational populations by solving the time-dependent continuity and momentum equations for the ground vibrational level and the first five vibrationally excited levels. They stated that vibrational excitation of nitrogen molecules is an important factor in the O^+ chemistry of the ionospheric F region at solar maximum. The high electron temperature possible at solar maximum can produce sufficient amounts of vibrational nitrogen through reaction (1-2) so as to cause a factor of two reduction in the peak O^+ density in summer at L = 2.4. Walker [1968] and Walker et al. [1969] initially concluded that loss of N_2 vibrational quanta by collisional quenching would only be significant below $\sim$120km. They deduced that the major quenching species at this altitude would be CO_2 and that quenching by O and O_2 would not be important, because N_2^* dose not radiate in the infrared and hence must be quenched or react with infrared active gases such as CO_2 or NO in order to lose its vibrational energy.

$$N_2^* + CO_2 \rightarrow N_2 + CO_2 \quad (1\text{-}5)$$

$$N_2^* + O \rightarrow N_2 + O \quad (1\text{-}6)$$

$$N_2^* + O_2 \rightarrow N_2 + O_2 \quad (1\text{-}7)$$

However, high vibrational temperature of N_2 is not realized if the quenching rate of vibrationally excited N_2 by atomic oxygen is greatly enhanced. In Figure 1-2, the relaxation time of translation - vibration of N_2 is obtained by

$$\tau_{VT} = (k_1[O]+k_2[O_2])^{-1}$$

Where k_1 is the reaction rate coefficient for quenching by O, determined to be 3.5×10^{-15} $cm^3\ s^{-1}$ at 270K by McNeal et al. [1974]. Breig et al. [1973] showed that with this value, O quenching would be significant between 120 and 200km. Reaction (1-7) with the rate coefficient $k_2 \sim 2.0\times10^{-18}$ $cm^3\ s^{-1}$ by Taylor and Bitterman [1969] is yet not important. Walker et al. [1969] examined the production, loss, and diffusion terms in the continuity equation for N_2* but were unable to determine whether high vibrational temperatures could be expected. However, the calculation are no longer valid in the light of the information that oxygen is indeed an important quencher. While both Walker et al. [1969] and Kummler and Bortner [1972] found that electron quenching would be important above 400km.

Recent Calculation of Vibrational Temperature of Molecular Nitrogen

From the point of energy budget, N_2^* is important as a sink of $O(^1D)$ which is significant heating source in the region 60 -150km described in Reaction (1-1) and as a source of vibrational excited CO_2 state radiating infrared 4.3 μm emission which is a significant cooling mechanism in the same region.

Therefore many researchers calculated N_2 vibrational temperature together with that of CO_2 from the concern of the energy budget in the mesosphere and the lower thermosphere. Reaction (1-5) is quick because the N_2 first vibrational excitation energy of 0.2886eV is very near the CO_2 asymmetric stretching mode excitation energy of 0.2908eV. Thus this system may be near-resonant system as will be described by (1-5)', rather than (1-5).

$$N_2^* + CO_2 \rightleftarrows N_2 + CO_2^* \qquad (1\text{-}5)'$$

The rate constant for (1-5)' of 6×10^{-13} [cm^3s^{-1}] for 300K[Pavlov, 1987 ; Nebel et al., 1994] is large enough that the process is a determining factor for the vibrational populations of both N_2 and CO_2 which therefore cannot be calculated independently. Kumar[1977] was the first who included the system in calculating vibrational temperaure (Tv) of N_2. The results are 307.8K at 81.1km, 308K at 90.2km and 371.3K at 107km. But no accounting of the $O(^1D)$ energy is available from their work. Harris and Adams [1983] researched the fractional thermalization of the $O(^1D)$ energy by following it through its various paths, including the multiple-photon processes involved in the coupled N_2^* - CO_2^* - 4.3 μm system. They determined the Tv values to be 234K at 80km, 285K at 100km and 550K at 140km. Nebel [1994] calculated vibrational temperature of N_2 and CO_2 asymmetric stretching mode and resulting 4.3 μm limb radiance using a line-by-line radiative transfer model and compared with 4.3 μm earthlimb radiance data obtained by the rocket experiment. Vibrational temperature of N_2 at night was calculated to be 190K at 100km in their work, which was equal to kinetic temperature. But its value was 320K at daytime, significantly larger than kinetic temperature, because of the excitation of CO_2 asymmetric stretching mode by solar pumping . Pavlov [1988a] described modern calculation of the vibrational distribution including collisions with excited oxygen atoms $O(^1D)$ as shown in Reaction (1-1), exthothermal reaction between N and NO as shown in Reaction (1-3), vibrational - translational energy exchange in collisions with oxygen atoms and molecules as shown in Reaction (1-6) and (1-7), vibrational - vibrational energy exchange between N_2^* molecules, intermode exchange of vibrational energy with CO_2 molecules as shown in Reaction (1-5)' and N_2^* transport processes. In this frame-work, Pavlov [1994b] calculated Tv of N_2 for 12LT on day 90 of a year with geomagnetic index Ap=10 at the latitude and longitude of Moscow and for medium solar activity (F10.7 = 150). The kinetic temperature of neutral atmosphere under this condition is 194.6K at 100km, 377.3K at 120km and 648.9K at 140km. The results were Tv=415K at 100km ,517K at 120km and 732K at 140km in the case of $[O(^1D)]=10^4\ cm^{-3}$, and Tv= 581K at 100km, 765K at 120km and 825K at 140km for $[O(^1D)]=10^5\ cm^{-3}$. The deviation from LTE is significant in the lower E region , the difference (T_v - T_k) reaches almost 200-300K. Figure 1-3 shows summary of the calculated vibrational temperature mentioned above overplotted on a reproduced figure from Kummler and Botrner [1972]

I-3 Measurement of Various Temperature in the Upper Atmosphere

Ion Temperature Measurement

Ion temperature measurement by Incoherent Scatter (IS) is useful to measure time varying ion temperature in local time. Tidal and gravity wave play a outstanding role for temperatures in the lower thermosphere. It is shown that waves of tidal type are present in the lower thermosphere, with dominant periods of 24 and 12 hr. The typical vertical wavelength is 20km and temperature amplitude is about several tens Kelvin. [Fontarani and Alcayde,1974; Wand,1976; Harper,1981] In situ measurements of ion temperature by the sounding rocket were done by many researchers. Knusen and Sharp [1965] have observed a wavelike variation of the ion temperature with altitude similar to the neutral temperature expected in a gravity wave. Minami and Takeya[1982] have obtained vertical ion temperature profile in the region from 95 to 310km by means of retarding potential analyzer which agreed with neutral temperature above 120km and also showed an oscillation of the temperature in

altitude with the vertical wavelength of about 25km.

Vibrational and Rotational Temperature Measurement on the Ground

As N_2^+ 1st Negative Band emission dominates the blue spectral region in the dayglow and in the aurora, many researchers obtained vibrational temperature from the dayglow spectrum or the auroral spectrum. Auroral observations [Hunten and Shepherd, 1955; Broadfoot, 1967] found that auroras do not show high nitrogen vibrational temperature, presumably because of fast quenching by atomic oxygen. A study of high-altitude auroral rays by Vallance Jones and Hunten [1960] with a 4-Å spectral resolution found the vibrational and rotational temperatures to be in equilibrium with atmosphere at 2200K. Subsequent measurements in the mid-latitude twilight of the N_2^+ first negative 0-0 band at 3914 Å, by Broadfoot and Hunten [1966], indicate a low rotational temperature of 1600K. Newton et al. [1974] also concluded that for SAR arc intensities of 0.554kR, a vibrational temperature of 1320K would result, while a 5.5kR arc would produce a vibrational temperature of 2480K. Vlaskov and Henriksen [1985] and Pavlov [1994c] calculated the effective vibrational temperature of N_2 by using the data of N_2^+ 1st negative band emission intensity and data on Franck - Condon factors and Einstein coefficients for the vibrational electron transition. Vlaskov and Henriksen [1985] determined Tv=1100～2560K on the base of the intensity ratio of the different vibrational- rotational bands.

Vibrational and Rotational Temperature Measurement on the Aircraft

The direct measurement of rotational temperature of molecular nitrogen in the lower thermosphere was done by Deleeuw and Davies [1972] for the first time by means of electron beam and two channel photomultipliers on a sounding rocket. The results shows good agreement with neutral temperature of US Standard atmosphere model above 110km. The direct measurement of vibrational temperature of N_2 was done for the first time by O'neil [1974] by using the rocket -borne system utilized electron beam induced luminescence of N_2^+ 1st negative band in the aurora. An upper limit for the N_2 vibrational temperature was given in the altitude range 80 - 175km, such as 1500K at 175km, 1200K at 155km, 1000K at 135km and 800K for altitudes less than 115km. In 90's ,the spectral images of N_2^+ 1st negative band system in dayglow were made with Imaging Spectroscopic Observatory flown on the shuttle[Torr et al. 1992, Torr et al. 1993]. It was found that rotational temperature of ～3000K was needed to explain the data while apparent vibrational temperature was ～6000K to 8000K at the altitude of ～250km [Torr et al. 1992]. Conventional thermospheric theory is not able to account for these high vibrational temperature. Dothe [1996] analyzed three prominent infrared radiators, CO, CO_2 and NO^+ from the database of infrared spectrometer flown on the space shuttle (CIRRIS 1A)in the altitude range of 120 -200km, and determined the rotational temperature respectively as shown in Figure 1-4. Barth and Eparvier [1993] determined rotational temperature of NO at the altitude range 110 -140km by using the NO gamma band spectra in the ultraviolet dayglow obtained by the rocket experiment at Poker Flat, Alaska. The results agreed with the kinetic temperature of MSIS86 model (Figure 1-5). Rotational temperature for CO agreed with translational temperature from the MSIS model and therefore characterized as LTE. The emission from CO_2 (NO^+) had a lower (higher) rotational temperature than the MSIS translational temperature over a altitude range.

Kawashima et al. [1997] improved the same system as O'neil [1974]'s by using the grating spectrometer with the linear image sensor and obtained the spectral image of N_2^+ 1st negative band system at the altitude range of 100 - 150km and determined the upper limit for N_2 vibrational temperature and derived N_2 rotational temperature profile simultaneously in altitude. Our detail work will be described in the present report.

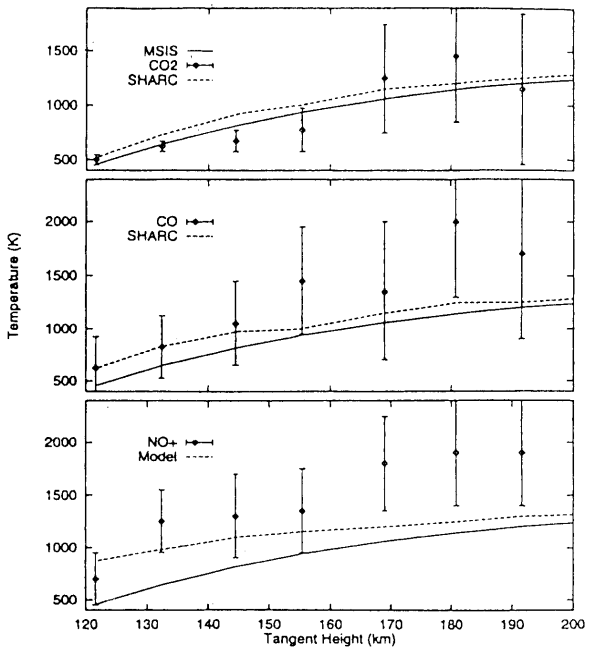

Fig. 1-4: Rotational temperature of the infrared emission derived from the spectrometer (CIRRIS 1A) flown on the shuttle (diamonds) and from the rotational LTE model (dashed line); the solid line is the local temperature from MSIS model (Dothe, 1996).

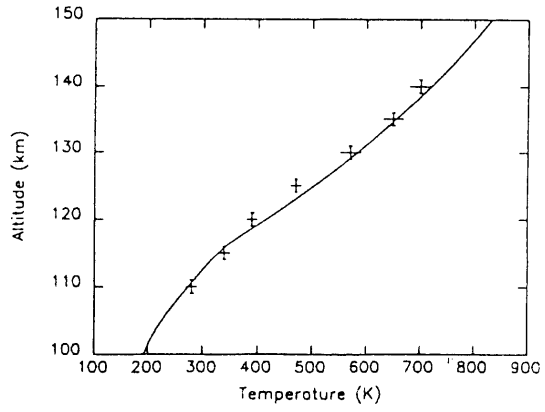

Fig. 1-5: Rotational temperature determined from NO γ (1, 1) band in the ultraviolet dayglow obtained from the rocket experiments (Barth, 1993).

II TECHNIQUE OF THE MEASUREMENT

II-1 BASIC THEORY OF MEASUREMENT

Figure 2-1 shows potential energy curves for the bound states of N_2^+ and N_2. The left panel of Figure 2-1 shows the singlet state of N_2 and the right panel of Figure 2-1 shows triplet state of N_2. A molecule has many electron energy states such as X, A, B,... having potential energies of several eV. The corresponding band specrta involved with electron energy states transition are observed in the ultra-violet and visible regions. The nuclei of a molecule are usually vibrating around the equilibrium distance defined as the minimum potential energy. The vibrational molecular energies are roughly smaller than electronic energies by a factor of $(m/M)^{1/2}$, where m and M are mass of the electron and the nucleus, respectively. The ratio m/M being in the range of 10^{-4}, the vibrational molecular energies are of the order of a few 0.1eV. The vibrational energy levels are usually identified by the vibrational quantum number of v. Each vibrational energy level is further divided into many rotational energy levels, roughly smaller than electronic energies by a factor of m/M. Thus the rotational energy order is 0.001eV. For the electronic ground state of N_2 ($X\,^1\Sigma_g^+$), the first excited vibrational energy is 0.29eV and rotational energy is 0.000496eV, corresponding to temperature of 3390K and 5.8K respectively. Transitions between rotational levels, belonging to the same electronic level, are observed in the infrared region. Transitions between vibrational levels, belonging to the same electronic and vibrational level, are observed in the far infrared region and the microwave regions. But in the case of homonuclear infrared inactive molecules such as N_2, only the vibrational-rotational transitions involved with electron states transition are observed, but vibrational-rotational transitions or rotational transitions by themselves are not. Figure 2-2 shows vibrational - rotational spectrum of N_2^+ and N_2 involved with electron state transition. Therefore in order to measure the vibrational - rotational distribution in the ground state of N_2, we should at first excite or ionize the molecules to upper electron sate by the electron beam or the laser, then observe the vibrational - rotational band in the radiation involved with electronic states de-excitation transition. Finally we can infer the initial vibrational - rotational distribution in the original electronic state from the vibrational - rotational bands by assuming Franck - Condon theorem and optical selection rule in the excitation

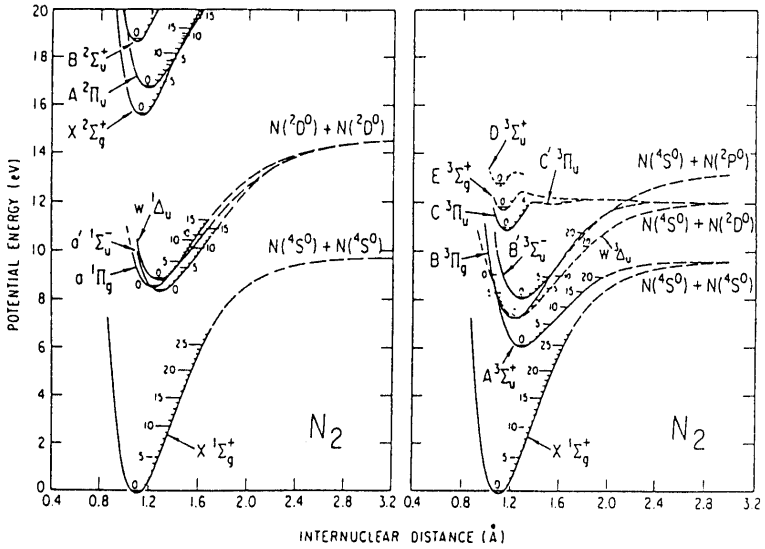

Fig. 2-1: Potential energy curves for the bound states of N_2^+ and N_2.

process. This method originally developed by Muntz[1962] and applied to the nitrogen gas flow allows us to measure indirectly the vibrational and rotational static temperatures of the neutral N_2 in the flow. He showed that the method of analysis of the so-obtained spectrum based on assuming that the optical selection rules also apply to the excitation produced by the beam electrons, gives reasonable results for the rotational temperature. Hunter [1968] also applied this method not only to the rotational temperature measurement but also to the vibrational temperature measurement. He determined vibrational temperature of the ground state with the uncertainty of as large as 20 percent. Then we describe the precise process of the measurement technique as follows.

The excitation and emission path for the first negative system is illustrated by energy-level diagram in Figure 2-3 and Figure 2-4 for vibrational transition and rotational transition respectively. Atmospheric molecular nitrogen is usually in the ground state. If it is assumed that vibrational and rotational energy levels in the ground electric state of $X^1\Sigma_g^+$ are in the local thermal equilibrium (LTE), the vibrational and rotational population distributions are given by a Maxwell - Boltzmann distribution at vibrational temperature (T_v) and rotational temperature (T_r) respectively. The population of the individual vibrational-rotational level identified by given vibrational quantum number (v_1") and rotational quantum number (J_1") is

$$N_{v_1"} = \frac{N_0}{Q_{v_1"}} \exp\left(-\frac{hc\,G_{v_1"}}{k\,T_v}\right) \quad \left[G_{v_1"} = \omega_e(v_1"+\frac{1}{2})\right]$$

$$N_{v_1",J_1"} = \frac{N_{v_1"}}{Q_{J_1"}}(2J_1"+1)\exp\left(-\frac{hc\,F_{J_1"}}{k\,T_r}\right) \quad \left[F_{J_1"} = BJ_1"(J_1"+1)\right] \qquad (2\text{-}1)$$

Here h is plank constant, c is light velocity, k is Boltzmann's constant and Q is normalization factor. Molecular constants ω_e = 2358.57 cm^{-1} and B=1.99824 cm^{-1} are given by Herzberg [1979].
Next , the simultaneous ionization and excitation process from $N_2X^1\Sigma_g^+$ to $N_2^+B^2\Sigma_u^+$ by electron impact is discussed. As there is little interaction between the electronic and nuclear motions in a molecule , the nulei and the electrons move almost independently. As the heavy nuclear periods of vibration or rotation is much longer than that of the electron, the heavy nuclei do not change their positions or momenta during the electron impact ionization process if the interaction time between the high energy incident electron and the molecular nitrogen is short enough. Therefore the molecule in the ground state may be excited *straight up* to the upper state. This is known as the Franck -

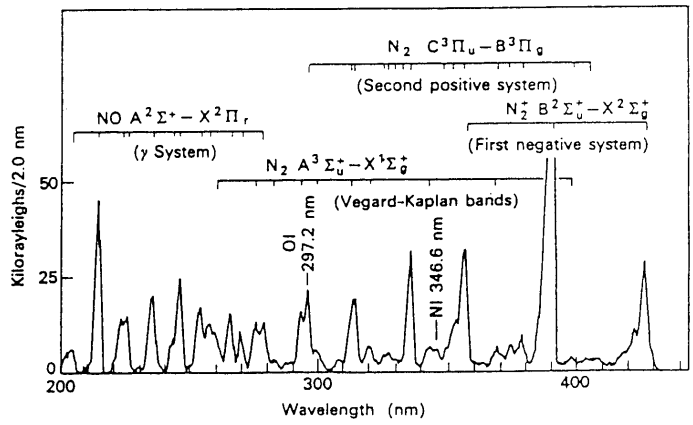

Fig. 2-2: Electrical - vibrational - rotational spectrum of N_1^+ and N_2 in airglow.

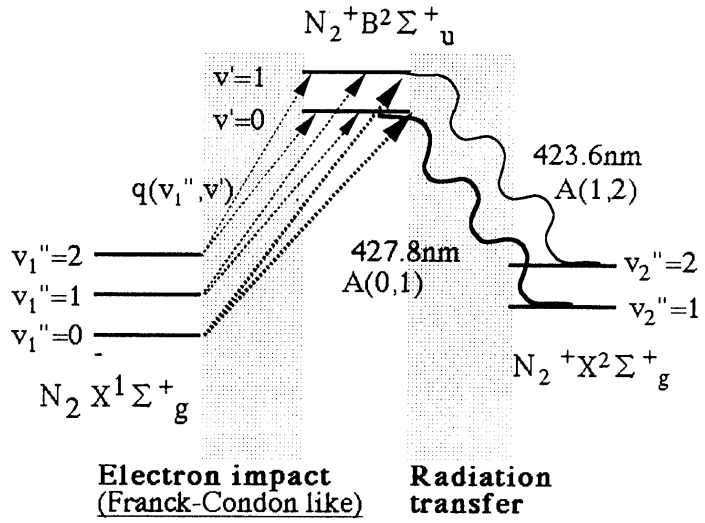

Fig. 2-3: Diagram of excitation and emission path for vibrational energy-levels.

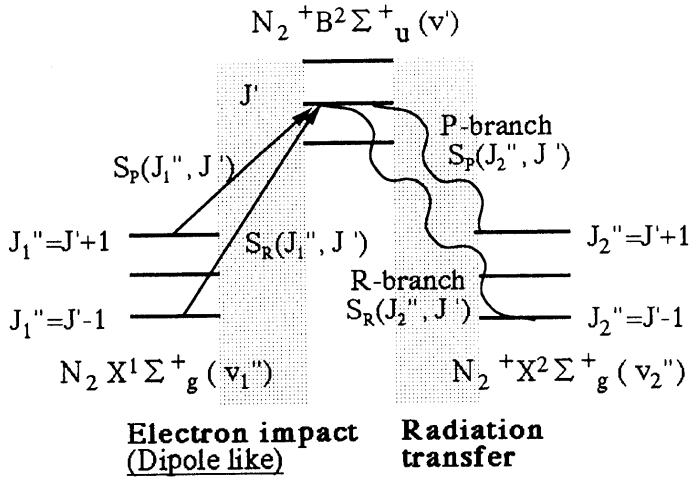

Fig. 2-4: Diagram of excitation and emission path for rotational energy-levels.

Condon principle. The transition probability between lower vibrational level (v_2") and upper vibrational level (v') is proportional to the Franck-Condon factor, expressed as the square of the overlap integral of the vibrational wave functions between the upper level and the lower level.

$$q(v_1",v') = \left| \int \Psi_{v_1"} \Psi_{v'} \, dr \right|^2$$

$\Psi_{v1"}$ and $\Psi_{v'}$ is the vibrational wave function of the $N_2X^1\Sigma_g^+$ state and $N_2^+B^2\Sigma_u^+$ state respectively. Franck - Condon factors for $N_2X^1\Sigma_g^+ \rightarrow N_2^+B^2\Sigma_u^+$ transition have been determined both theoretically and experimentally by many researchers [Bates,1949; Nicholls,1962; Gilmore,Laher and Espy,1992]. As for the rotational transition, dipole like transition is assumed in the excitation process. Thus transition probability is proportional to Honl London factor [Herzberg 1950],

$$S_R(J_1",J') = \frac{J_1"+1}{2J_1"+1} = \frac{J'}{2J'-1} \text{ (R-branch)} \qquad S_P(J_1",J') = \frac{J_1"}{2J_1"+1} = \frac{J'+1}{2J'+3} \text{ (P-branch)}$$

The population of the rotational level of upper electronic state identified by J' is gathered only from the rotational level of lower electronic state identified by J_1" which satisfies the electric dipole selection rule $J_1"=J' \pm 1$.

Then the production rate of the $N_2^+B^2\Sigma_u^+$ (v= v', J= J') is given,

$$N_{v',J'} = N_i \, R \sum_{v_1"} \frac{N_{v_1",J'+1} \, S_P(J_1",J') + N_{v_1",J'-1} \, S_R(J_1",J')}{\theta} q(v_1", v')$$

$$\theta = \sum_{J_1'} [N_{v_1",J'+1} \, S_P(J_1",J') + N_{v_1",J'-1} \, S_R(J_1",J')] \qquad (2\text{-}2)$$

where θ is normalization factor, $N_i[cm^{-3}s^{-1}]$ is the total ion production rate per second and R is ionization excitation branching ratio for $N_2^+B^2\Sigma_u^+$ state. R is estimated to be 0.09 ± 0.02 using the coincidence ionization experiment [Goembel and Doering, 1994]. N_i is expressed as

$$N_i[cm^{-3}s^{-1}] = N_0 \, \sigma_i n_e v_e$$

Where N_0 is the number density of N_2, σ_i is the total ionization cross section of N_2, n_e is number density of electron in the electron beam, v_e is velocity of electron in the beam. The electron beam current is expressed as $i = Sen_ev_e$, thus

$$N_i = \frac{N_0 \sigma_i \, i}{Se} \qquad (2\text{-}3)$$

Where S is the cross sectional area of the electron beam. Next, we discuss the radiation process of $N_2^+B^2\Sigma_u^+ \rightarrow N_2^+X^2\Sigma_g^+$ transition. As the lifetime of $N_2^+ B^2\Sigma_u^+$ state was determined to be 60ns by Dufayard [1974], the $N_2^+B^2\Sigma_u^+$ dose not undergo any collisions during its lifetime under the gas environment corresponding altitude above 100km where the mean collision time is larger than 1ms. That means no vibrational - rotational redistribution by collision occurs at $N_2^+B^2\Sigma_u^+$ state. Multiplied Equation (2-2) by Einstein coefficients and Honl-London factors above mentioned, the volume emission rate of a particular rotational line ($N^{v',J'}_{v_2",J_2"}$) is derived as

$$N^{v',J'}_{v_2",J_2"} = N_{v',J'} \frac{A(v',v_2")S(J',J_2")}{\sum_{v_2"} \sum_{J_2"} A(v',v_2")S(J',J_2")} \qquad (2\text{-}4)$$

The transition probability is determined by both experimentally and theoretically [Shemansky,1971; Gilmore, Laher and Espy, 1992].

Substituting (2-1), (2-2), (2-3) into (2-4), the volume emission rate of a particular rotational line is obtained.

$$N^{v',J'}_{v_2",J_2"} = R \times (\text{ion production rate}) \times (\text{vibrational structure}) \times (\text{rotational structure})$$

$$\text{ion production rate} : N_i = \frac{N_0 \sigma_i \, i}{Se}$$

$$\text{vibrational structure} : \frac{1}{Q_{v_1"}} \frac{A(v', v_2")}{\sum_{v_2"} A(v', v_2")} \sum_{v_1"} \left[q(v', v_1") \exp\left(-\frac{hc\, G_{v_1"}}{k\, T_v}\right) \right] \tag{2-5}$$

$$\text{rotational structure} : \frac{1}{Q_{J_1"}} \left\{ J' \exp\left(-\frac{hc\, F_{J'-1}}{k\, T_r}\right) + (J'+1) \exp\left(-\frac{hc\, F_{J'+1}}{k\, T_r}\right) \right\} S(J', J_2")$$

The ratio of the volume emission rate of vibrational structure of 1NG(v'=0,v_2"=1) band to 1NG(v'=1, v_2"=2) band is given

$$\frac{N^{v'=0}_{v_2"=1}}{N^{v'=1}_{v_2"=2}} = \frac{\dfrac{A(0,1)}{\sum_{v_2"} A(0, v_2")} \sum_{v_1"} \left[q(0, v_1") \exp\left(-\dfrac{hc\, G_{v_1"}}{k\, T_v}\right) \right]}{\dfrac{A(1,2)}{\sum_{v_2"} A(1, v_2")} \sum_{v_1"} \left[q(1, v_1") \exp\left(-\dfrac{hc\, G_{v_1"}}{k\, T_v}\right) \right]} \tag{2-6}$$

The ratio (2-6) is calculated for various Franck - Condon factor and Einstein coefficient as shown in Figure 2-5. The accuracy of the Franck - Condon factor is usually taken to be between 10 and 20 percent [Hunter 1968]. As the first vibrational level of molecular nitrogen has an excitation energy of 3390K (which is called *characteristic temperature for vibration*) , the population of vibrationally excited molecules are very small below 800K This is reflected in Figure 2-5 as a fact that the ratio 1NG(0,1)/1NG(1,2) is almost invariant for low vibrational temperatures. But *characteristic*

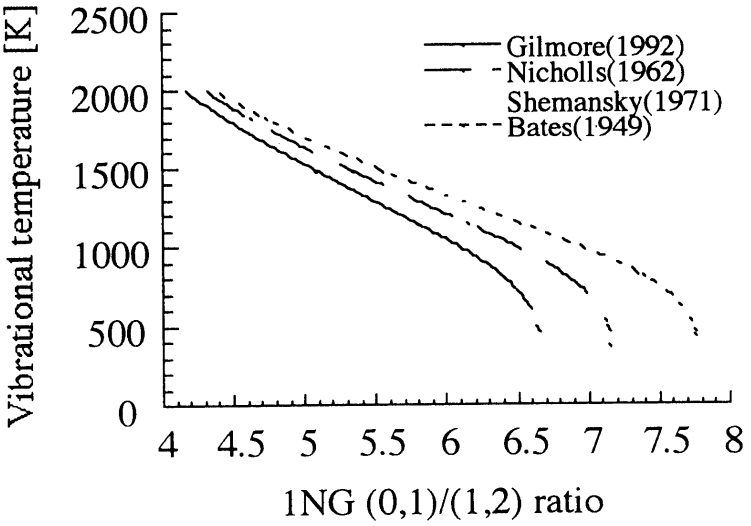

Fig. 2-5: Vibrational temperature as a function of intensity ratio of 1NG(0,1)/1NG(1,2) for various Franck-Condon factors by past researcheras. The Gilmore [1992]'s factors are adopted in the present paper.

temperature for rotation is 5.5K, thus the relative intensities of rotational structure at the same vibrational level shown as a 'rotational structure' in Equation (2-5) dramatically varies even for the order of the room temperature. By measuring relative intensities in the rotational fine structure of the vibrational bands and relative intensities of the vibrational bands themselves, the model mentioned above predicts detailed information about the population distribution in the rotational and vibrational quantum levels of the ambient neutral nitrogen in the electronic ground state. Therefore we can determine vibrational temperaure and rotational temperature from the luminesence induced by the electron beam impact on neutral N_2 gas.

II-2 SYNTHETIC SPECTRUM

This section is devoted to the spectrum analysis technique which enable to determine the vibrational temperature and rotational temperature from the rotationally unresolved spectrum.

When vibrational temperature and rotational temperature are determined from Equation (2-5), several problems arise as follows.

(a) To derive rotational temperature from the relative intensities of independent rotational lines as the way described in Muntz [1962], the wavelength resolution need more than 0.01nm. This specification is almost impossible to the compact grating type spectrometer born on a sounding rocket.

(b) Under the condition of high rotational temperature (>500K), the envelope of the R-branch of 1NG (0,1) band overlaps 1NG(1,2) band. This leads to the incorrect vibrational temperature simply determined by 1NG (0,1) / 1NG (1,2) ratio shown in Figure 2-5 as the way described in Hunter[1968].

(c) The N_2 second positive (2PG) system is also investigated umder the same condition as for the N_2^+ first negative system. The overlap of 2PG (1,5) band [426.8nm] on the R-branch of 1NG (0,1) band deforms the spectral shape of the 1NG (0,1) band.

To resolve the above problems, we calculate the line intensities from Equation (2-5) and convolute them with a instrument slit function of the spectrometer to obtain the synthetic spectrum. The line intensities of 1NG (0,1) band and 1NG (1,2) band calculated from Equation (2-5) are plotted in Figure 2-6. Franck - Condon factor of $N_2X^1\Sigma_g^+ \rightarrow N_2^+B^2\Sigma_u^+$ transition and Einstein coefficients of $N_2^+B^2\Sigma_u^+ \rightarrow N_2^+X^2\Sigma_g^+$ transition by Gilmore et al. [1992] are utilized and the wavelengths of rotational lines are given by Dick (1978). Both vibrational temperature and rotational temperature are assumed to be 300K An example of the typical instrument function of the Spectrometer , Jovin HR-320 with a full width at half maximum (FWHM) of 1nm is also plotted in Figure 2-6 for comparison. Then the synthetic spectrum is produced by convoluting the line intensities with the instrument function. Figure 2-7 shows the synthetic spectra for various values of FWHM. The R-branch of 1NG (0,1) band disappears in the spectrum for 1.2nm. Figure 2-8 shows spectra for various vibrational temperatures, and Figure 2-9 for various rotational temperatures. As mentioned above, the intensity ratio 1NG(0,1) / 1NG(1,2) is almost invariant below 800K because of small population at the vibrationally excited level of ground $N_2X^1\Sigma_g^+$ state. This means the method utilized in the present paper doesn't have much resolution for Tv below 800K. Spectral profile varies remarkably for Tr in the range of 300K $\sim$ 800K because the characteristic temperature for rotation is 5.5K, much lower than that of vibration. It is clearly seen in Figure 2-9 that the envelope of R-branch of 1NG(0,1) band extends to the shorter wavelength region and overlaps 1NG(1,2) band above 500K as a result of the large population of high rotational levels of ground $N_2X^1\Sigma_g^+$ state. The spectral variation for Tr is the most prominent at the wavelength region of R-branch of 1NG(0,1) band (425nm-427nm), because the wavelength intervals between rotational lines of R-branch are broader than those of P-branch. Figure 2-9 shows if a FWHM of the instrumental function is smaller than an overall R-branch wavelength

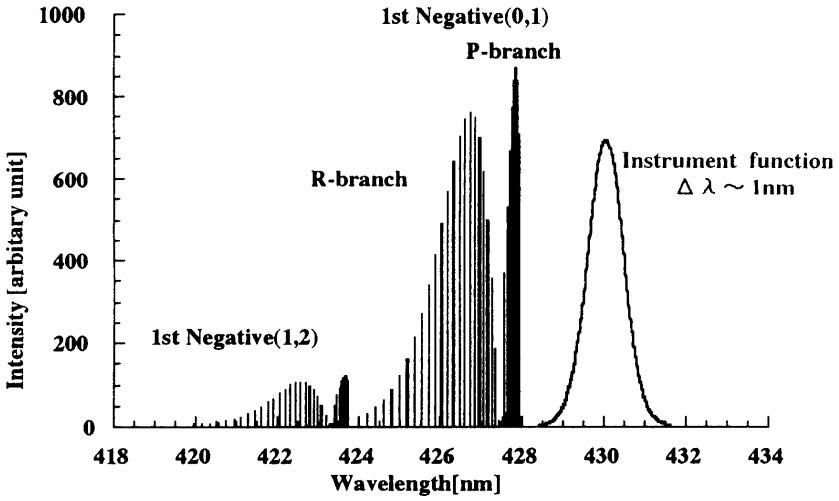

Fig. 2-6: Line intensities of vibrational - rotational bands of 1NG(0,1) and 1NG(1,2) Tv=300K and Tr=300K are assumed. The typical instrumental function in the present paper with a FWHM of 1nm is also plotted for comparison.

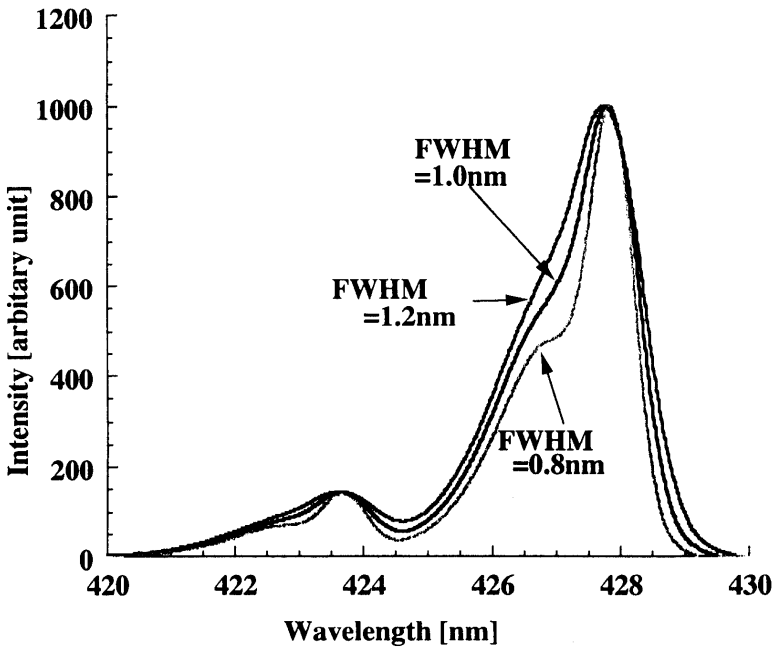

Fig. 2-7: Synthetic spectra for various half widths of the instrument function. Tr=300K and Tv=300K are assumed.

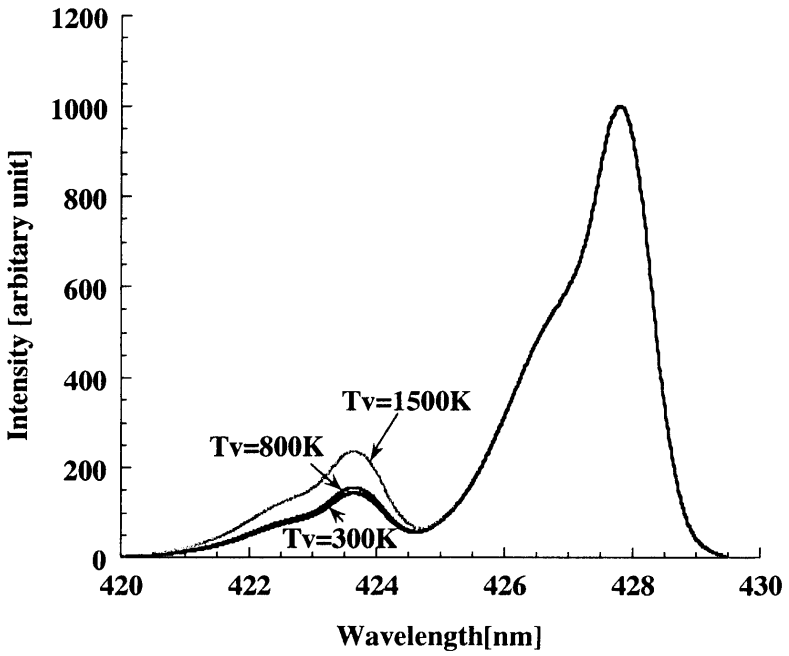

Fig. 2-8: Synthetic spectra for various vibrational temperatures. The spectra are normalized by the intensity of the 1NG(0,1) band for convenience. FWHM of 1nm and Tr=300K is assumed.

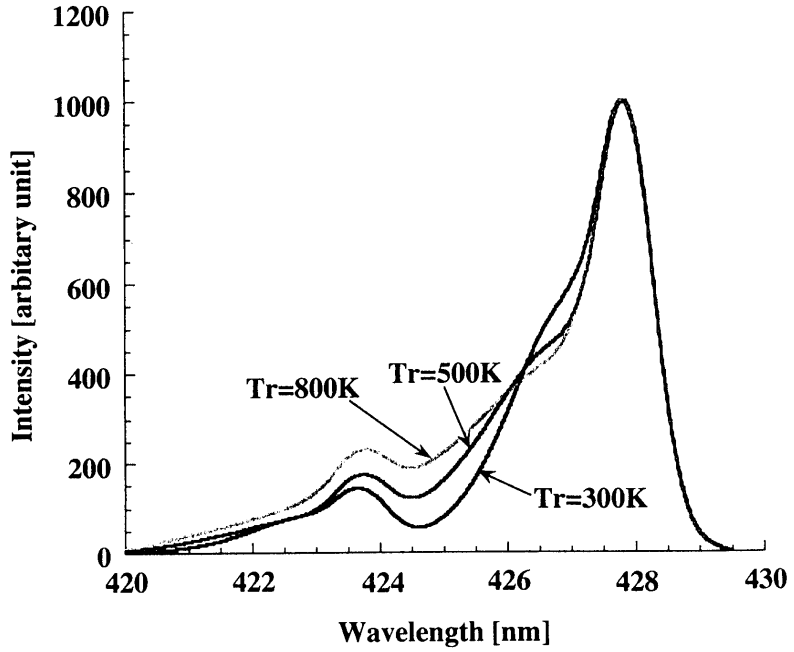

Fig. 2-9: Synthetic spectra for various rotational temperatures. The spectra are normalized by the intensity of the 1NG(0,1) band for convenience. FWHM of 1nm and Tv=300K are assumed.

scale size (1.5nm), the spectrum profile reflects relative rotational intensities sufficiently to enable us to determine Tr. This method can be useful in the whole target altitude region (100 - 160km) of the rocket experiment where the kinetic temperature is expected to be in the range of 200K - 800K.

As shown above , the spectral variations for three variables, the FWHM of instrument function, vibrational temperature and rotational temperature are independent each other. Conversely optimum values of three variables can be determined independently from the spectrum. The mathematics to simultaneously determine a FWHM of instrumental function and rotational temperature from rotationally unresolved spectrum is described by Phillips [1975]. In the present thesis , we obtained optimum values by simply minimizing the fitting error for various three parameters. Fitting error is defined as the ratio of the integral difference squared between the synthetic spectral profile and the experimental spectral profile to the integral area enclosed with the data spectral profile as follows.

$$\text{Fitting error} \equiv \frac{\sqrt{\sum_i \left(f(\lambda_i) - y(\lambda_i)\right)^2}}{\sum_i y(\lambda_i)}$$

$f(\lambda_i)$: Synthetic spectrum (2-7)

$y(\lambda_i)$: Observation spectrum

The optimum Tv and Tr are defined as the values when fitting error is at minimum. This method can be applied to the rotationally unresolved spectra obtained by the spectrometer with a resolution of about 1nm . If fitting error is smaller than 0.1, the synthetic spectrum well explains the observation spectrum. Generally fitting error includes two errors, one is due to experimental noise and the other is due to the lack of the synthetic spectrum itself to explain the complete process of the measurement. The reason why FWHM of the instrumental function is taken as a fitting parameter in addition to Tv and Tr is that determining the instrumental function is very difficult because its FWHM is usually dependent not only on the wavelength resolution of the spectromenter but also on the scale size of the emission target in the field of view of the spectrometer. It is *theoretically* true that Tr and FWHM of the instrumental function ($\Delta\lambda$) can be determined independently and uniquely but it should be discussed more carefully in applying this method to the analysis of the real spectrum. The independence and uniqueness of the optimum Tr and $\Delta\lambda$ will be discussed in Chapter Ⅳ-2.

Ⅲ EXAMINATION OF THE VALIDITY OF THE MEASUREMENT TECHNIQUE

The purpose of this section is to examine the validity of the basic measurement technique of Tv and Tr based upon a simple Franck - Condon model and a dipole like transition involving simultaneous ionization and excitation of the neutral molecule. We examined the basic measurement theory for various projectile electron energies.

Tv and Tr Measurement in the Laboratory

It is known that the vibrational energy distribution of excited electronic states can certainly be well described by the Franck - Condon principle if the projectile particle velocity is greater than 2×10^7 cm/sec (corresponding kinetic energy is 100eV) in the case of the electron beam impact excitation [Doering et al. (1994)] and 10^8 cm/sec in the case of the ion beam impact excitation [Moore and Doering, 1969]. In such cases, if the process involves excitation of a molecule which is initially in the

ground electronic and vibrational states of $X^1\Sigma_g^+$ (v_1"=0) to some excited electronic and vibrational state of $B^2\Sigma_u^+$ (v' =*n*), the ratio of the population of $B^2\Sigma_u^+$ (v' =*n*) to the population of $B^2\Sigma_u^+$ (v'=0) state is given by the ratio of Franck-Condon factors for the two transitions $X^1\Sigma_g^+$ (v_2"=0) $\rightarrow B^2\Sigma_u^+$ (v'=n) and $X^1\Sigma_g^+$ (v_2"=0)$\rightarrow B^2\Sigma_u^+$ (v'=0) as described in Chapter Ⅱ-1. But the ratio of the population of $B^2\Sigma_u^+$ (v' =*n*) to $B^2\Sigma_u^+$ (v' =0) excited by low-energy electrons depart notably from the prediction of the Franck - Condon principle. It is the same with Tr measurement. In order to infer the initial neutral N_2 rotational temperature from the observed N_2^+ rotational energy distribution, it is obviously necessary to understand the excitation process and to know whether the $N_2^+B^2\Sigma_u^+$ excited state distribution accurately reflects the initial neutral N_2 rotational temperature. The Muntz model described in the previous section assumes that when moderately-high-energy electrons (50 - 100keV) pass through a low-density nitrogen gas, having an assumed Boltzmann rotational distribution, the rotational excitation obeys the optical dipole selection rules for the transition involved. Within this framework one can then measure the rotational distribution of excited $N_2^+B^2\Sigma_u^+$ and infer the nascent rotational distribution in the neutral $N_2X^1\Sigma_g^+$. O'Neil and Davidson [1969] did rotational temperature measurement by excitation of the 1NG(0,0) [391.4nm] band for electron energies of 10 keV, 17.5 keV and 60keV, respectively. They report good agreement of observed N_2 rotational temperature with gas temperature. Culp [1967] also shows reasonable agreement between observed rotational temperature and the gas temperature by using the same method and the same band as O'Neil and Davidson [1969] from 100eV to 300eV. But he showed Tr was observed to depend upon electronic energy for energies below 100eV; Tr reaches a maximum of about 350K at 19eV for a gas temperature of 296K. Hernandez [1982] also showed the rotational state distribution of ground-state $N_2X^1\Sigma_g^+$ in supersonic expansions is found to be constant with electron energy >800eV. But breakdown of the $|\Delta J|=1$ optical selection rule occurs with $|\Delta J|=3$ transition observed first below 800eV, followed by much larger ΔJ transition at low energies <100eV.

Experimental Configuration

A brief description of the apparatus is given and illustrated schematically in Figure 3-1. It is composed of an electron gun and a spectrograph monochrometer. The electron gun was set up in the vacuum chamber made of PYREX glass. The optical transmittance of PYREX glass is constant at 92% for wavelengths longer than 360nm. The monochrometer was Jovin Yvon HR-320. The specification is as follows. The type of grating is holographic, the reciprocal linear dispersion is 2.5nm/mm, number of grooves is 1200 mm^{-1} and blaze wavelength is 130nm - 800nm. The instrumental function was determined from the line spectrum of mercury lump at 404.66nm. A full width at half maximum (FWHM) of the instrumental function was 0.82nm.

Figure 3-2 shows the detail configuration of the electron gun. The electron gun is composed of two electrode. Cathode is the 25mm diameter disk made of nickel covered with BaO, to which potential of -100V～-2kV was applied. Anode is made of stainless mesh and on the ground potential. Thermal electrons are emitted from the disk cathode heated by the coil heater and accelerated toward anode. Finally they form the electron beam after passing through the mesh anode. The electron beam current in the range of 1- 10mA is monitored by the collector. We applied a potential of 40V to the collector in order to prevent secondary electrons from being emitted out of the collector surface.

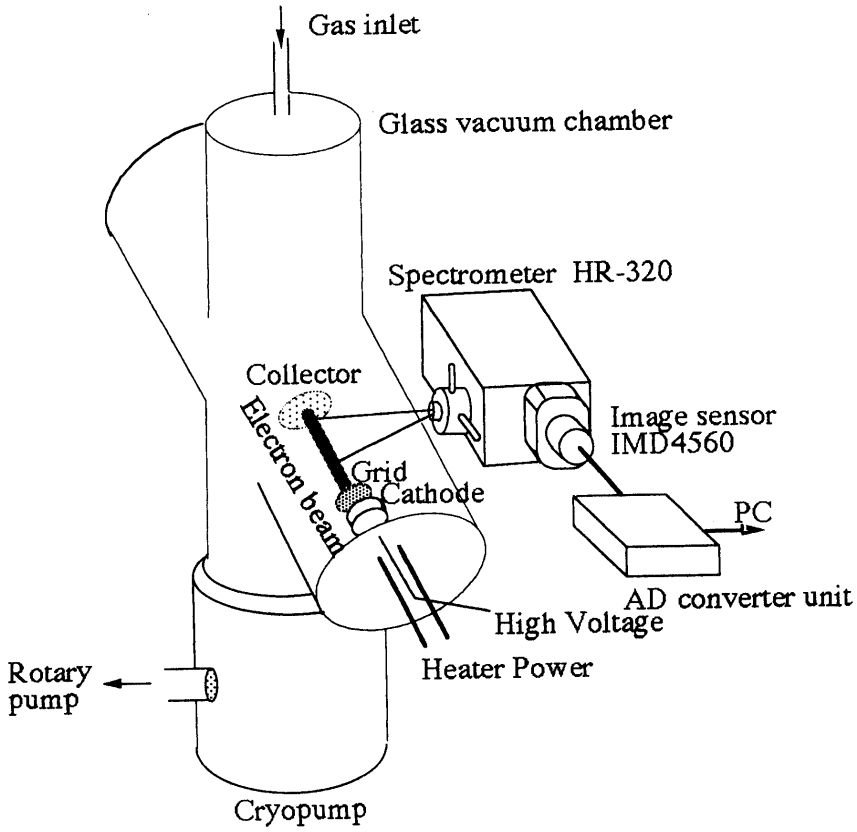

Fig. 3-1: Experimental setup.

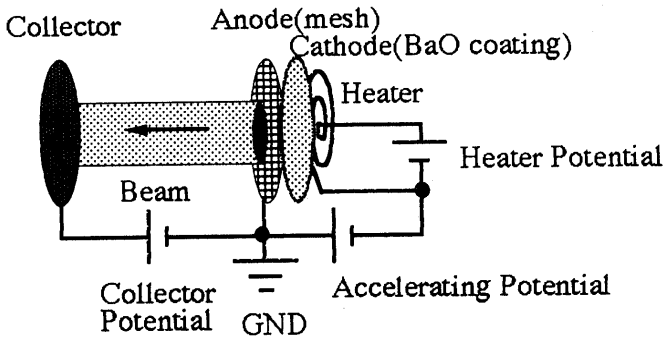

Fig. 3-2: Schematic configuration of the electron gun.

Results

We obtained the spectra of 1st negative (0,1) band [band origin at 427.5nm], (1,2) band [423.4nm] and (2,3) [419.7nm] in the wavelength region of 410 - 430nm for various accelerating potentials. Figure 3-3 shows the spectra for the projectile energies of (a)15eV, (b)70eV and (c)2keV respectively together with the synthetic spectra. The synthetic spectra were all the same, which were obtained by being fitted to the spectrum in panel (b). The optimum value of Tr was determined to be 350K. The large discrepancy between observed spectra and synthetic spectra was shown at R-branch region (425nm - 427nm) of 1NG(0,1) band in panel (a) and (c). This discrepancy is attributed to the overlapping spectrum of N_2 second positive band (1,5) [426.8nm]. Another notable point in panel (a) and (c) was anomalously larger intensity of 1NG(2,3) band than Franck - Condon expectation.

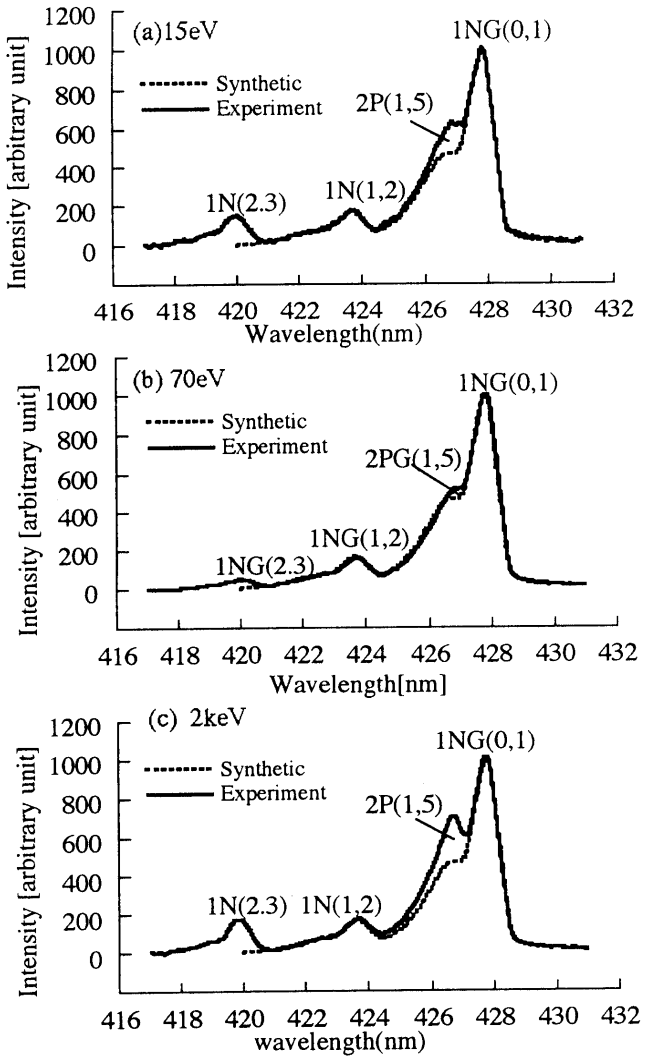

Fig. 3-3: Projectile energy dependence of $\Delta v=-1$ sequence of N_2^+ first Negative System. (a)15eV, (b)70eV, (c)2keV respectively. Dash line shows Experiment spectrum. Solid line shows Synthetic spectrum. The spectra are normalized to equal heights of the (0,1) band.

Figure 3-4 shows the plot of the experimentally determined intensity ratio 1NG(0,1) / 1NG(1,2) versus projectile electron energies. Figure 3-4 shows that the intensity ratio increased with increasing energy. But the ratio gradually decreased again with energy for high energy region of ~ 1keV. We introduced a function to interpret this tendency of 1NG(0,1) / 1NG(1,2) versus projectile electron energies and fitted to the observation data.

$$\frac{1NG(0,1)}{1NG(1,2)} = (6.03 \pm 0.061) \times \{1 - \exp(-\frac{V_{acc}}{9.92})\} - 1.89 \times 10^{-4} V_{acc} \qquad (R=0.662)$$

Where V_{acc} is accelerating potential in volts. The first term of the right member describes that the intensity ratio become asymptotic to ~6. According to the synthetic spectrum based on Franck - Condon factor calculated by Gilmore [1992] and convoluted with the instrumental function , the intensity ratio equals to 5.81 for 350K. This led the fact that Franck - Condon principle was valid above 100eV. This result was consistent with Doering et al. [1994]. While below 100eV the intensity ratio was smaller than 5.81, especially the value was even around 5 at tens eV. This value corresponds to high vibrational temperature of 1500K. Therefore Franck - Condon principle was not valid below 100eV. The reason why the ratio decreased again in the high energy region might be due to the coexistence of the low energy electrons such as secondary electrons with high energy primary beam electrons. This effect will be discussed in the subsequent section. Figure 3-5 shows the same plot as Figure 3-4 but for the intensity ratio of 1NG(0,1) / 1NG(2,3). The ratio showed a peak at 100eV, and decreased with increasing energy. This tendency was the same as the case of 1NG(0,1) / 1NG(1,2) but showed serious discrepancy from Franck-Condon theory even at 100eV. The corresponding vibrational temperature was ~3000K. Pendelton and O'Neil [1972] reported the experimental relative photoemission rate of 1NG(0,1) / 1NG(2,3) exceeded the corresponding theoretical values expected from Franck-Condon theory by factors of 5. They explained the discrepancy in terms of occurrence of overlapping spectra which were not accounted for 1NG(2,3) band or the occurrence of a second excitation mechanism. We might attribute the discrepancy to the overlap of the second positive (2,6) band[420nm] of N_2 on the 1NG(2,3) band. Anyway we should not utilize the 1NG(2,3) band to determine Tv for the reason mentioned above.

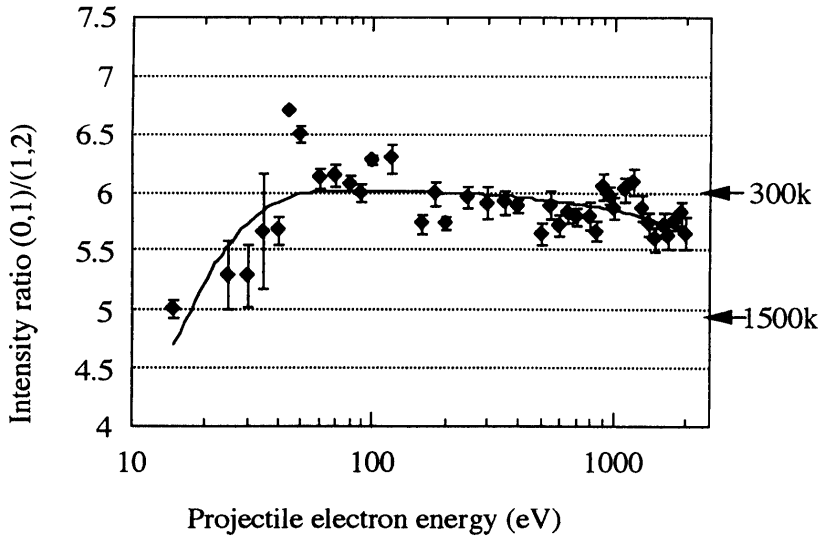

Fig. 3-4: Ratio of intensities of the 1NG (1,2) and (0,1) bands in collisions of 10 - 2ke V electrons with N_2. The arrow indicates the ratio calculated for a simple Franck-Condon mechanism as described equation (2-6) by assuming Tv of 300K and 1500K.

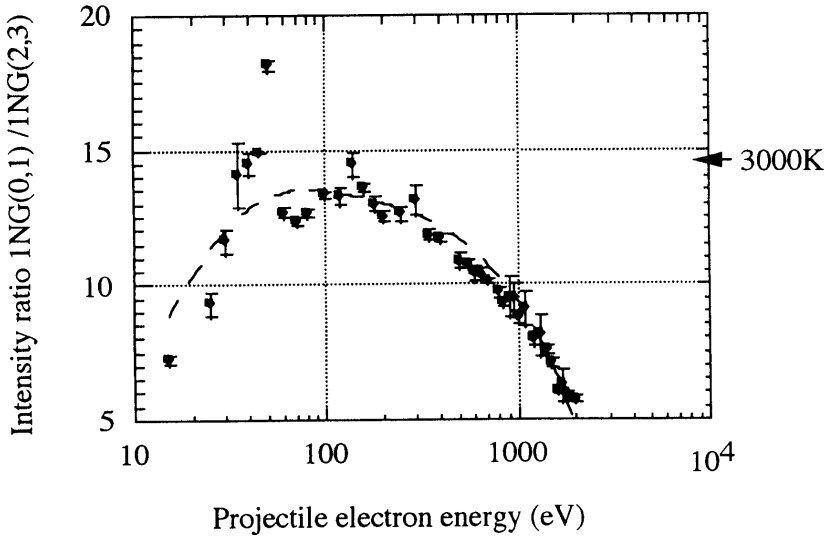

Fig. 3-5: Same as Fig. 3-4 but for ratio of intensities of the 1NG (2,3) and(0,1) bands. The arrow indicates the ratio calculated for a simple Franck-Condon mechanism as described equation (2-6) by assuming Tv of 3000K.

The N_2 second positive band systems (2PG) $N_2C^3\Pi_u \rightarrow N_2B^3\Pi_g$ was also investigated in Figure 3-3 (a) and (c) together with N_2^+ first negative system. The upper panel and middle panel of Figure 3-6 shows the absolute emission cross section versus projectile electron energy (so-called *excitation function*) of 1NG(0,0) [Burns, 1969] and 2PG(0,2) [Borst and Zipf, 1970] respectively. The peak of emission cross section of 2PG(0,2) is at 14eV, much lower than that of 1NG (0,0) at 100eV. Branching ratio 2PG(0,2) / 1NG(0,0) is as large as 1.57 for 20eV but becomes nearly equal to zero above 100eV.The experimental results obtained from the same spectrum as utilized in Figure 3-4 are overplotted together with the past values in each panel. The experimental emission cross section of 2PG(0,2) and 1NG(0,0) are normalized by the maximum value of the absolute emission cross section of Shaw and Compos [1983] and Borst and Zipf [1970] respectively. The tendency of experimentally determined relative emission cross section nearly agrees with previous results as shown in Figure 3-6. But experimentally determined branching ratio 2PG(0,2) / 1NG(0,0) as shown in the lower panel of Figure 3-6 reached a minimum at 100eV and increase with increasing projectile electron energy. This tendency was anti-correlation with the ratio of 1NG(1,2) / 1NG(0,1) as shown in Figure 3-4. Unexpected small value of 1NG(1,2) / 1NG(0,1) and large value of 2PG(0,2) / 1NG(0,0) for high energy suggested a lot of low energy electrons might coexist with primary high electrons. This fact could also agreed with reason why the ratio 1NG(1,2) / 1NG(0,1) decreased again above 100eV in Figure 3-4 and Figure 3-5. Therefore we can take branching ratio of 2PG(0,2) / 1NG(0,0) as a useful indicator to examine the influence of low energy electrons in the observation region.

If there are excitation effect of disturbing the information of initial vibrational- rotational distribution, which are more important at low energies, experiments will have to be done with great care to avoid excitation of the N_2 gas target by low energy electrons, such as secondary electrons from the gas and surfaces in the apparatus. Otherwise anomalously high vibrational temperature may be obtained. Figure 3-7 shows energy distribution of secondary electrons involved with ionization of N_2 for various projectile electron energies. Most of secondary electrons have an energy below 50eV

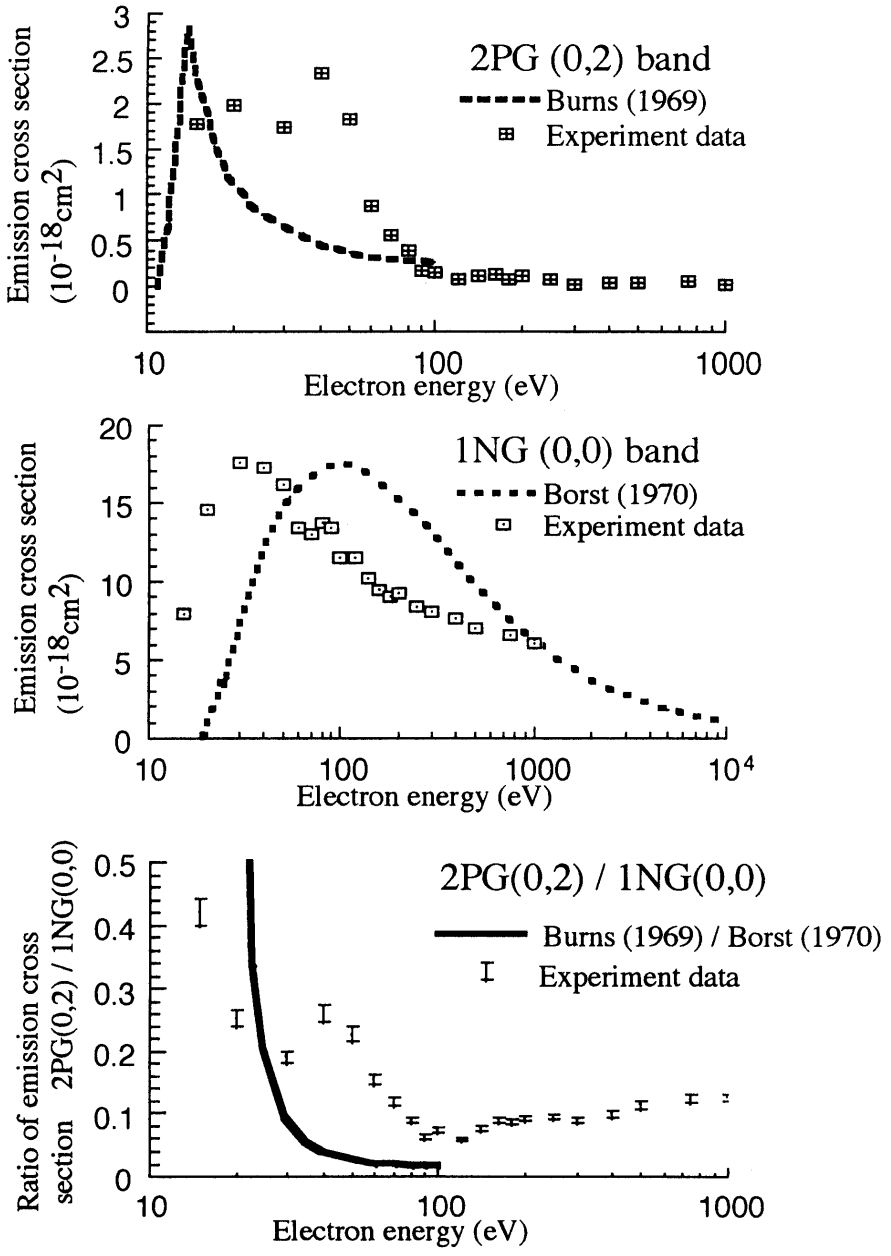

Fig. 3-6: Emission cross section for the electron-impact excitation of the transitions concerned. Upper panel shows emission cross section of 2PG(0,2) band [380.4nm] by Burns [1969]. Middle panel shows emission cross section of 1NG(0,0) band [391.4nm] by Borst and Zipf [1970]. Lower panel shows Ratio of emission cross section of 2PG(0,2)/1NG(0,0). Experimental date are normalized by a peak value of Shaw [1983] for upper panel and peak value of Bost and Zipf [1970] for middle panel respectively.

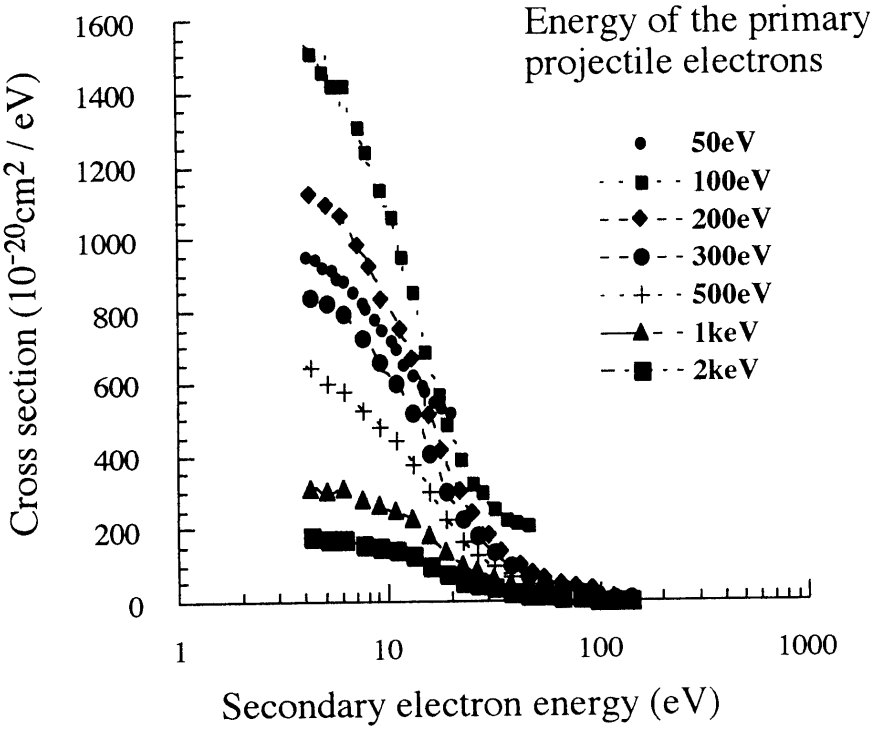

Fig. 3-7: Secondary energy distribution in collisions of 50 - 2keV electrons with N_2 [Opal, Beaty and Peterson, 1972].

but some of them have a energy larger than ionization potential of $N_2^+B^2\Sigma_u^+$, 18eV. Therefore some secondary electrons have an enough potential to produce 1NG band emission.

In addition to secondary electrons from the target gas, secondary electrons from surfaces of the collector is fatal for Tv measurement. Figure 3-8(a) shows a picture of the experiment under the pressure of 2×10^{-4} Torr , the projectile energy is 1keV and applied collector potential is 10V. In Figure 3-8(a), the red-purple luminescence of conical shape region is observed around the blue-purple electron beam trajectory. This red-purple region corresponds to the luminescence produced by secondary electrons. Red color suggested the existence of N_2 first positive bands which have the almost the same excitation function as N_2 second positive bands. We could also investigate the red-purple region adjacent to the collector probably corresponding to luminescence produced by the secondary electrons which are produced by the bombardment of beam electrons on the collector surface. Figure 3-8(b) shows the same picture as Figure 3-8(a) but for applied collector potential of 1kV. The red-purple region were moved toward the collector of high positive potential. On the contrary the blue luminescence was clearly seen in the region adjacent to the anode after the secondary electron robe region was bared.

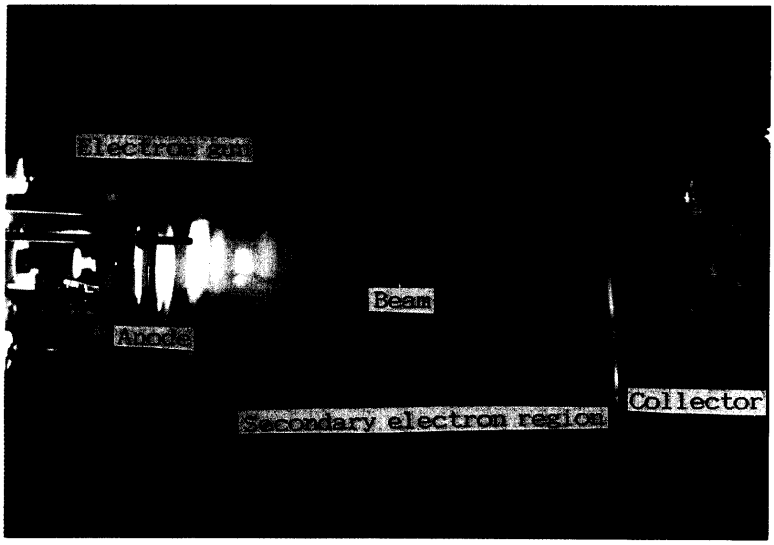

Fig. 3-8(a): The picture of the experiment.
The electron gun was shown on the left. The beam energy is 1keV and the potential applied to the collector is 10V. The vacuum range is 9×10^{-4} Torr. The blue light is the emission from the ionized molecular nitrogen, corresponding to the electron beam trajectory. The blue emission mainly consists of 1st negative band. The red-purple region around electron beam trajectory and adjacent to the collector shows 1st positive band and 2nd positive band corresponding to the existence of secondary electrons.

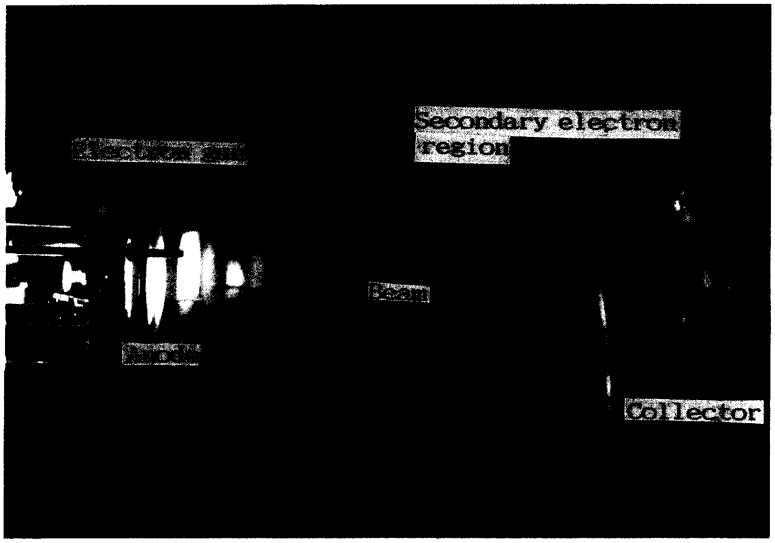

Fig. 3-8(b): The same picture as Fig. 3-8(a) but for the collector potential of 1kV
The red-purple region is drawn closer to the collector. The blue region adjacent to the anode is clearly seen corresponding to pure 1st negative band.

Figure 3-9 shows the spectrum under the condition of Figure 3-8(b). Panel (a) shows spectrum in the region adjacent to the anode , panel (b) shows spectrum in the region adjacent to the collector region. We observe only 1NG(0,0)band in panel (a), but 2PG bands are clearly seen corresponding to the existence of secondary electrons in panel (b). The upper panel of Figure 3-10 shows spectra of 1NG(0,1) and 1NG(1,2) near the anode region and middle panel shows spectra near the collector region together with synthetic spectrum. The fitting is excellent for the upper panel but was not for the middle panel because of the overlapping of 2PG(1,5) spectrum. As mentioned above, the

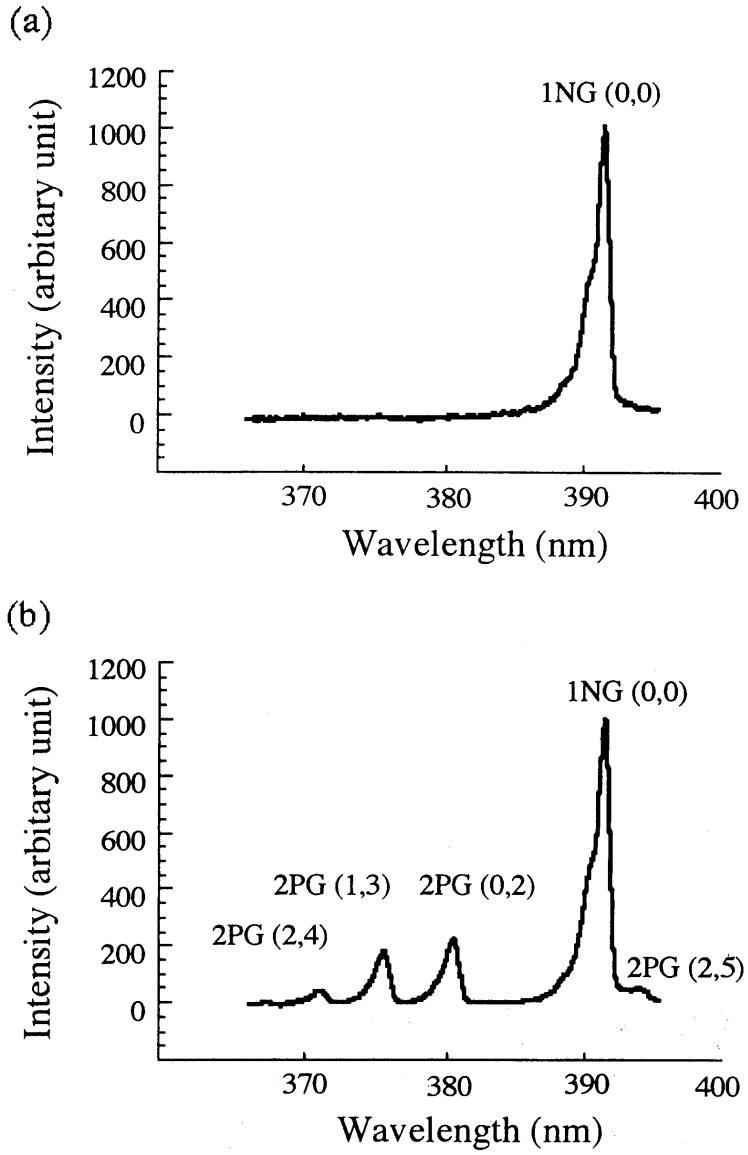

Fig. 3-9: The spectrum of N_2^+ and N_2 in the wavelength region 360nm-400nm under the condition shown in Fig. 3-8(b). Panel (a) shows spectra near the anode region and (b) shows spectra near the collector region. 2PG bands system are clearly seen in panel(b) corresponding to the existence of many secondary electrons.

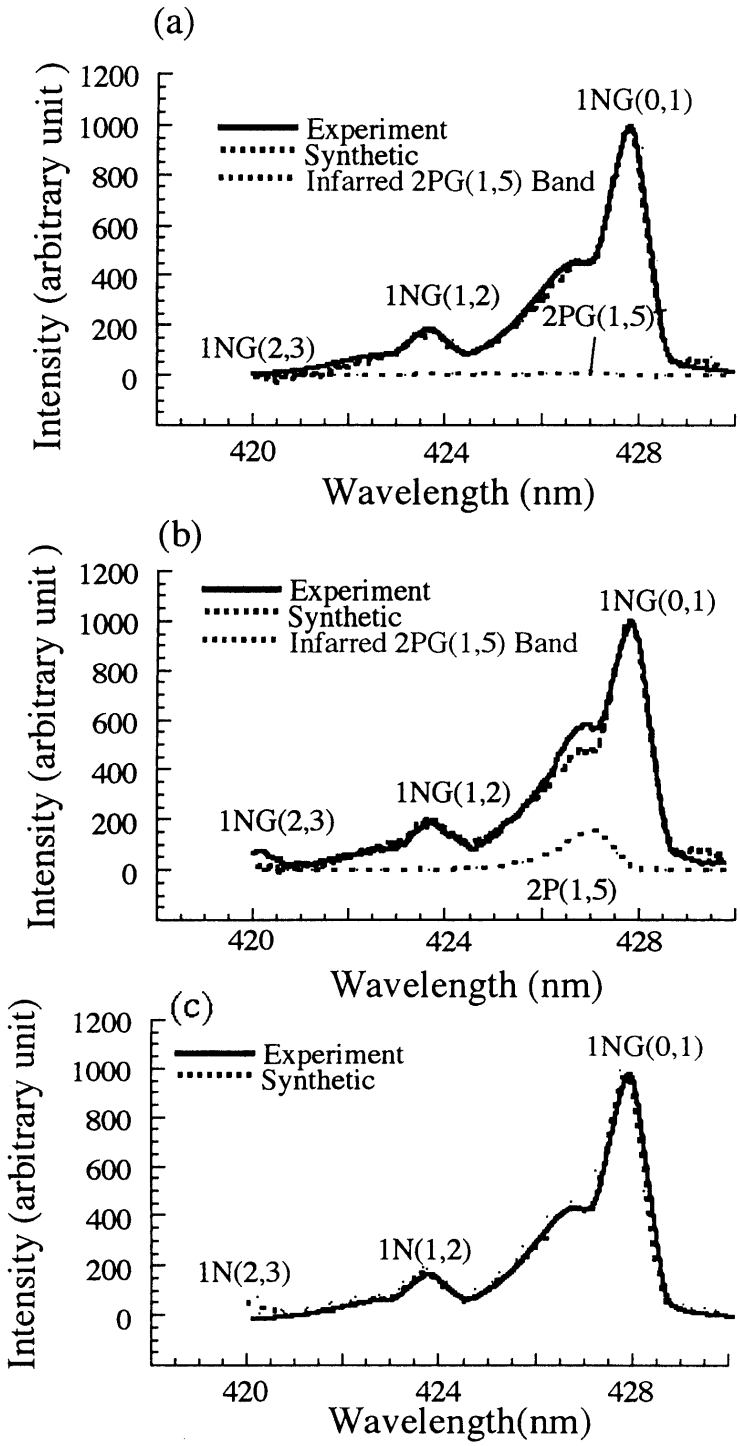

Fig. 3-10: The spectrum of N_2^+ and N_2 in the wavelength region 420nm - 430nm under the condition of Fig. 3-8(b).
The panel (a) and (b) shows spectra near the anode region and the collector region respectively. The solid line shows experimental spectra. The black dotted line shows synthetic spectra for Tv=800, Tr=400. The gray dotted line shows 2PG(0,5) band inferred 2PG(1,5) band. The panel (c) shows a spectrum after 2PG(1,5) band was subtracted from the panel (b). (See text).

overlapping of 2PG(1,5) to 1NG(0,1) deforms the profile of 1NG(0,1) band , which results in serious difficulty in determing the Tr by using fitting method. But the intensity of buried 2PG(1,5) band can be inferred from another independent spectrum, 2PG(1,3) as follows.

$$2PG(1,5) = \frac{A(1,5)}{A(1,3)} 2PG(1,3)$$

A(v', v_2") is transition probability of $N_2C^3\Pi_u$ (v=v')$\rightarrow N_2B^3\Pi_g$(v=v_2"). As 2PG(1,5) and 2PG(1,3) belong to the same upper vibrational level, the intensity ratio of 2PG(1,5)/ 2PG (1,3) is dependent neither on vibrational distribution of $N_2X^1\Sigma_g^+$, nor on excitation process $N_2X^1\Sigma_g^+ \rightarrow N_2C^3\Pi_u$ The lower panel of Figure 3-10 shows the spectrum after 2PG(1,5) was subtracted from the original 1NG(0,1) spectrum. The fitting was excellent and reproduced the same Tr of 400K as upper non-secondary electron effect spectrum. The reason why Tr was obtained to be higher than room temperature of 300K was because the vacuum chamber size was not so larger than the electron beam scale size, thus electron beam bombarded on and heated the chamber wall and consequently heated the target gas.

As overlapping effect is *linear,* we can remove the effect of secondary electron in Tr measurement. But there is inevitable problem which cannot be subtracted by data analysis, such as the break down of the optical selection rule in excitation process by low energy electrons [Hernandez,1982]. We examined the intensity ratio of the R-branch to P-branch of 1NG(0,0) band versus various projectile electron energies. The ratio should be dependent only upon Honl-London factor if the optical selection rule is applied for excitation process. The reason why we selected 1NG(0,0) band other than 1NG(0,1) band was that 2PG(1,5) band overlapped the R-branch of 1NG(0,1) band. Figure 3-11 shows the result. The ratio was found to be constant with electron energy >50eV. But it increased with decreasing the projectile energy <30eV. This fact suggested the breakdown of the optical section rules below 30-50eV. This fact does not contradict the conclusion of Culp[1967] and Hernandez [1982]. Hernandez [1982] stated that the projectile electron energies > 800eV should be used in order to completely satisfy the optical selectrion rule.

Considering our experimental result together with the conclusion of Hernandez [1982], projectile electron energies of 800eV is lower limit to obtain Tv and Tr which accurately reflect the vibrational - rotational distribution of the original N_2 ground state.

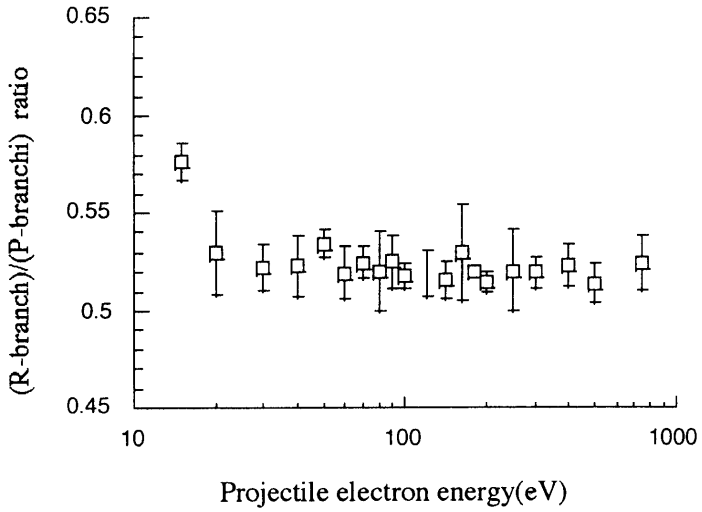

Fig. 3-11: Ratio of intensities of the R-branch and P-branch of 1NG(0,0) band in collisions of 10-2keV electrons with N_2.

Ⅳ INSTRUMENTATION OF THE ROCKET BORNE-SYSTEM

Ⅳ-1 THE ROCKET BORNE SYSTEM

Ⅳ-1- 1 Configuration

The rocket born instrument to measure the vibrational and rotational temperature of molecular nitrogen described in this chapter is an adaptation of a technique that is previously examined in the laboratory. Figure 4-1 shows a sketch of the instrument of N_2 Temperature of Vibration (NTV). This configuration is almost the same as O'Neil [1974]'s and Deleeuw [1972]'s. NTV is composed of two parts; an electron gun to excite and ionize ambient atmospheric molecular nitrogen, and a photospectrometer to detect luminescence (1st Negative Band) from ionized molecular nitrogen. It is seen that the electron beam is perpendicular to the rocket axis and hence to the approximate direction of flight and collected by the Faraday collector to provide a return circuit for the electron beam. This is important because the electron beam current is about 2-3mA and a current of this magnitude without positive return would lead to serious difficulties of charging up of the rocket body potential. This effect is described later. The field of view of the spectrometer is ($1.68^\circ \times 0.05^\circ$) in size, and is titled 60° away from the rocket axis to avoid seeing the Faraday collector surface where many secondary electrons are emitted. The observation region is the intersection of the electron beam and the field of view of the spectrometer . The central point of observation is chosen at a distance of 285mm from the rocket axis in order to avoid disturbance caused by any shock wave formed by the rocket motion. The observation region is limited to a small region around this point by the arrangement of the optical system, effectively 15cm long and with a equivalent diameter of about 2mm.

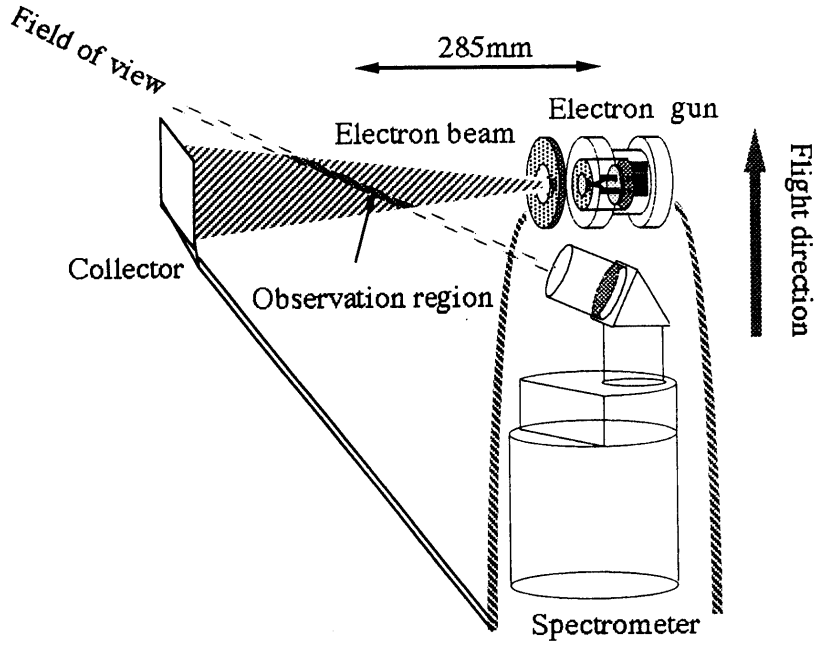

Fig. 4-1: Instrument configuration.

IV-1-2 Electron Gun

The schematic configuration of the electron gun is shown in Figure 4-2. The beam system is operated at potentials of 1030V and currents about 2mA. The electron gun is a conventional system composed of three stainless-steel electrodes, cathode, grid and anode at potentials of -1030V, -1360V and 0V respectively with respect of the rocket body potential. The cathode of 0.2mm diameter hairpin tungsten is directly heated by a dc current of 5.3A up to a temperature of about 3000K. The heating current is directly supplied from three rocket-born batteries which are attached linearly. Thermal electrons emitted from the heated filament are accelerated toward the anode through the orifice of 4mm diameter on the grid and then form an electron beam after passing through the orifice of 2mm diameter on the anode. As the beam electron energy is equal to the potential of the cathode , we can generate various beam energies by changing the cathode potential. The role of the negative grid bias is mainly to control the electron beam diameter. The gun operated at the cathode potential of -1030V and at the grid potential of -1360V produces a beam with a spot size of 10cm on the collector, 40cm distant from the last gun element. This fact is verified from the experimental picture of Figure 4-12. The beam is collected by the Faraday collector with a potential of 100V to provide a return circuit for the electron beam. A mesh at the potential of 50V is attached with the collector to prevent the emission of the secondary electrons. The electron gun was sealed in the vacuum chamber to avoid discharge induced by H_2O. The Figure 4-3 shows block chart of the electronics circuit of the electron gun. The electron gun is drawn on the upper-right in the Figure 4-3. The rectangular region enclosed by a bold shaded line is the region floated from the rocket body to about -1kV through a 1GΩ resistance and an isolation amplifier. A relay switch is utilized to turn on or off the cathode filament. We set six monitors to check the behavior of the electron gun system. The pirani gauge monitor is for watching the vacuum status in the electron gun chamber. It also gives the information of the opening the sealing cap by the rapid decreasing of the gas pressure. The anode voltage monitor and the grid voltage monitor is for watching the normal behavior of the high voltage supply without discharge. The heater current monitor is for watching the deterioration of the filament. The total current monitor is to measurement of the total emission current from the cathode. The collector current monitor is to measurement of the current which flows through the collector. We should note that the collector

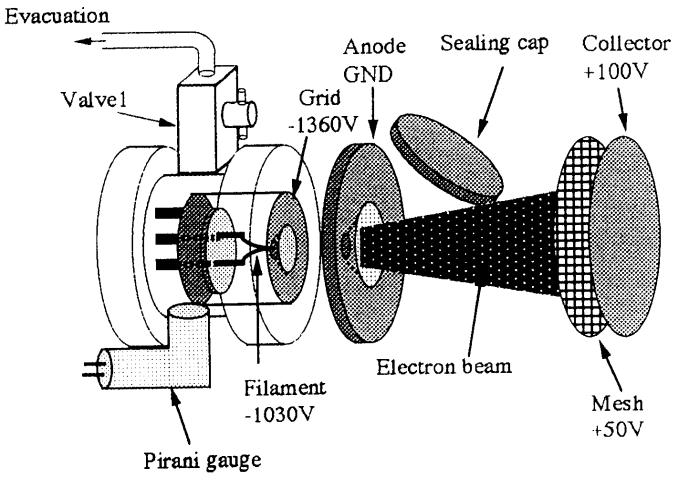

Fig. 4-2: Schematic configuration of the electron gun.

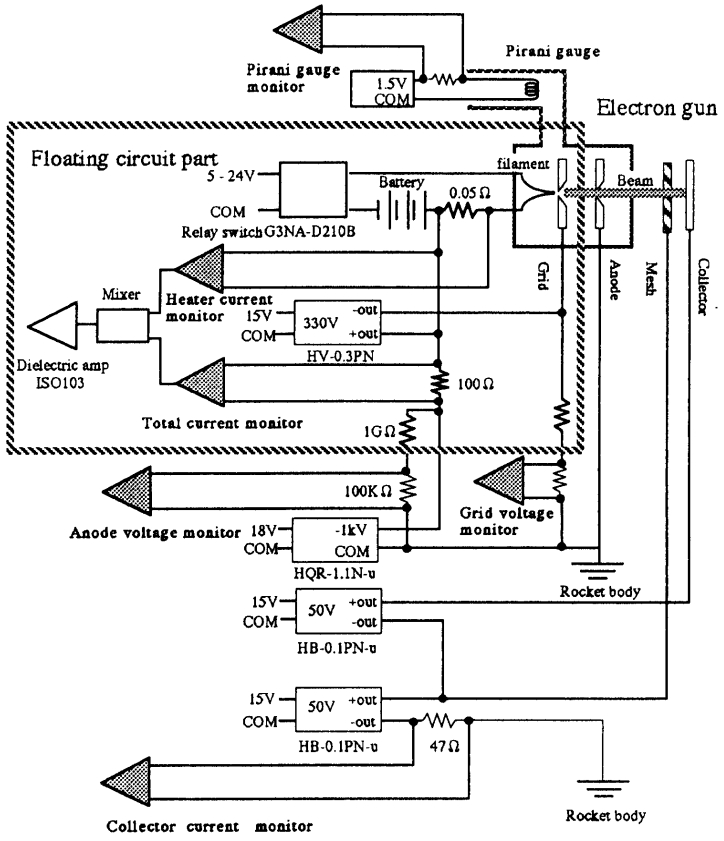

Fig. 4-3: The block diagram of the electronics circuit of the electron gun system.

current monitor measures only the fraction of the electron beam intercepted by the collector surface but the rest of the beam escapes into the space. We should also note that the collector is able to catch the background ionospheric electrons and secondary electrons. The contribution of the secondary electron to the collector current is not negligible in the pressure higher than 10^{-4} Torr.

Next, we describe the determination process of the optimum values of electron gun parameters such as cathode potentials (equals to beam energy) and so on above mentioned by experiments. The factors favoring the higher beam energy are , requirement of Franck - Condon theory which is valid for incident electron energies larger than hundreds eV and small beam deflection in the Earth's magnetic field. The factors favoring the lower beam energy are, to reduce the overall power requirement and to avoid the discharge between the electrodes. Considering the conflicting factors mentioned above, the beam energy is chosen to be 1030eV. Figure 4-4 shows the observed collector currents as a function of the cathode potential (I-V curve) for various cathode loading. The collector utilized in this experiment was 20cm in diameter and was set up about 10cm distant from the last gun element. Therefore the collector was able to catch whole beam electrons, thus the collector current indicated the same value as the beam current in this case. The grid potential was given to be 0V. The vacuum range is 2×10^{-4} [Torr] , corresponding altitude of 100km. The solid line shows space charge limited flow, dependent on the cathode potential and the shape of electrodes. The space charge limited flow is described as follows.

$$I\ (mA) \propto V^{3/2}[V]$$

If the beam current varied in accordance with the curve, beam current was only dependent on the accelerating potential and not on the cathode temperature. At the higher accelerating potential, the I-V curves departed from the space charged limited flow and transferred to temperature limited flow region , which is only dependent on cathode temperature proportional to cathode loading. If cathode potential of -1030V was applied, I-V curves were in the temperature limited flow region for any cathode loading in Figure 4-4. Higher cathode loading will produce a larger electron beam current which results in large signal-to-noise ratio of photospectrum. Thus we select high cathode loading of (5.3A × 2.5V) tolerable against deterioration of the filament under 10^{-4} Torr vacuum environment during rocket observation (~2 minutes). Figure 4-5 shows the observed total emission current and the collector current as a function of the grid potential. Accelerating potential was chosen to be constant value of 1030V. The total emission current monotonously decreased with increasing grid potential, but the collector current showed a maximum at 310V. The region where grid potential was larger than 310V, the collector current nearly was equal to total emission current. The beam efficiency defined as the ratio of the collector current to the total emission current was nearly 100% . The grid potential was chosen to be 330V for both requirements of the high beam efficiency and the large beam current.

The vacuum system of the electron gun is shown in Figure 4-6. The electron gun chamber is evacuated by using a rotary pump and a sorption pump to 5×10^{-5} Torr through 1/4 inch diameter pipe. The rubber hose is utilized in order to separate electrically the mechanical rotary pump from the fuel of the rocket booster. The gun chamber is baked by the heater wounded around the external wall of the chamber at the temperature of 120° C in order to clean the surface of the gun and the internal wall of the chamber for a few days. At 30 minutes before launching , 300Torr pure N_2 gas is injected into the chamber, the valve 1 is closed and finally the evacuation pipe is separated by the tool specially designed for this purpose.

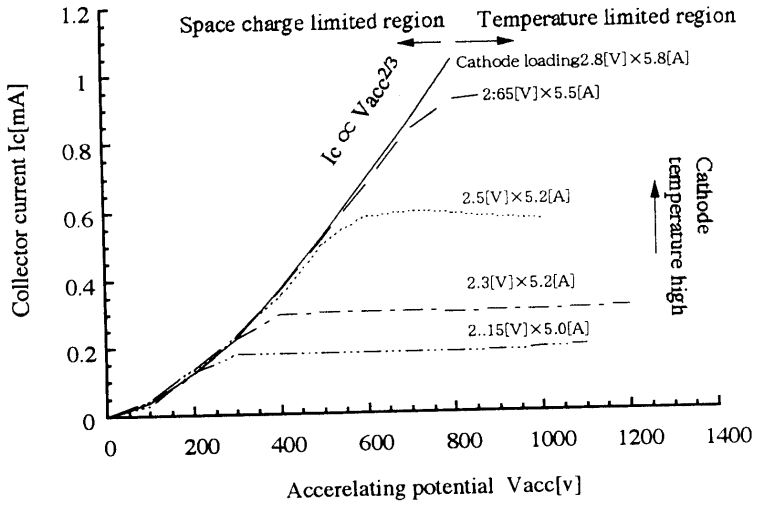

Fig. 4-4: Observed collector currents as a function of the cathode potential (I-V curve) for various cathode loadings.

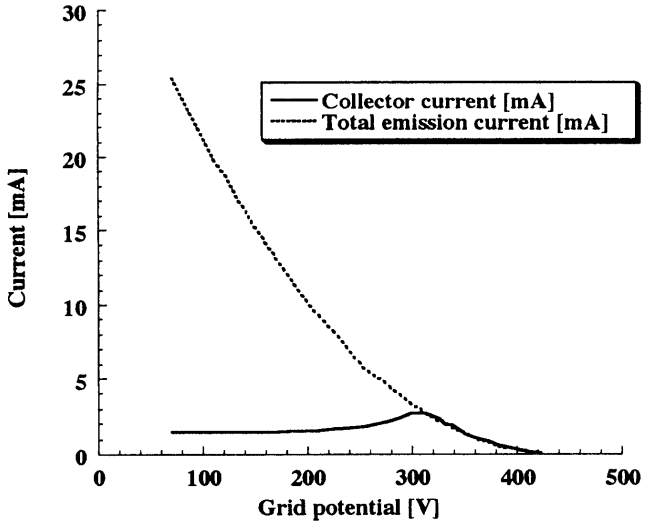

Fig. 4-5: Observed total emission current and collector current as a function of the grid potential.

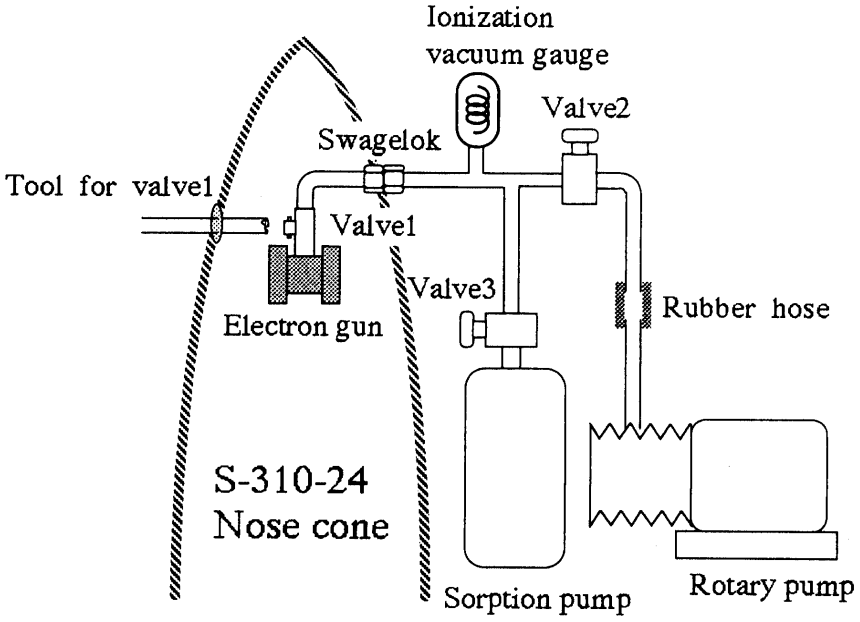

Fig. 4-6: The vacuum system of the electron gun.

IV-1-3 Details of the Detector System

The detector system is divided into two section: the spectrometer part and the detector part. Figure 4-7 shows the arrangement of the optical detector system. Luminescence from N_2^+ passes through a band-pass filter (central wavelength 410 nm, half-width 200 nm) and is focused by an objective lens (D=50 mm, f=170 mm) on to the slit (width 0.15 mm, length 5 mm) oriented along the electron beam direction. The optical path between the lens and the slit was carefully baffled so that only the field of view region was observed. The light from the slit is diffracted by a concave grating (D=60 mm, f=228 mm), amplified by an Image Intensifier (I・I) and detected by a linear 768 channel image -sensor. The spectrum profiles were obtained at intervals of 240ms. The image-sensor attached with I・I, on which high-voltage of 6kV was applied, was sealed in the gas chamber kept at the pressure of 1 atm to avoid discharge. Table 1 and table 2 shows specification of the spectrometer and the detector respectively. Figure 4-8 shows the block chart of electronics circuit of image sensor. Luminescence from N_2^+ is radiated on the cathode of I・I and converted into electrons by the photoelectric effect. Photoelectrons are amplified in the Micro Channel Plate (MCP) and converted into photon again thorough the screen of I・I. The gain is proportional to the voltage applied between input and output of the MCP. In this case, MCP voltage was applied at 1600V and the gain of MCP was 2×10^5. The exposure time of the 1024 channel linear image-sensor is 227.7 ms. The output of the analogue signal from the image-sensor is amplified , converted into digital signal and accumulated in a memory. The gain of the amplifier is designed to be changed from low mode to high mode at the altitude of 120km (during rocket ascent) or high mode to low mode (rocket descent) because the number density of N_2 decreases rapidly with altitudes. The resolution of the A/D converter is 12bit. The lower panel of Figure 4-8 shows time chart of the image-sensor. A/D convert starts at the same time of a master start signal. The output signal of one pixel of image-sensor is converted into a digital signal every 6 master clock signals (500kHz)with the frequency of 83.3kHz.

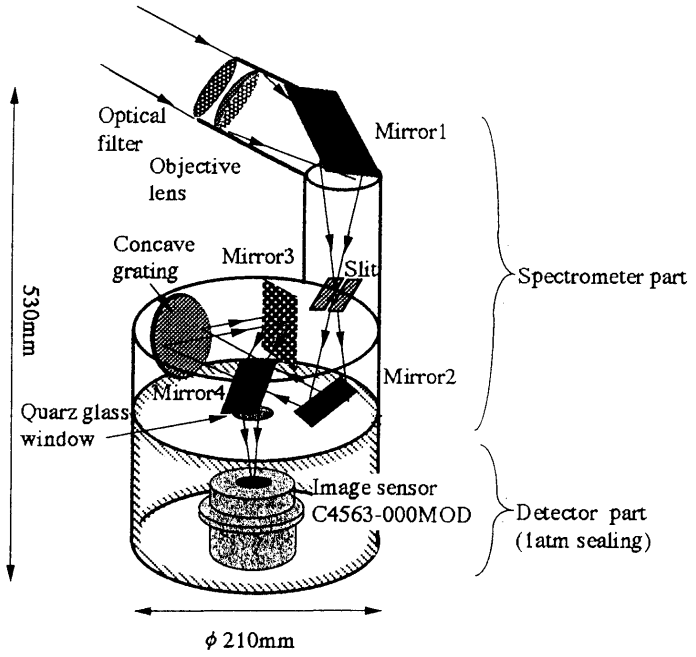

Fig. 4-7: The arrangement of the optical detector system.

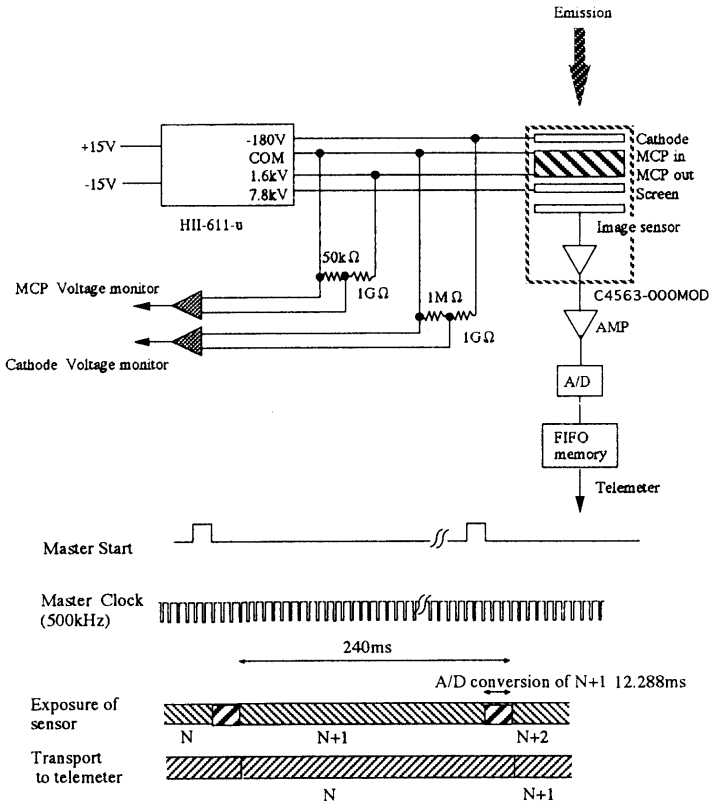

Fig. 4-8: The block diagram of the detector system.

It takes 12.288ms to convert 1024 pixels image analogue data into the digital data. We select 768 pixels including effective 700 pixels covered with I・I out of whole 1024 pixels. During the period of the next spectrum image exposure, previous spectrum data are transferred into telemetry. We can check the behavior of the applied high voltage to MCP and the cathode of I・I by two monitors through the telemetry.

Next, the calibration of the spectrometer - detector system was done and results were described. Figure 4-9(a) shows the spectrum of the mercury lamp obtained by the rocket - born spectrometer. The lamp lightened uniformly the whole field of view of the spectrometer by setting up the diffuser made of opal glass (SIGMA, DFO-50C-1) in front of the aperture of the spectrometer. The pixel numbers of the image sensor were converted into wavelength using by the known line wavelengths in Figure 4-9(a) and the grating equation described as follows.

$$\lambda\,[\mathrm{nm}] = \frac{\sin\alpha + \sin\beta}{10^{-6}\mathrm{M}\,[\mathrm{mm}^{-1}]}$$

Where λ is wavelength, α is incidence angle, β is diffraction angle and M is the number of grooves per mm. Figure 4-10 shows the result of the conversion. Figure 4-9(b) shows the enlargement of the mercury line of 404.66 nm in Figure 4-9(a). As this line was well-resolved from other lines, we took the line as a instrument function of the spectrometer to make a synthetic spectrum.The linear fitted curve was given,

$$\lambda\,[\mathrm{nm}] = 445.95 - 0.12464 \times \mathrm{N} \qquad (4\text{-}1)$$

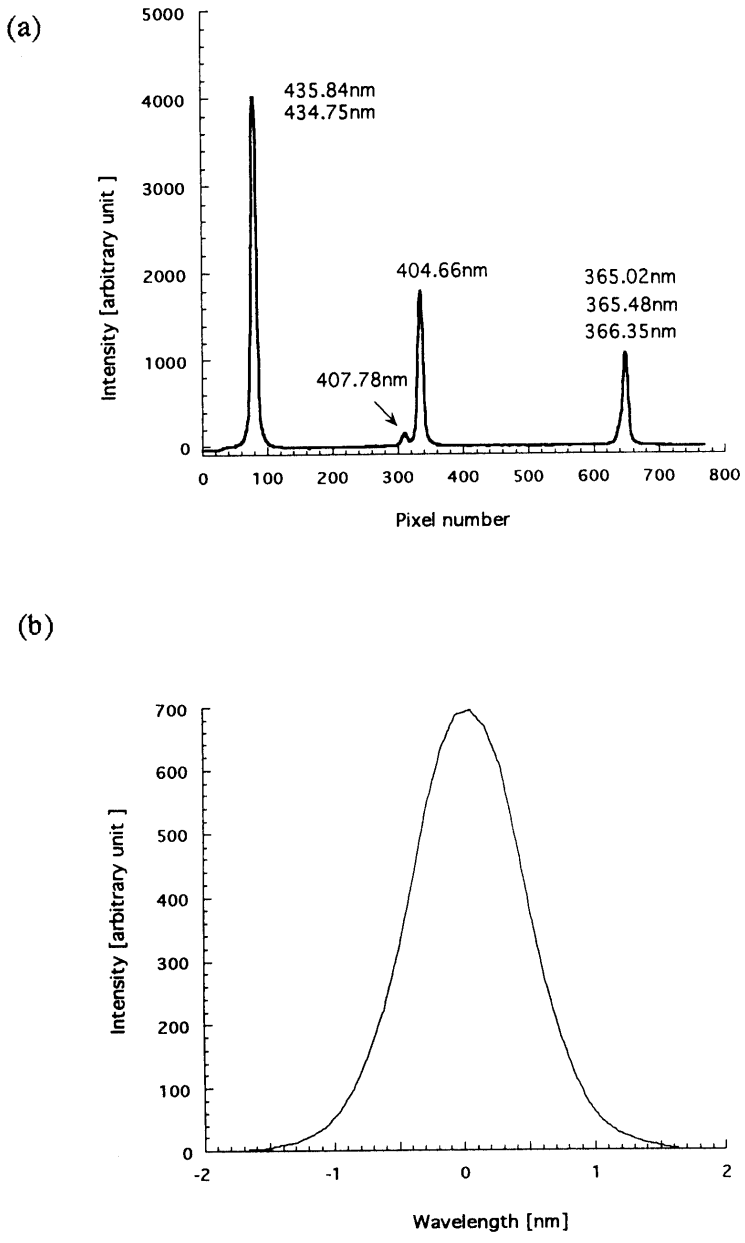

Fig. 4-9: The spectra of the mercury lamp.
Panel (a) shows the spectra in the whole wavelength region.
Panel (b) shows enlargement of 404.66nm line. This line was taken as a instrument function.

We adapt the calibration curve of Equation (4-1) for the conversion from pixel numbers into wavelength. The reciprocal linear dispersion (RLD) was determined from the first order coefficient of the Equation (4-1) to be 4.98 [nm / mm]. This value was a little bit larger than the specification value in Table 1. The sensitivity of the detector system was calibrated by using the standard deuterium lump (HAMAMATSU, L1626 - 40). The extinction filter (KENKO ND400) which reduce the light intensity by 1/400 available in the wavelength range of 400nm - 700nm was set up in front of the aperture of the spectrometer because the calibration lump was too strong for the high sensitive spectrometer. Figure 4-11 shows the intensity of the calibration lump averaged over wavelength range of 420nm - 440nm versus distance between the aperture of the spectrometer and the calibration lump. The test was done three times and all data were inversely proportional to the distance squared. This corroborated that standard lamp was fully caught in the field of view of the spectrometer. The calibration curve in Figure 4-11 were determined as follows.

$$Y\,[V] = \frac{179.5}{x^2\,[m]} \quad (R = 0.962)$$

Where Y[V] is the output voltage of the one pixel of the image-sensor and R is the correlation coefficient. Then the relation between the Y[V] and the photon count rate incident to the aperture of the spectrometer was derived.

$$I\,[\text{photon s}^{-1}] = 1.16 \times 10^6\ Y[V] \tag{4-2}$$

Or, in the unit of Reyleighs[R],

$$I\,[\text{kR nm}^{-1}] = 26.0\ Y[V] \tag{4-3}$$

Table 1 Specification of the rocket - borne spectrometer

Wavelength resolution	1.1nm
Effective wavelength range	356nm - 442nm
Slit dimension	width 0.15mm×length 5mm
Concave grating (Flat-field) Type Reciprocal linear dispersion Distance from slit to grating center Distance from grating center to image Grooves per mm Free aperture (Effective value)	 MILTON ROY 35-82-40-021 4.5nm/mm 231mm 225mm (λ = 380nm) - 251mm (λ = 780nm) 792.8/mm ϕ 95mm(60mm)、F2.4 (F3.8)
Objective lens Material Diameter Focal length	 Quartz 50mm 170mm
Band pass filter Type Central wave length Half width	 HOYA, B410 410nm 200nm

Table 2 Specification of the rocket - borne image sensor

Type	HAMAMATSU C4563-000 MOD
Wavelength range	195nm - 850nm
Window material	Synthesis quartz
Maximum sensitivity wavelength	430nm
Exposure time for 1 spectrum	240ms
Micro channel plate for I・I Gain of I・I	two stage 2×10^5 (at applied voltage of 1600V)
Effective dimension of image sensor Channel number (effective number) Cooling	17.5 (W) × 2.5 (H) mm 1024 (700) channel no-cooling of either I・I nor sensor

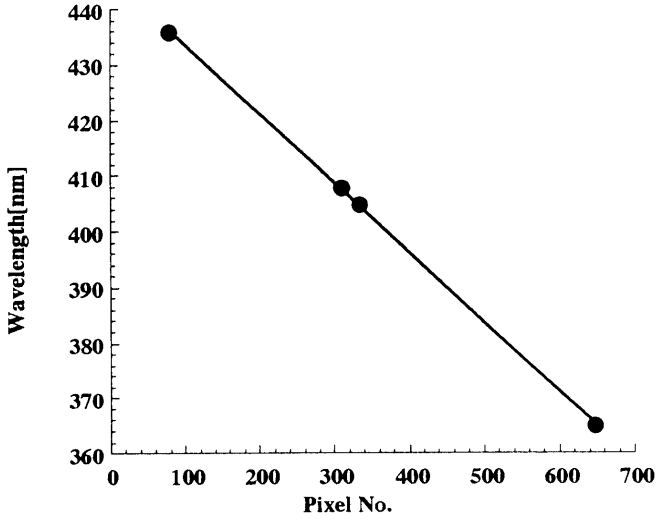

Fig. 4-10: The calibration curve between wavelengths and Image sensor pixel numbers.

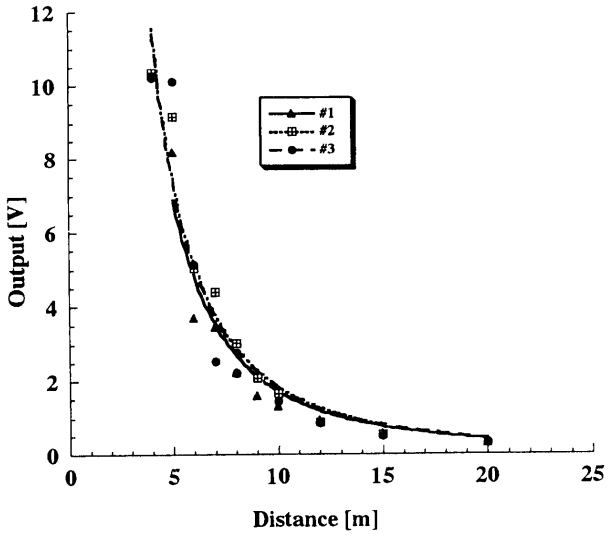

Fig. 4-11: The calibration of the sensitivity of the spectrometer.

IV-2 CHAMBER SIMULATION OF THE ROCKET-BORNE SYSTEMS

The whole instrument was put into the vacuum space chamber in the Institute of Space and Astronautical Science (ISAS) to check the behavior of the circuit in vacuum environment and to calibrate it for rotational temperature Tr and the number density N_0 of the molecular nitrogen. The gas pressure in the calibration chamber was measured simultaneously by a ionization gauge. Figure 4-12 shows the picture of the electron beam emission test at the pressure of 8×10^{-4} Torr , the simulated altitude of about 95km. NTV is the name of the payload, shown on the left. The blue light is the emission from the ionized molecular nitrogen , corresponding to the electron beam trajectory. Figure 4-13 shows the spectrum of electron beam induced luminescence of N_2^+ in the whole wavelength region of the payload system under the condition of Figure 4-12. The obtained spectrum were corrected for the change of the relative sensitivity of the photon detection system with wavelength. The spectrum intensity ratio of 1NG(0,0) [391.4nm] to 1NG(0,1)[427.8nm] should be equal to the ratio of the Einstein coefficient, $A(v' = 0, v_2" = 0) / A(v' = 0, v_2" = 1)$. The value of the ratio from Figure 4-13 is 2.81 and that of theoretical calculation is 3.07 [Gilmore, Laher and Espy, 1992]. We corrected the optical transmittance of the overall spectrometer - detector system by using the theoretical value of $A(v' = 0, v_2" = 0) / A(v' = 0, v_2" = 1)$.

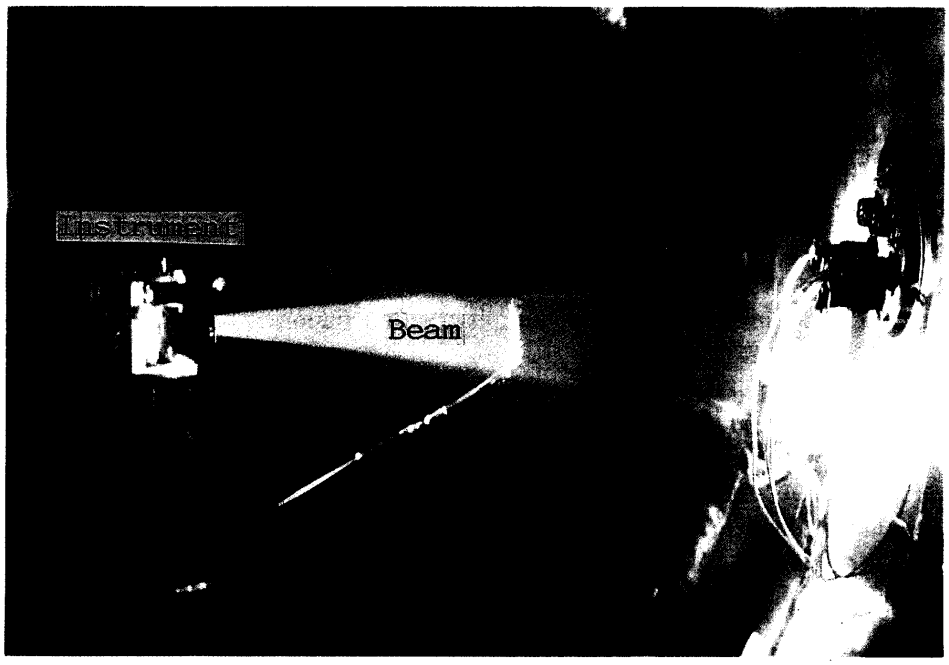

Fig. 4-12: A picture of the experiment in a simulation space vacuum chamber.
The pressure is 8×10^{-4} Torr, the same pressure at the height of 95km. The rocket - borne instrument is shown on the left. The blue light is the emission from the ionized molecular nitrogen, corresponding to the electron beam trajectory.

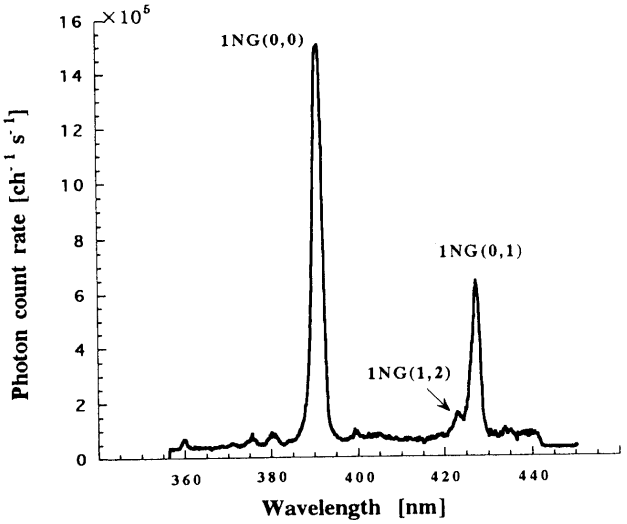

Fig. 4-13: A spectrum of N_2^+ and N_2 band emissions in the whole wavelength region of the payload system under the same condition as in Fig. 4-12.

IV-2-1 Number Density Calibration

The peak intensity of the spectrum for the same vibrational and rotational temperature is expected to be proportional to the number density of N_2 as shown in Equation (2-5). We modified Equation (2-5) in the particular case of 1NG(0,1) band emission.

$$N^{v'=0}_{v_2''=1}[\text{photon cm}^{-3}\text{s}^{-1}] = \frac{\sigma_{1NG(0,1)}\, i}{\bar{S}_{beam}\, e} N_0 \qquad (4\text{-}4)$$

Where N_0 is the number density of N_2, i is the electron beam current and $\bar{S}_{beam}$ [cm^2] is the average cross-sectional area of the electron beam in the observation region. $\sigma_{ING(0,1)}$ is the emission cross section of 1NG(0,1) band.

Figure 4 -14 shows the output of the image-sensor experimentally obtained data for various pressure range. The gain of the sensor amplifier was selected to be low mode. The number density was calculated from the nitrogen gas pressure detected by the ionization vacuum gauge using by the ideal gas state equation at temperature of 300K . Figure 4-14 shows the experimentally determined outputs were clearly linear with the densities. The calibration line shown in Figure 4 -14 as a bold solid line was determined by the least square method.

$$\begin{aligned} N_0[\text{cm}^{-3}] &= 1.76 \times 10^{12} \bullet (Y_{1NG(0,1)}\,[\text{V}] - \text{back ground}) \quad \text{(Low gain)} \\ N_0[\text{cm}^{-3}] &= 2.30 \times 10^{11} \bullet (Y_{1NG(0,1)}\,[\text{V}] - \text{back ground}) \quad \text{(High gain)} \end{aligned} \qquad (4\text{-}5)$$

The calibration for the high gain mode was done by using other data. We use Equation (4-5) to determine the number density from spectrum from now on.

Next, we try to determine Equation (4-5) directly from Equation (4-4). $\bar{S}_{beam}$ was calculated from the beam diameter measured in Figure 4-12. Assuming the beam electron current of 3mA . The value of $\sigma_{ING(0,1)}$ at the incident electron energy of 1keV is 1.7×10^{-18} [cm^{-2}]. This value was given by multiplying the emission cross section of 1NG(0,0) band [Borst, 1970] by the ratio of Einstein - coefficient of A(0,1)/A(0,0) = 0.33. Multiplying Equation (4-4) by the a factor G (geometry factor of the optical arrangement), the photon count rate incident to the objective lens I [photon s^{-1}] is derived.

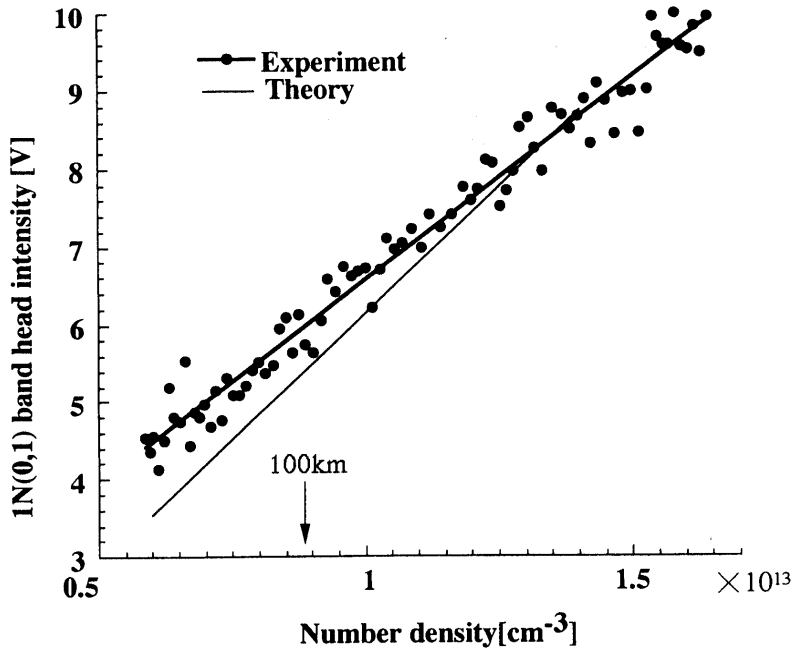

Fig. 4-14: The output of the image sensor of band head intensities of 1NG(0,1) versus number density of the N_2 by the chamber test. The bold line shows fitted curve and the thin line shows theoretical curve from Equation (4-6).

$$I\,[\text{photon s}^{-1}] = G\,N^{v'=0}_{v_2''=1} \qquad \left[G = \frac{1}{4\pi} A\,\Omega\,L\right] \tag{4-6}$$

where $N^{v'=0}_{v_2''=1}$ [photon cm^{-3} s^{-1}] is the volume emission rate of 1NG(0,1) band, A [cm^2] is area of the objective lens , Ω[sterad] is solid angle of the filed of view of the spectrometer and L[cm] is the length of the intersection of the filed of view of the spectrometer and the electron beam path. L was detemined from Figure 4-12. G was calculated to be 6.47×10^{-4} [cm^3 sterad]. Combined Equation (4-2) of the detector sensitivity calibration, Equation (4-4) and Equation (4-6) , the output voltage is

$$Y_{1NG(0,1)}\,[V] = \frac{G}{E}\,\frac{\sigma_{1NG(0,1)}\,i}{\bar{S}_{beam}\,e}\,N_0 \tag{4-7}$$

Where $Y_{1NG(0,1)}$ is the output voltage of the band-head of 1NG(0,1) band and E is the efficiency of the detector system, determined to be 1.16×10^6 [photon s^{-1} V^{-1}] in Equation (4-2). The thin line in Figure 4-14 shows theoretical curve calculated from Equation (4-7). Theoretical curve agreed with experimental calibrated curve. So both the calibrations for the number density and the sensitivity of the detector system were consistent with the electron beam excitation theory.

Combined Equation (4-2), (4-5) and (4-6) , volume emission rate of 1NG(0,1) band was determined as follows.

$$N^{v'=0}_{v_2''=1}[\text{photon cm}^{-3}\text{s}^{-1}] = 1.02\times10^{-3}\;N_0 \tag{4-8}$$

For example substituting N_0 =8.82×10^{12} [cm^{-3}] for the altitude of 100km after MSIS86 [Hedin,1987] in Equation (4-8), $N^{v'=0}_{v_2''=1}$ is determined to be 9.0×10^9 [photon cm^{-3} s^{-1}].

Ⅳ-2-2 Rotational Temperature Calibration

We obtained relatively high rotational temperature of about 350 - 400K in Chapter Ⅲ in the small chamber. While the volume of the space chamber utilized in the present experiment is very large compared to the electron beam scale, the electron beam does not heat the chamber wall by its bombardment. Therefore the rotational temperature is expected to be same as room temperature. Figure 4-15 shows spectrum obtained in the space chamber together with fitted synthetic spectrum. Tr was determined to be 270K from the spectrum. For corroborating the uniqueness of the optimum values of Tr, a example of contour map of fitting error for various FWHMs (Full Width of the Half Maximum) of the instrument function ($\Delta \lambda$) and for rotational temperatures (Tr) is shown in Figure 4-16. Fitting error is defined as Equation (2-7). Figure 4-16 indicates the uniqueness of the optimum value of Tr and $\Delta \lambda$. The optimum values of Tr and $\Delta \lambda$ were determined to be 270K and 1.5nm respectively at the minimum fitting error of 0.034. The reason why optimum $\Delta \lambda$ was larger than FWHM of the observed instrumental function determined from the mercury lamp as shown in Figure 4-9(b) by 40 -50% was not well-understood. But the valley of the contour was nearly perpendicular to the x-axis, which meant that the optimum Tr was dependent on $\Delta \lambda$. Therefore we should be careful to estimate the error in determining Tr. Temperature error was mainly attributed to signal-to-noise ratio of spectrum, which decreased with decreasing gas pressure. Figure 4-17 shows Tr for various pressure range. We conducted experiments for two pressure range, $2 \sim 8 \times 10^{-4}$ and $1 \sim 6 \times 10^{-5}$. We determined Tr not only from 1NG(0,1) band but also from 1NG(0,0) band. The band-head intensity of 1NG(0,0) band saturated for the condition of high gas pressure experiment. Therefore we got only data from 1NG(0,1) band for the condition of high gas pressure experiment. Tr was determined to be 265.7 ± 8.4K for high gas pressure condition, corresponding altitude of about 100km. Tr were also determined to be $247.5\text{K} \pm 41.2$K for 1NG(0,0) band and 294.5 ± 45.2K for 1NG(0,1) band for the low gas pressure condition, corresponding to an altitude of about 120km. Room temperature was about 280K on 12th January 1996. The measured rotational temperature agreed with the real gas

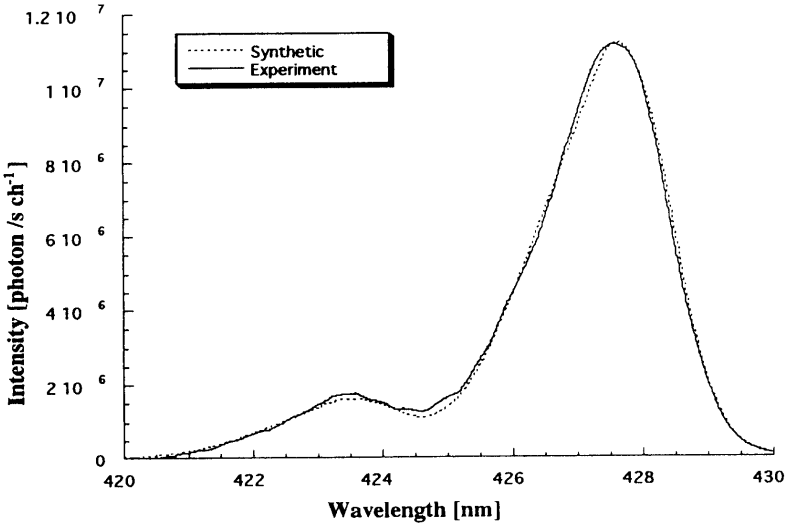

Fig. 4-15: The spectrum of N_2^+ in the wavelength region 420nm - 430nm.
Solid line shows experimental data and dotted line shows synthetic fit.
The gas pressure is 8×10^{-4} [Torr].

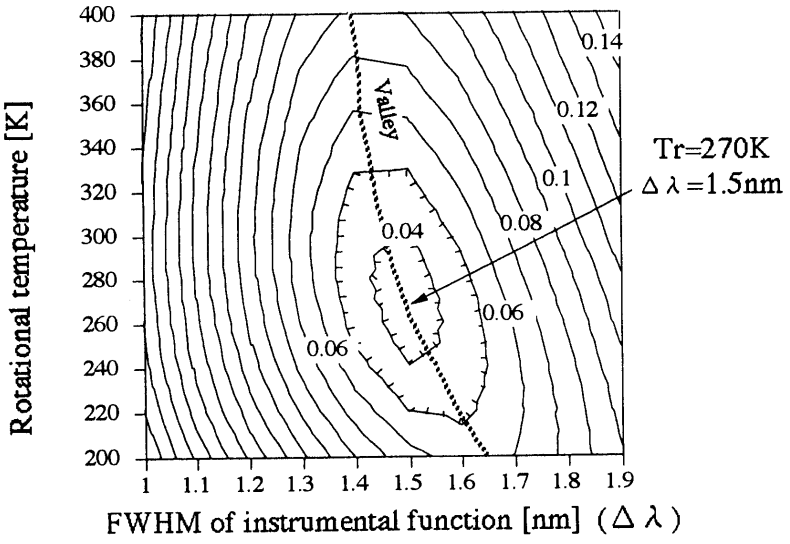

Fig. 4-16: Contour map of the fitting error versus Tr and FWHM of the instrument function.

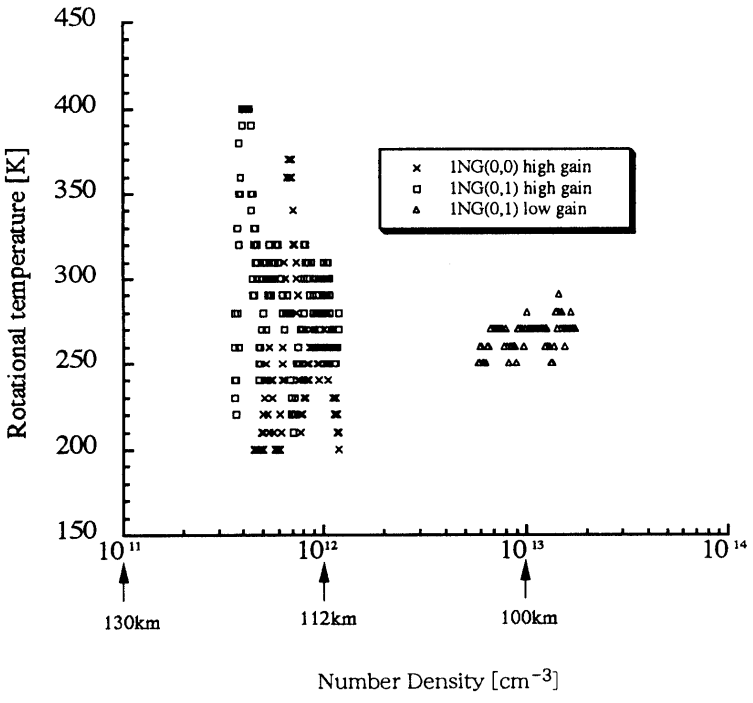

Fig. 4-17: Tr measurement versus number density of N_2.

temperature with an error of about 10K for high gas pressure condition, which means we can determine Tr at 100km with an error of 10K. For low gas pressure condition, the error was about 50K, which means we can determine Tr at 120km with the error of about 50K. At higher altitude, error of Tr will reach 100K at 140km, and the reliability of the Tr measurement will be small.

Ⅳ-2-3 Plasma Environment Test

We conducted impedance probe experiments simultaneously in a vacuum chamber to estimate the secondary electron production. Figure 4-18 shows the electron density measured by an impedance probe versus the gas pressure. As might be expected , secondary electron production increases with increasing the gas pressure. Figure 4-18 also shows current which flows through Faraday collector. As mentioned above the collector also detect the back ground electrons such as secondary electrons other than the primary beam electrons, the collector current also increases with increasing the gas pressure. Therefore we should be careful that collector current includes the contribution of the secondary electrons and the background plasma electrons. The increment of the collector current can be estimated by using Langmuir's space charge limited flow. If the geometric size of the high potential region (so-called *electron sheath region*) is much larger than Faraday collector and this condition can be realized for the applied potential of 100V in the plasma of electron density of 10^3 - 10^5 cm^{-3}, Current-Voltage relation is described [Linson, 1969],

$$\phi \approx 1.17 \times 10^3 \, I_0^{-1/2} \, I^{7/6} \tag{4-9}$$

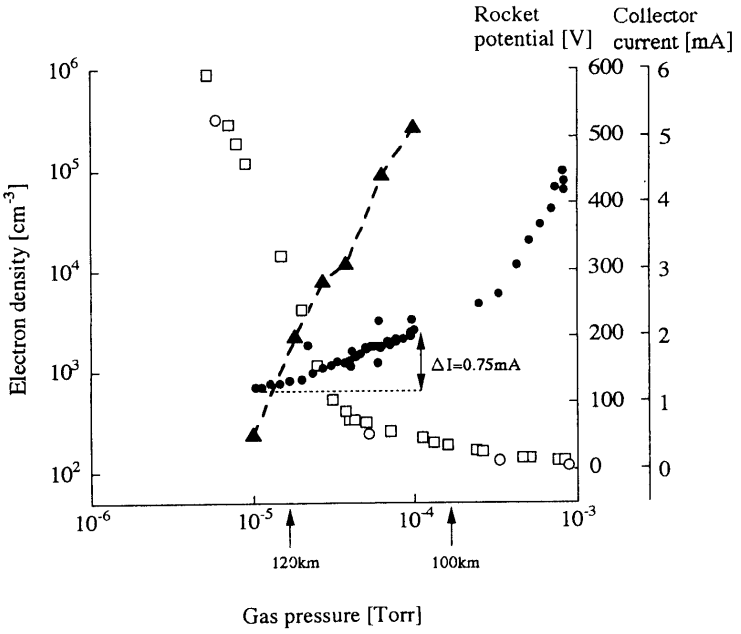

Fig. 4-18: Floating rocket body potential in the space chamber.
Electron density measured by the impedance probe and collector current of the electron beam are also plotted. Secondary electrons produced by electron beam increase with increasing gas pressure.
These electrons return to rocket body and prevent it from positive charge up.
-▲- Electron density, □Rocket potential #1, ○Rocket potential #2,
●Collector current.

where ϕ is the applied potential of the Faraday collector, I_0 is the thermal current intercepted by the cross - sectional area of the Faraday collector, and I is the effective current to the Faraday collector. I_0 is limited by the ambient thermal current density j_0 multiplied by twice the cross-sectional area, S=7.2×10^{-3} [m^2].

$$I_0 = j_0\, 2S \qquad \left(j_0 \equiv \frac{en_e\bar{c}}{4}\right) \tag{4-10}$$

Where j_0 is current density, n_e is electron number density and $\bar{c}$ is thermal velocity of electron. The typical electron thermal speed ,$\bar{c}$ is 1.2×10^4 m/s for the electron temperature of 300K. ϕ=100V is substituted for equation (4-10), and get a relation between I and n_e

$$n_e[cm^{-3}] = (4.9I)^{7/3} \times 10^4 \tag{4-11}$$

Where I is in unit of mA. The observed increment of Faraday collector current probably due to the secondary electrons was ΔI=0.75mA at 1×10^{-4} [Torr] as shown in Figure 4-18 , and we obtained the electron density of 2.1×10^5 [cm^{-3}] using Equation (4-11). This value agreed with observed value of 2.7×10^5 [cm^{-3}] by impedance probe. Therefore the Faraday collector can be useful as a probe to detect the background electron density, and the density can be compared with the values from the impedance probe.

The rocket body potential may go up if there is the incompleteness of the return circuit of the electron beam, for example the beam electrons missing the collector and escape into the space. If the floating rocket potential goes up to the level comparable to accelerating potential of the electron gun, the beam electrons may be de-accelerated by the negative electronic field around the rocket body, or in the worst case, electron beam cannot reach the observation region. Therefore it is important to estimate to what extent the rocket charging potential may go up. We made the stainless cylindrical shape model of the rocket body, with the diameter of 30 cm and the length of 60cm. The conductive surface area of the model was as smaller than that of the sounding rocket S-310 by a factor of 10. The Faraday collector was not attached on the model, thus the no beam electron could return. We installed it in the space chamber and it was floated electrically from the space chamber. The floating potential of the model rocket body was measured during the electron beam emission experiment for various gas pressure range. The experiment was done twice to confirm that the data were reproducible. The experiment was not done simultaneously with the impedance probe, but the data were overplotted in Figure 4-18 for comparison. The potential of the rocket body was lower than 100V in the case of the gas pressure above 5×10^{-5} [Torr], while it went up rapidly below 10^{-5} [Torr] and reach the level comparable to the electron beam potential. The electron sheath around the rocket body extended with increasing rocket body potential. Thus the sheath was able to collect more thermal electrons than ever. Therefore the rocket body potential was the result of the balance between the out-going beam electron current and the incident thermal electron current which increases proportionally to the geometric size of the electron sheath. Equation (4-9) is thus available again also in this case. I is the electron beam current and I_0 is the thermal electron current intercepted by the rocket body and ϕ is the floating potential of the rocket body. I_0 was calculated to be 2.71×10^{-6} [A] and ϕ was calculated to be 250V and 790V for the electron density of 10^4 [cm^{-3}] and 10^3 [cm^{-3}] respectively . The ionospheric electron density in the E region is expected to be in the range of 10^3～10^4 [cm^{-3}]. The calculated ϕ agreed with the measurement value in Figure 4-18 with a factor of 2. As the conductive surface of the real sounding rocket is 10 times larger than the model, the floating potential is expected to be 79V and 250V for the electron density of 10^4 [cm^{-3}] and 10^3 [cm^{-3}] respectively without the Faraday collector . If Faraday collector will be attached with the rocket body, it can collect 30% of the beam electron, consequently the floating potential of the rocket body will be reduced by 38%. Therefore the role of the Faraday collector is very important. As a conclusion, the floating potential

of the real sounding rocket is expected to be below 200V in the worst case. It does not significantly affect the observation.

Figure 4-19 shows the band intensity ratio 2PG(0,2)/1NG(0,1) versus the number density of N_2. The ratio 2PG(0,2)/1NG(0,1) gives information of the abundance of secondary electrons in the observation region mentioned in the Chapter Ⅲ. The 2PG band appeared notably in the particular pressure range of $1\sim4\ \times10^{-4}$ [Torr] corresponding to the altitude of 100km. The reason why 2PG band disappeared suddenly at 3.5×10^{-4} [Torr] was not understood. As the life time of $N_2C^3\Pi_u$ state is about 100ns, there is little probability of quenching by collision. Several estimates mentioned in Chapter I denote high vibrational temperature is realized around 100km, but the measurement in the altitude region is expected to be disturbed by the contamination of the secondary electron, as seen in Figure 4-19. Therefore we should analyze the rocket data in the altitude region of 100 - 110km with great care not to confuse the real high vibrational temperature with the effects due to the secondary electrons.

Ⅳ-2-4 Vibrational Temperature Calibration

There has been several estimates that Tv is enhanced to above 1000K in the thermosphere as mentioned in Chapter I .Therefore we should calibrate the instrument for several thousands Kelvins. The special calibration apparatus for the vibrational temperature measurement was installed in accordance with the apparatus of Hall et al. [1988]. The experimental set-up is shown in Figure 4-20. The rocket - borne spectrometer and the electron gun were installed separately for this experimental set-up. The N_2 gas once stagnate in the small cylindrical cell which is heated by a tungsten filament and is ejected into the collision chamber. The enlargement of the heating apparatus is shown in Figure 4-21. The cylindrical cell is made of stainless steel and has an internal diameter of 22mm and a length of 55mm. An operating gas temperature inside the cell of 2000K is obtained by heating a tungsten filament of diameter 0.6mm and length 50 mm for a current of 30A. Nitrogen gas of about 0.7 Torr pressure is in thermal equilibrium with the tungsten filament in a cylindrical cell. The gas temperature was measured by a thermocouple installed in the cell. The heated gas ejected through a

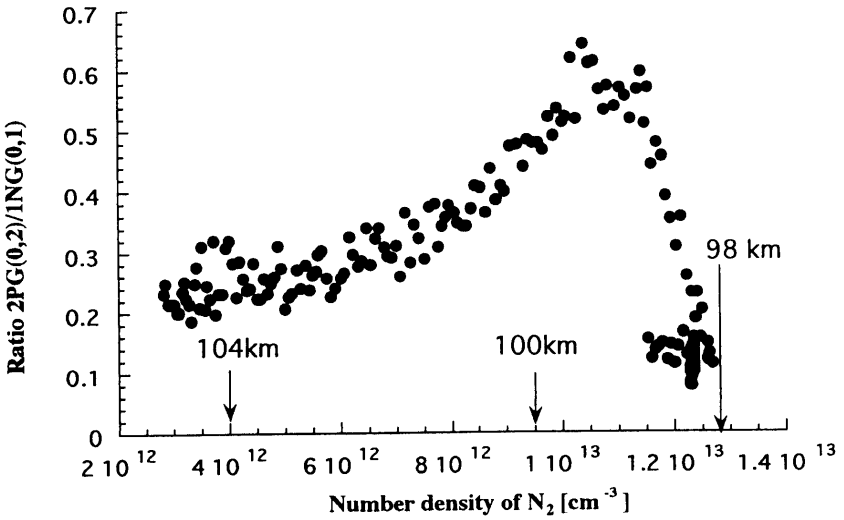

Fig. 4-19: The intensities ratio of 2PG(0,2)/1NG(0,1) versus gas pressure. 2PG(0,2) band clearly observed at particular gas pressure.

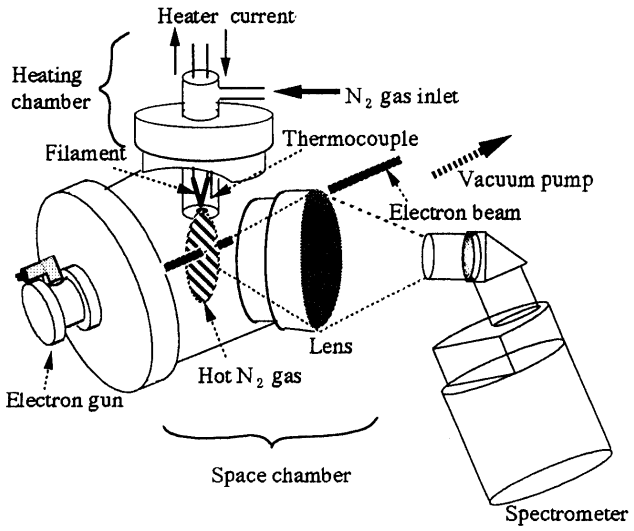

Fig. 4-20: Experimental set-up for vibrational temperature calibration system.

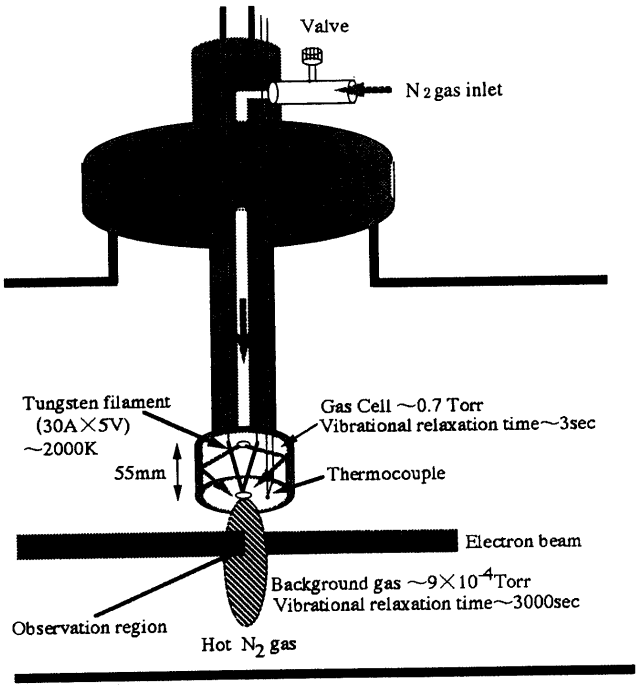

Fig. 4-21: Details of the heating chamber.

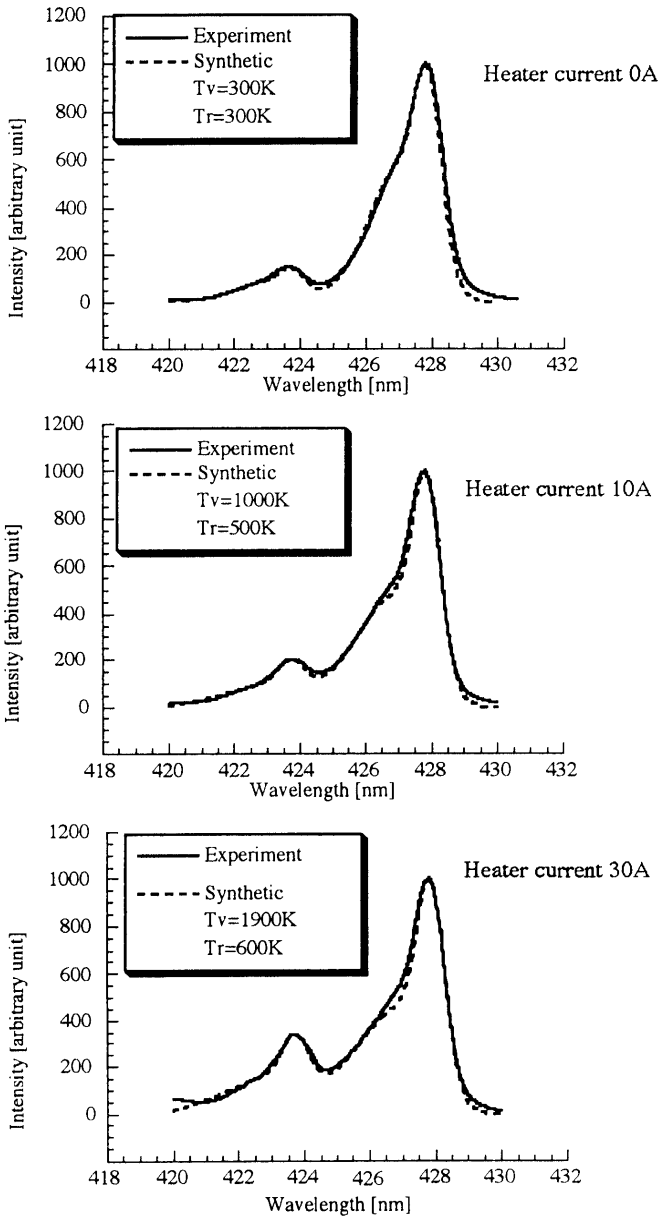

Fig. 4-22. Vibrationally excited spectrum for various heater currents. Synthetic spectrum are overplotted on the data. We can calibrate Tv with little overlap between 1NG(0,1) and 1NG(1,2) because of relatively low rotational temperature.

6mm ϕ orifice into the 10^{-3}-10^{-4} Torr pressure environment was crossed by an electron beam about 10 mm below the orifice. Since the solid angle of the orifice from the center of the cell is about 0.05 [sterad], the molecular nitrogen collides with the internal cell wall at least 20 times before being ejected through the orifice. The vibrational energy quenching rate by the solid surface is large, 5 times collisions are enough for the vibrational relaxation. Therefore the vibrational temperature of molecules in the cell is expected to be in equilibrium with the temperature of the cell surface, the tungsten filament and the translational temperature of the gas. But after being ejected into the collision chamber at 10^{-3}-10^{-4} Torr pressure, the nitrogen gas lose its vibrational energy by vibrational - translational (V-T) energy exchange. The time of V-T energy exchange is given by Vincenti and Kruger [1965],

$$\tau_{vT}[\mathrm{sec}] = 5.41\times 10^{-6}\ \frac{\exp\left[(1.91\times 10^{6}/T[K])^{1/3}\right]}{p\ [\mathrm{Torr}]} \qquad (4\text{-}12)$$

Substituting the back-ground pressure of 9×10^{-4} Torr , τ_{vT} is 1.14×10^{2} sec for T=800K and 3.83×10^{3} sec for T=2000K. Therefore the beam electron impacts ejected N_2 gas at the observation point much before it reaches equilibration with ambient gas at room temperature. The vibrational temperature determined from the observed spectrum is thus expected to be equal to the translational temperature found by the thermocouple. On the other hand, in this ejection process the translational temperature and the rotational temperature become about the room temperature at the observation point because of the fast rotational - translational relaxation time τ_{RT}[sec] of ~10 ms. Therefore a nonequilibrium condition, such that the rotational temperature is less than 400K, but the vibrational temperature are much greater , can made in expansion gas flow. As accounting for the overlap of the 1NG(0,1) band onto the 1NG(1,2) band is not a significant problem for rotational temperature below 400K, a precise determination of intensity ratios can be made in such a gas flow. Figure 4-22 shows thermally excited spectrum obtained for various heater currents in the experiment. The fitted synthetic spectra were overplotted on the spectral data. The discrepancy between vibrational temperature and rotational temperature was attributed to the difference of the relaxation times in the ejecting process mentioned above. Figure 4-23 shows that those two temperatures are in good agreement. But as mentioned in Chapter Ⅲ-1, this instrument has little resolution for Tv below 800K, the calibration was only meaningful for high temperatures above 1000K.

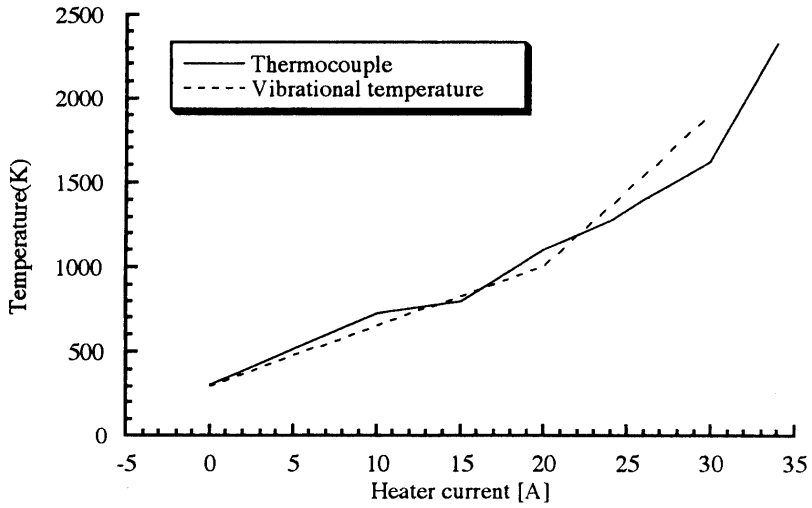

Fig. 4-23. Comparison of the temperature measured with thermocouple and the Tv determined from vibrationally excited spectra.

Ⅳ-3 Wind Tunnel Experiment

This section is devoted to the discussion of the effect of the shock wave disturbance produced by the supersonic rocket motion. The rocket ambient atmospheric gas is heated by shock wave disturbance through the conversion of the kinetic energy of the supersonic bulk flow against the rocket body into the thermal energy of the gas. The density of the rocket ambient air also increases due to the compression by the supersonic flow. As is expected from Rankine - Hugoniot theorem, the temperature increases by 8 times and number density increases by 5 times under the Mach number of 6. Thermally heated gas in turn distribute its translational energy to internal molecular energy through vibrational-translational energy exchange (V-T) process or rotational- translational exchange (R-T) process. As shown in Figure 1-2, the vibrational-translational relaxation time of N_2 at the height of 100 km is ~ 6000 s, and the rotational-translational relaxation time is ~ 50 ms. The rotational temperature measurement and number density measurement thus might be affected by the shock wave disturbance but the vibrational temperature measurement will not be. We have designed the rocket-borne instrument to avoid the shock wave disturbance in accordance with the numerical simulation results by Bird [1988]. We have made supersonic wind tunnel experiments in order to examine the shape of the shock wave using a 1/2 size model at the Institute of Space and Astronautical Science (ISAS). Two angles are defined as Figure 4-24 which determine the rocket attitude. The attack angle is defined as the angle between the flight direction and the rocket axis. The spin phase angle is defined as the angle between the electron beam direction and the plane which includes both rocket axis and the velocity vector. Generally, the shock wave disturbance is small for the small attack angle. Figure 4-25 shows the Schlieren picture of the wind tunnel experiment. The Mach number was 4 and the gas pressure inside the wind tunnel was 50 Torr. The attack angle was 15° and spin phase angle was 180° , which is the measurement condition most subject to shock wave disturbance because the shock wave generally expands toward the down stream region with respect of the rocket body. The schlieren picture generally reflects the change of the refractive index induced by the change of the density in the flow field. The red color region shows the compressed region and the blue color region shows the expansion region in Figure 4-25. Generally the shock wave is formed where the super sonic flow come into contact with the rocket ambient gas at first, subsequently ,the expansion wave is formed. The density compression is most enhanced near the shock wave front , while expansion effect increases with increasing the distance from the rocket body. Figure 4-25 shows the observation area was barely outside the shock disturbance even for the worst condition of the attitude. We concluded thus that the measurement would not be affected by the shock disturbance region during most of the flight under the condition of the attack angle of less than 15° . But on the rocket descent phase, the attack angle will be much larger than 15° . Thus the measurement on the rocket descent is expected to be in the downstream region where the expansion flow is dominant. Therefore measured density will be significantly lower than the real atmospheric density.

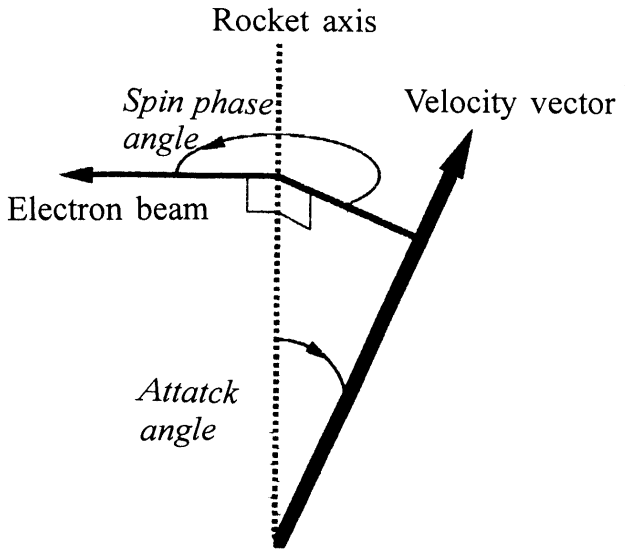

Fig. 4-24: Definition of the angle characterizing the rocket attitude.
Attack angle is the angle between the velocity vector and rocket axis.
Spin phase angle is the angle between the electron beam and the plane which includes both rocket axis and velocity vector.

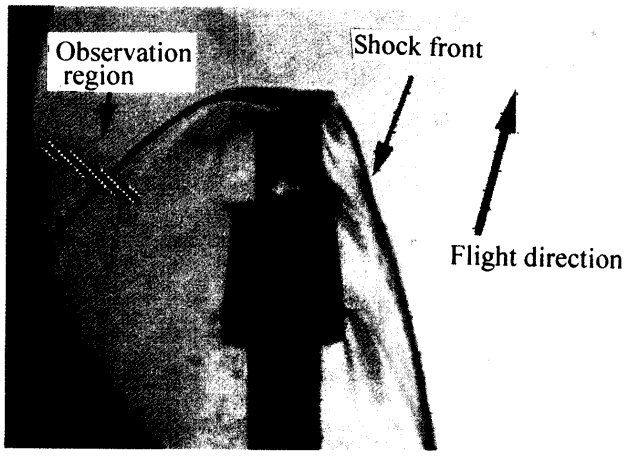

Fig. 4-25: Supersonic wind tunnel experiment.
Attack angle=15° and spin phase angle=180°

V ROCKET OBSERVATIONS AND DATA ANALYSIS

V-1 LAUNCHING CONDITIONS

The instrument was flown abroad the sounding rocket S-310-24 at Kagoshima Space Center in Japan on February 11, 1996 at 2000 JST. The geographic location of the launching site is 31.1°N and 131.3°E and geomagnetic location is 20.0°N and 198°E. The magnetic dip angle is about 40°. At this time ,the solar 10.7cm radio flux (F10.7) adjusted to 1AU was 68.2 (in units of 10^{-22} $Wm^{-2}Hz^{-1}$) and the sun spot number was 0. The monthly average value of F10.7 was 69.8. This means the solar activity was nearly at minimum in this period. The geomagnetic activity index Kp over three-hourly average including launching time was 3, meaning it is moderately disturbed.

Figure 5-1 shows the outline of the flight course of the rocket. The elevation angle and azimuth angle on launching were 78° and 135° respectively. The apogee altitude was 199km and the total flight distance was about 250km. The ionosphere sounder at Yamagawa, about 50km distant from the rocket launching center was operated in support of this experiment. The ionogram at the launching time

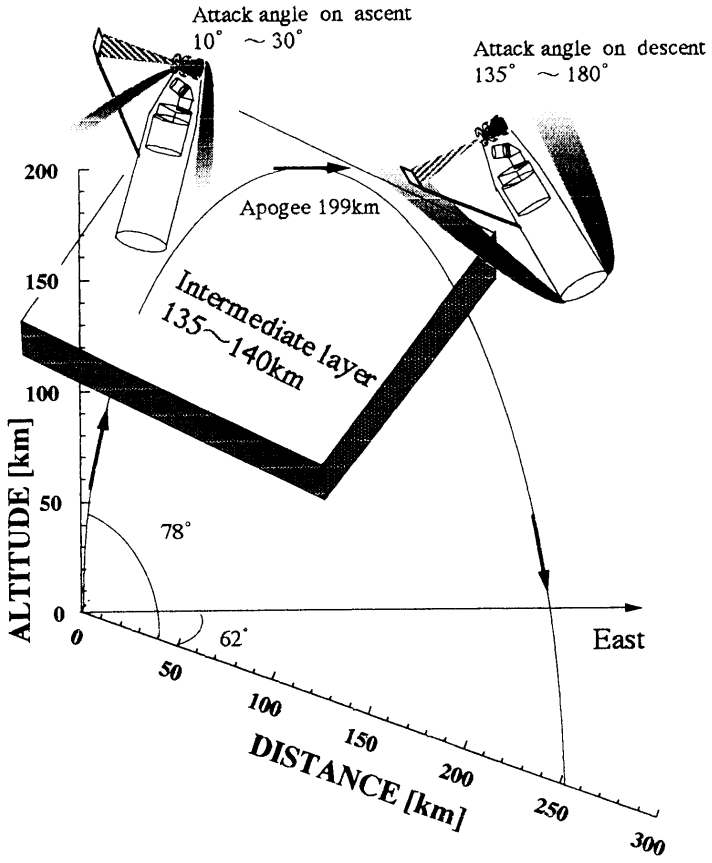

Fig. 5-1: The outline of the flight course of the rocket.
Ionization intermediate layer appeared at 135 - 140km altitude.

Figure 5-2 shows the appearance of the descending intermediate ionization layer at 139km.
Figure 5-3 shows the attack angle during the whole flight determined from the star sensor. The attack angle was in the range of 10° - 30° on the rocket ascent while 135° - 180° on rocket descent. Therefore the flow field on rocket ascent was the similar to that shown in Figure 4-25. The attitude was significantly important in analyzing the density data , and will be discussed later. The time sequence of the flight is shown in the Table 3. The cap of the chamber of the electron gun was opened at 57s after the launching (h=75.02km). This opening procedure was confirmed by the change of the vacuum range in the chamber measured by a pirani gauge. The filament was turned on at 68s and the high voltage for the electron gun and the I・I was turned on at 74s (h=99.46 km). From this moment, the electron beam was emitted toward the ambient atmospheric gas and the detection of the luminescence by the spectrometer began. At 97s (h=128.22 km), the amplifier of the image sensor changed its gain from the low mode to the high mode because the N_2 number density rapidly decreases in this altitude. The observation continued until the cathode filament was turned off at 127s (h=158.38 km). The observation during the down-leg was done from 323s (h=152.56 km) to 381s (h=81.78 km).

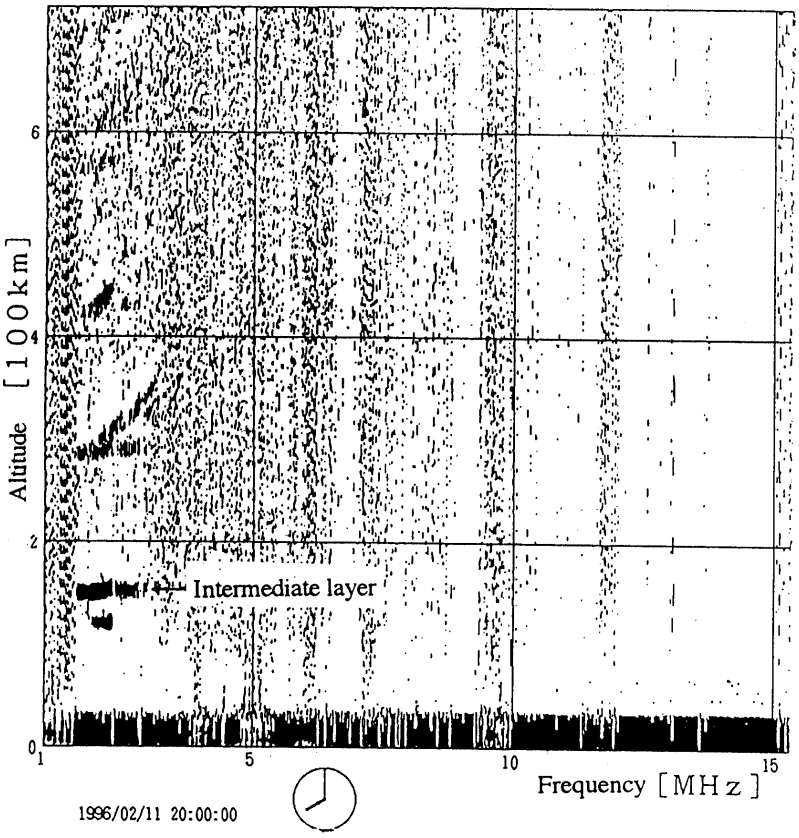

Fig. 5-2: The ionogram at Yamagawa at the rocket launching time. Ionization intermediate layer was observed.

Table 3: The time sequence of the souding rocket S-310-24

Time after lift off [s]	Expected altitude [km]	Real altitude [km]	Active item
48		60.97	Extend the impedance probe
57	75	75.02	Open the cap of the electron gun
68	91	91.14	Turn on the filament of electron gun
74	100	99.46	Turn on the high voltage (Begin the Observation on rocket ascent)
97		128.22	Change the gain of the sensor Low→High
127	160	158.38	Turn off the filament of the electron gun (Finish the Observation on rocket ascent)
138	170	167.34	Turn off the high voltage
312	170	162.12	Turn on the filament of electron gun
323	160	152.56	Turn on the high voltage (Begin the Observation on rocket descent)
346		128.81	Change the gain of the sensor High → Low
381	92	83.21	Turn off the high voltage (Finish the Observation on rocket descent)
382	91	81.78	Turn off the filament of the electron gun

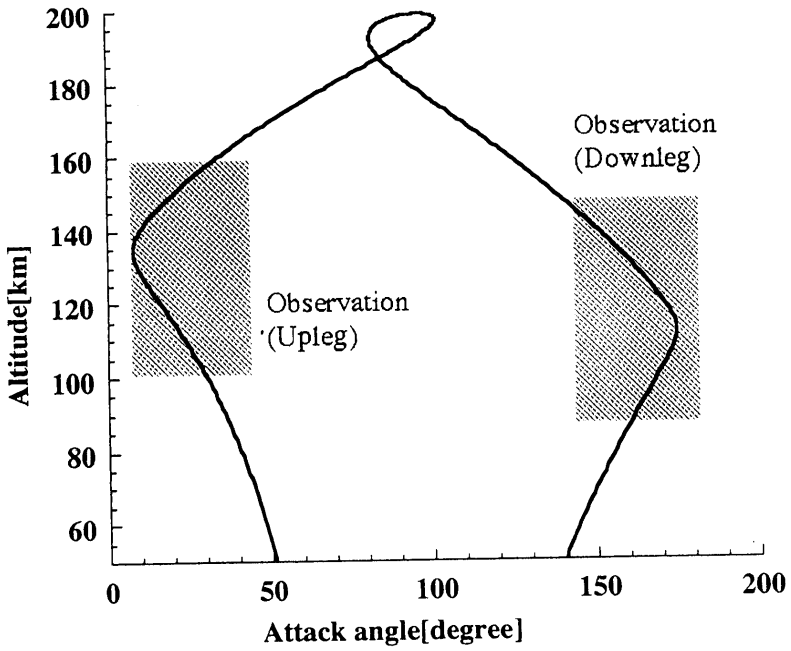

Fig. 5-3: Attack-angle of the S-310-24 during the flight
The observation was done in the altitude region of 99 - 158km on ascent, and 153 - 83 on descent.

V-2 Behavior of the Electron Gun and Plasma Environment Observation

The profiles of the Faraday collector current and the total emission current are plotted versus in altitude as shown in Figure 5-4. Both current data were obtained at major intervals of 5.12s. The sampling time of the total emission current and Faraday collector current were 160ms and 320ms respectively. Faraday collector current varied during the sampling time because the angle between the electron beam and the magnetic field, which determined the fraction of the beam intercepted by the Faraday collector, was changing cyclically over a period of 1s as the same period as the rocket body spin. Total emission current was almost constant with altitudes, which meant that the electron gun behaved normally without deterioration of the cathode filament. Below 110km, Faraday collector current was very large, even in excess of total emission current as shown in Figure 5-4. Electron density also showed large value in the same altitude region. This indicates the large production rate of secondary electron in these altitudes because of the high gas pressure, as observed in the space chamber experiment shown in Figure 4-18. Above 115km, where secondary electron production was no more dominant in the rocket ambient plasma environment, the contribution of the flux of the background ionospheric electrons to Faraday collector current became relatively large. Faraday collector current showed a peak around 135 ~140km altitude on the rocket ascent in Figure 5-4. The altitude profiles of the electron density measured by the rocket-borne impedance probe are shown in Figure 5-5. There was also a peak in altitude profile of electron density around 134km on the rocket ascent in Figure 5-5. The peak density was 2×10^4 [cm^{-3}]. But there was no clear peak on rocket descent in either Faraday collector current profile (Figure 5-4) nor electron density profile (Figure 5-5). The distance of the rocket position between on the rocket ascent and on rocket descent at 140km altitude was 137km. Therefore the horizontal scale of this enhanced electron density phenomenon along the rocket flight course was smaller than ~140km. The peak altitude of Faraday collector current agreed with the altitude of the intermediate layer of 139km shown in the ionogram , Figure 5-2. The peak electron density was also estimated from the Faraday collector current by using the Equation (4-12)

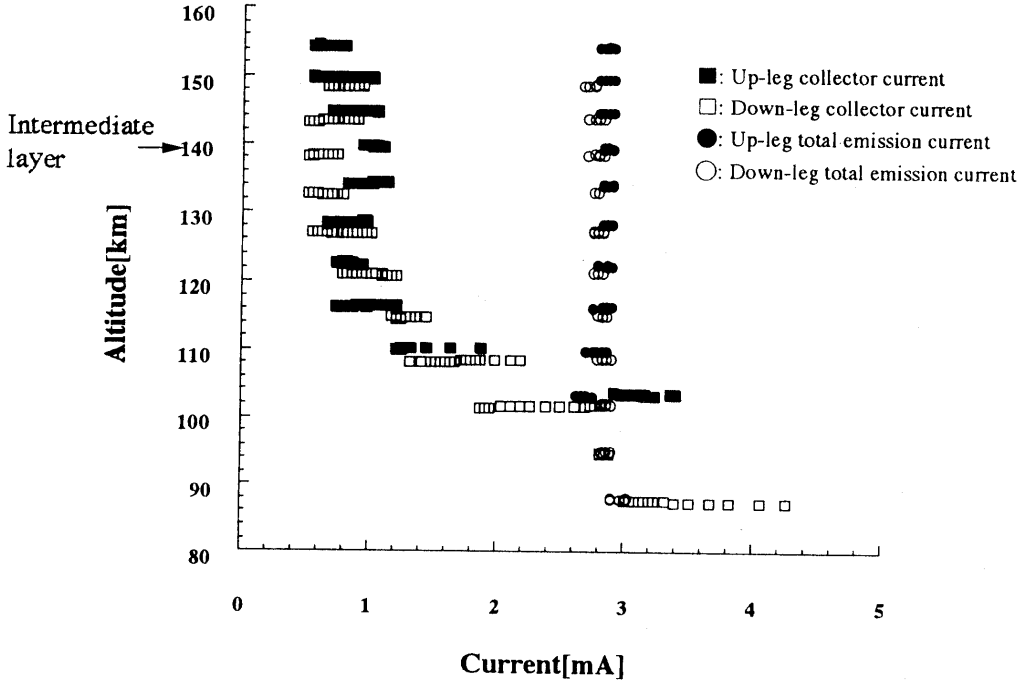

Fig. 5-4: Electron beam current profile in altitude during the flight.

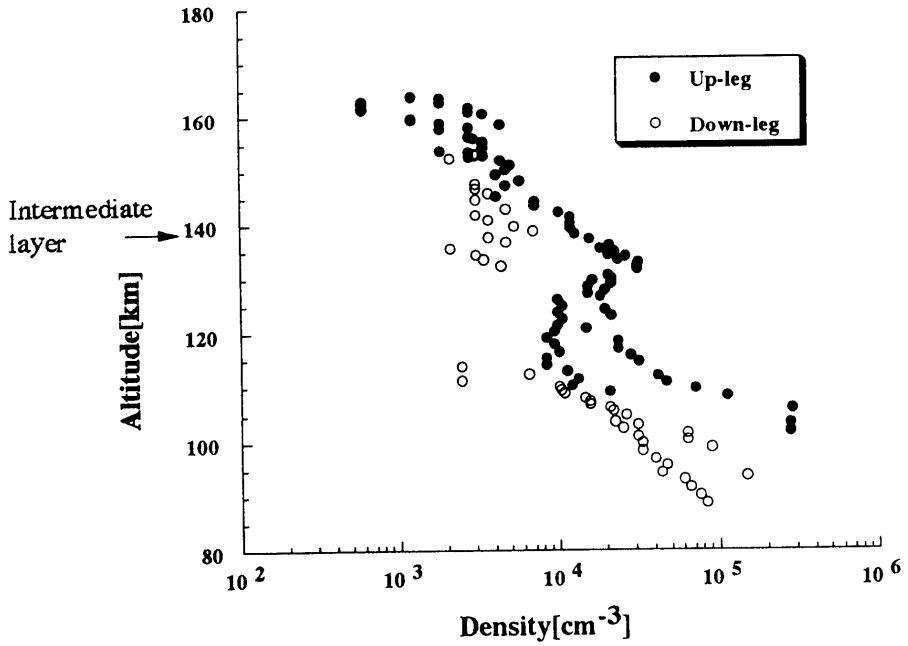

Fig. 5-5: Electron density profile in altitude during the flight by impedance probe.

$$n_e[cm^{-3}] = (4.9I)^{7/3} \times 10^4$$

Where I is the Faraday collator current in unit of mA subtracted the electron beam contribution. The observed value of increase of the Faraday collector current corresponding to intermediate layer is about I=0.3mA, and we get the electron density value of 2.5×10^4 [cm^{-3}]. This value agreed with the observed value of 2×10^4 [cm^{-3}] by impedance probe. Therefore it is concluded quantitatively that the increase of the Faraday collector current around 140km could be attributed to the enhanced ionospheric electron density in the intermediate layer. The further discussion about the intermediate layer will be found in ChapterVI.

V-3 Rotational Temperature and Number Density Measurement

Figure 5-6 shows a typical example of spectrum obtained at 100km by the rocket experiment in the whole wavelength region of the spectrometer. This section is devoted to determination of the number density from the peak intensity of the observed spectra using the equation (4-5) and rotational temperature by the synthetic spectral fitting to the observed spectra.

V-3-1 Outline of Measurement of Number Density of N_2

Figure 5-7 shows altitude profile of N_2 density on the rocket ascent obtained from running average over 20 spectra with an altitude resolution of 3km. N_2 densities were determined from the band head intensities of the 1NG(0,1) band by using the calibration Equation (4-5). The solid line and dotted line indicate the data on rocket ascent and descent, respectively. The dashed line is the value from MSIS86 model. Figure 5-8 shows the density perturbation defined as $(N-N_{MSIS})/N_{MSIS}$, where N is the observed N_2 number density and N_{MSIS} are MSIS86 values. The observed number density on the rocket ascent nearly agreed with MSIS values. But the observed number density values on the rocket

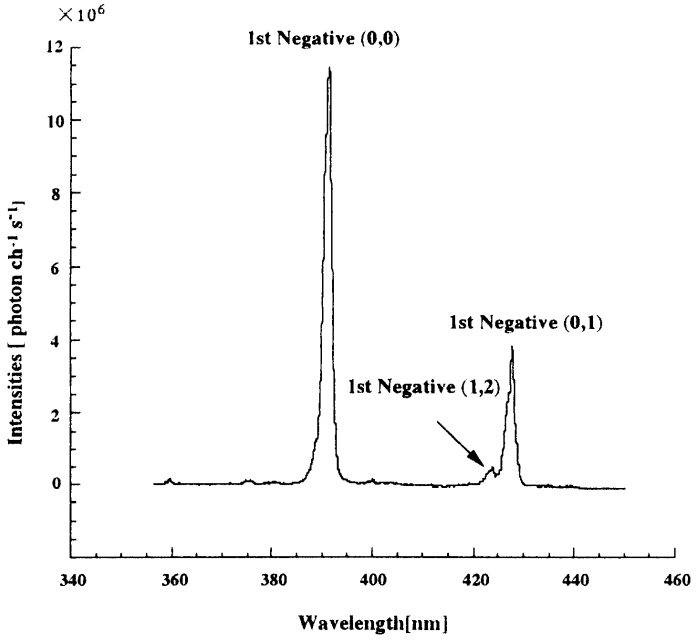

Fig. 5-6: Spectrum obtained on the rocket at 102.8 km in the whole wavelength region of the spectrometer.

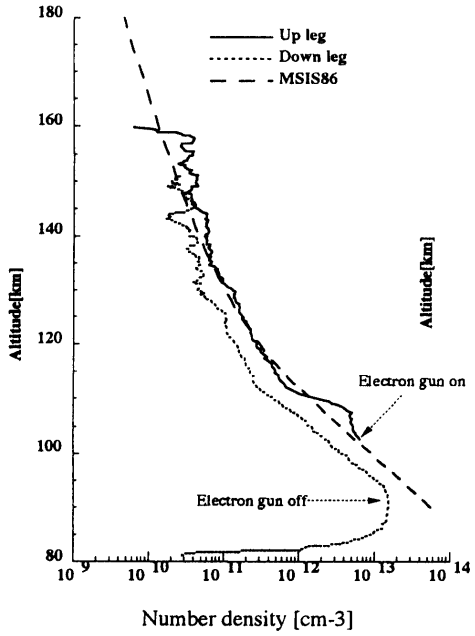

Fig. 5-7: Number density profiles on ascent and descent.

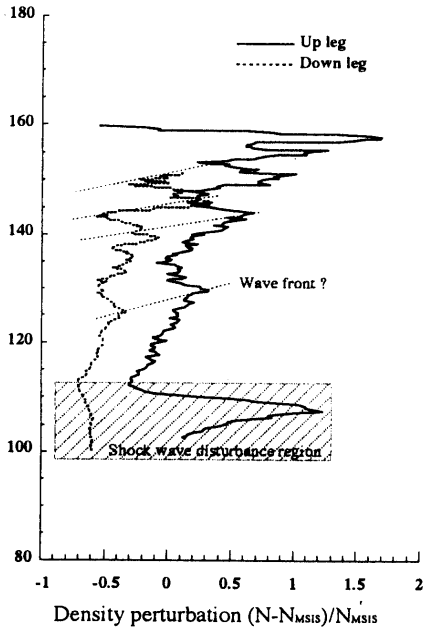

Fig. 5-8: Density perturbation defined as $(N-N_{MSIS})/N_{MSIS}$. Altitude profiles of density perturbation on ascent and descent show considerable correlation.

descent was significantly smaller than MSIS86 values. The reason was not well-understood, but it might be attributed to the aerodynamics effect because the attack angle on the rocket descent was in the range of 140 -180° (Figure 5-3) suggesting that the observation region was completely in the rocket wake region. Onei'l [1974] also reported the upleg-downleg discrepancy of intensity of 1NG(0,1) 427.8nm induced by the electron beam ionization. They had no idea about the phenomenon. As spectral intensities are also proportional to the beam current indicated in Equation (2-3), this upleg - downleg discrepancy in density measurement might be attributed to the low electron beam current on rocket descent. But the total emission current on descent shown in Figure 5-4 was almost the same as ascent values, so this probability was ruled out. Below 112km, the density perturbation was positive, because of the compression induced by the supersonic shock wave. This fact was shown for both up-leg and down-leg data in Figure 5-8. The further discussion of the aerodynamics effect will be done in the subsequent section. Figure 5-7 shows decreasing gradient in density with altitude was smaller than MSIS model. As the density of atmosphere under the hydrostatic equilibrium is proportional to the factor of exp(-z/H), where z is altitude and H is scale height defined as H= kT/mg, the small gradient of decreasing density suggests that the back ground atmospheric temperature was higher than MSIS value in this altitude region. Other important points in Figure 5-8 are the fact that the wavy structure was shown and that altitude profiles had considerable correlation between the ascent data and the descent data. The phase of upleg-downleg discrepancy in altitude is about 3km. This fact suggested the rocket passed through the atmospheric wave front slanting to the eastward or southward. The altitude intervals between wave fronts decrease with increasing altitude. This fact might reflect the saturation of the gravity wave at the critical height. This phenomenon will be further discussed in the Chapter Ⅵ.

V-3-2 Outline of Measurement of Rotational Temperature of Molecular Nitrogen

Figure 5-9(a) shows observed spectra in the wavelength region 420nm -430nm including 1NG(0,1) band and 1NG(1,2) band for three altitude levels obtained from averaging 20 spectra with an altitude resolution of 3km during up-leg. Figure 5-9(b) shows the same figure as Figure 5-9(a) but for the wavelength region 385nm -395nm including 1NG(0,0) band. The synthetic fit spectra are overplotted on the spectral data. Rotational temperature is determined to be 220K and 230K at 105±3.5km, 480K and 460K at 120±3km and 350K and 540K at 135±3km in the case of 1NG(0,1) band and 1NG(0,0) bands respectively. Intensities of spectra and consequently the signal-to-noise ratios decreases with altitude corresponding to decrease in N_2 density. Figure 5-10 shows contour map of the fitting error versus Tr and FWHM of instrumental function for a typical spectrum of (a) 1NG(0,1) band and (b) 1NG(0,0) band. The optimum rotational temperature was determined to be 230K for both cases. But the optimum FWHM was determined to be 1.15nm for (a) but the larger value of 1.5nm for (b). The valley of the error contour is nearly parallel to the x-axis. This means the ambiguity of the determined Tr due to instrumental function was small in this case. Figure 5-11 shows the altitude profiles of the rotational temperature (Tr) determined from 1NG(0,1)band and 1NG(0,0) band (a) during the rocket ascent and (b) the descent. These altitude profiles of temperature were obtained from the running average of 20 spectra with an altitude resolution of 6km. The thin line is kinetic temperature from MSIS86 model . The error of the Tr was determined previously in Chapter Ⅳ-2 to be 10K at 100km and 40K at 120km. The altitude profile of Tr on rocket ascent were similar to the MSIS values in the both case of 1NG(0,0) band and 1NG(0,1) band. Below 120km , rotational temperatures determined from these two bands well agreed on the rocket ascent . Thus measured Tr was reliable below 120km. But, above 120km, these temperatures differed each other and Tr obtained from 1NG(0,1) band showed much lower values than MSIS values at the altitude region of 130km - 145km. Tr obtained

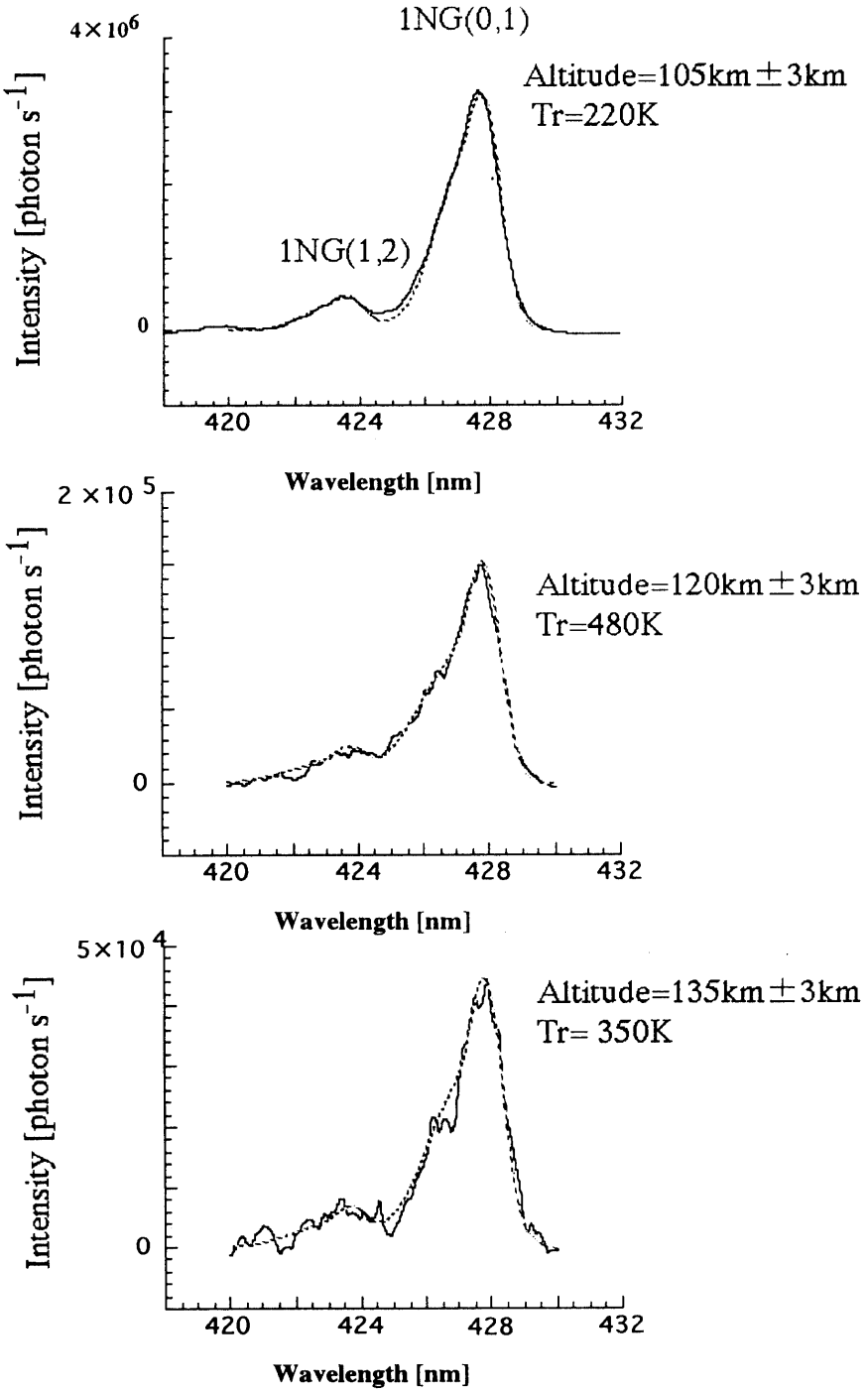

Fig. 5-9(a): Spectra in the wavelength region 420nm - 430nm at various altitudes. Solid line shows experimental data and dotted line shows synthetic fit.

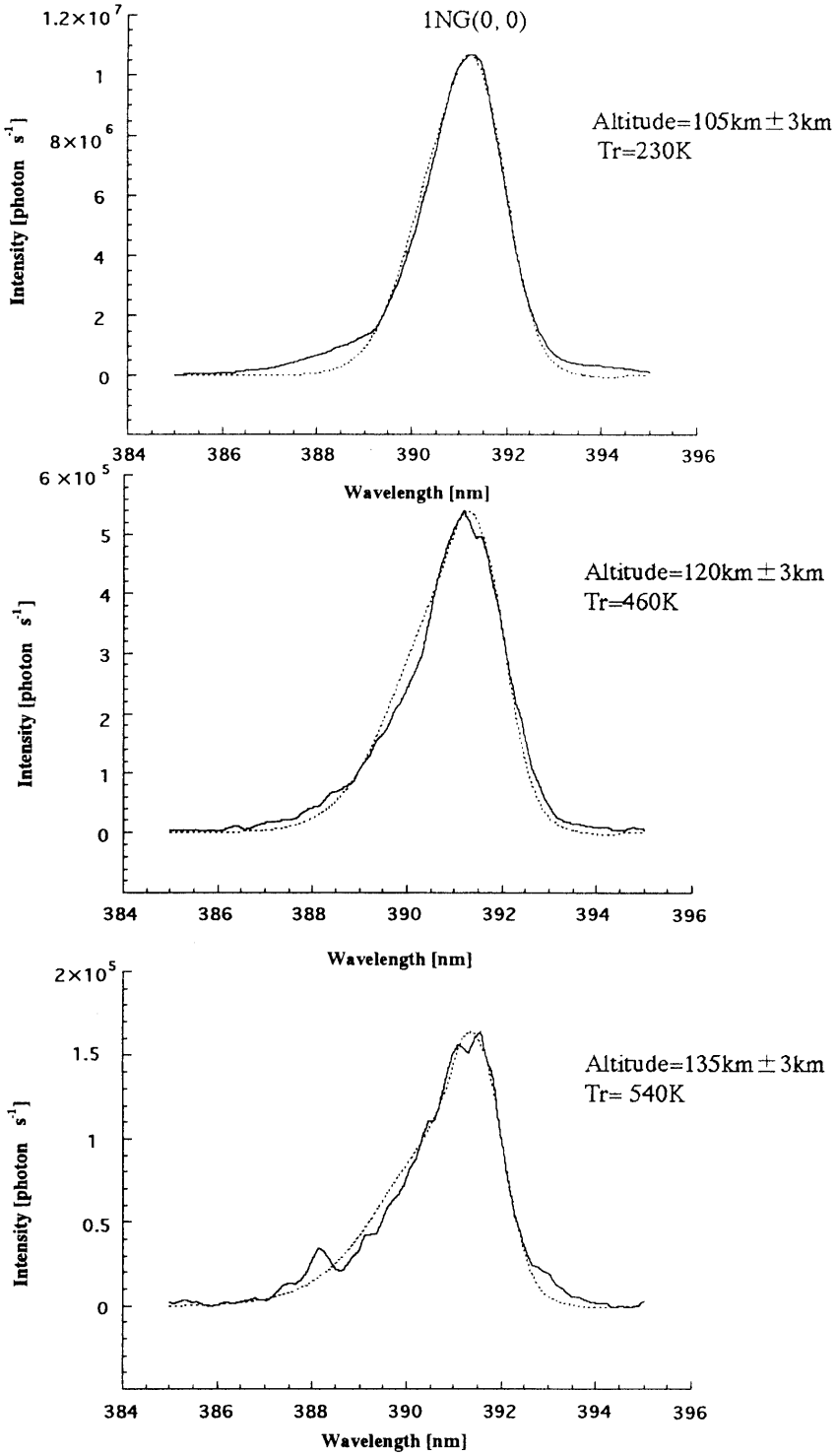

Fig. 5-9(b): Spectra in the wavelength region 385nm - 395nm at various altitudes. Solid line shows experimental data and dotted line shows synthetic fit.

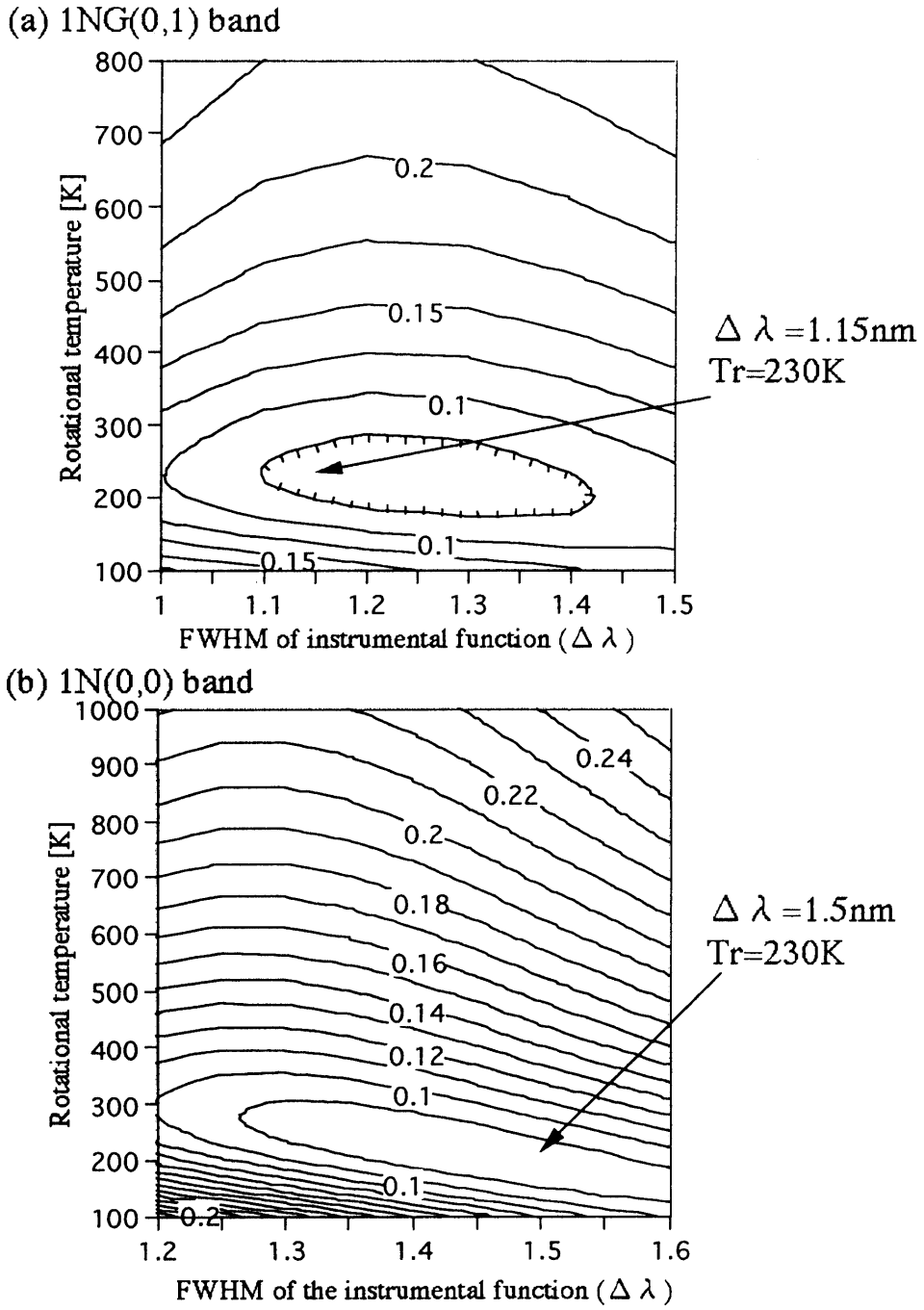

Fig. 5-10: Contour map of the fitting error versus Tr and FWHM of the instrumental function at the altitude of 105.1km.
Upper panel (a) is the fitting error for 1NG(0,1) band and lower panel (b) is the fitting error for 1NG(0,0) band. The valley of the contour is nearly horizontal for both cases (a) and (b). It means Tr is almost independent on instrument function.

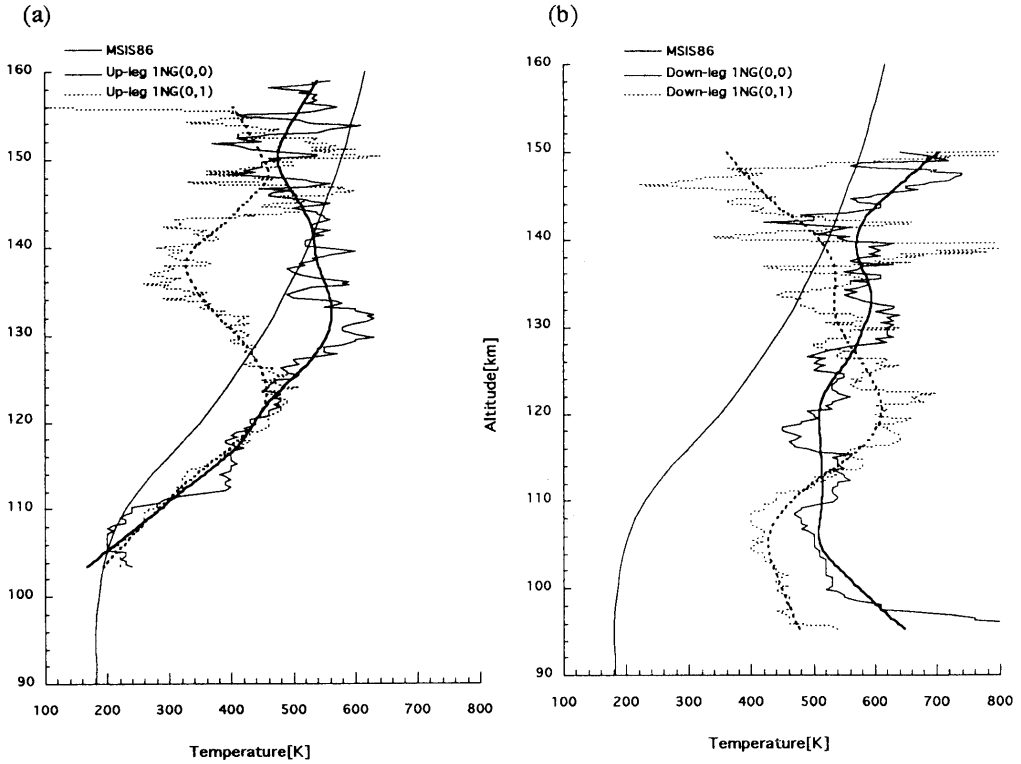

Fig. 5-11: Altitude profile of Rotational temperature (Tr).
Left panel (a) shows rocket ascent data and right panel (b) shows rocket descent data. Solid line shows temperature determined from 1NG(0,0) band and dotted line shows temperature determined from 1NG(0,1) band. Thin line shows obtained from data averaged over 20 spectra in altitude. Bold line shows smoothing the thin line.

from 1NG(0,0) band also decreased with altitudes in the altitude range of 130km - 150km, and was equal to MSIS values at 140km. This altitude was the same level as the intermediate layer was observed by the Faraday collector and the ionosphere sounder at Yamagawa. Figure 5-11(b) shows the altitude profile of Tr on the rocket descent. Tr was higher than MSIS values below 125km, and rapidly increased with decreasing altitudes below 110km in both cases of 1NG(0,1) band and 1NG(0,0) band. As the observation region was completely in the rocket down-stream region, aerodynamic heating by the shock wave disturbance began at 125km as the rocket went down and it really occurred below 110km. It was consistent with the fact that number density measurement showed large values below 110km. Figure 5-12 shows altitude profile of the fitting error for 1NG(0,0) band and 1NG(0,1) band. The fitting error of 1NG(0,1) band exceeded 0.1 above 130km while that of 1NG(0,0) band was around 0.1 in the whole altitude region. Therefore Tr from 1NG(0,0) band was more reliable than Tr from 1NG(0,1) band. Figure 5-13 shows altitude profile of the optimum FWHM of the instrumental function ($\Delta\lambda$). $\Delta\lambda$ determined from 1NG(0,1) band rapidly increased on the rocket ascent and decreased on the rocket descent with altitude above 125km, while $\Delta\lambda$ determined from 1NG(0,0) band was stable in the whole altitude region. As $\Delta\lambda$ and Tr are not completely independent and large $\Delta\lambda$ value results in small optimum Tr value as shown in the

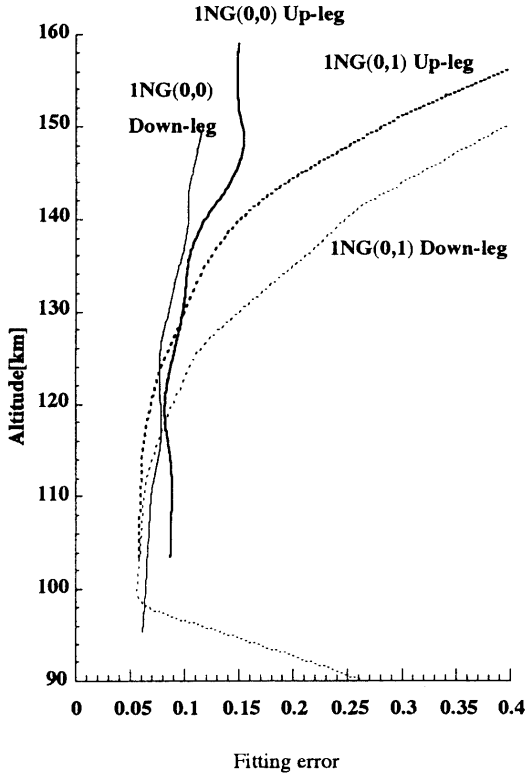

Fig. 5-12: Altitude profile of fitting error. 1NG(0,0) is more reliable than 1NG(0,1) band at higher altitude.

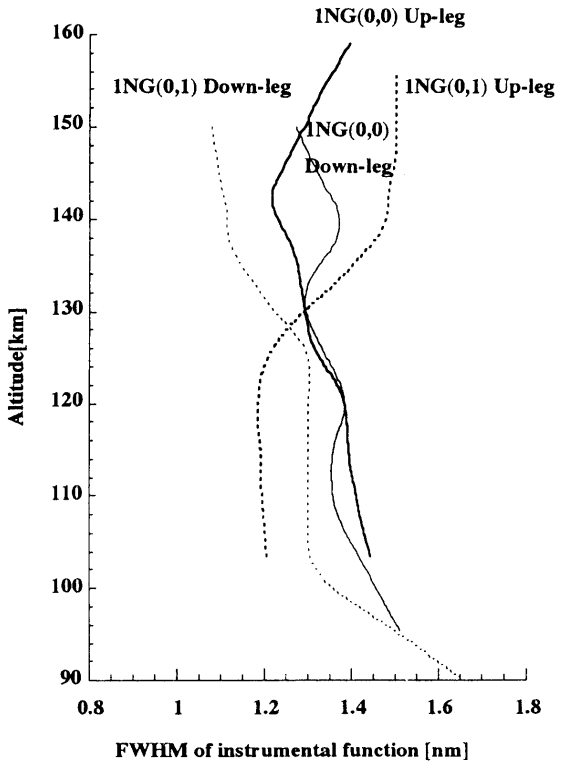

Fig. 5-13: Altitude profile of FWHM of the instrumental function. 1NG(0,0) is stable during the flight.

fitting error contour map of Figure 5-10 , unstable $\Delta\lambda$ of 1NG(0,1) band might lead the significant lower value of Tr above 130km. Therefore again, Tr determined from 1NG(0,0) band was more reliable in the light of the altitude profile of $\Delta\lambda$ above 120km. From now on, we mainly use Tr determined from 1NG(0,0) band in analysis.

The Figure 5-14 shows difference of the height varying temperature of 1NG(0,0) band from MSIS model. The sinusoidal function was fitted to data and amplitude (A[K]), wavelength (λ [km]) and null altitude (z_0) are determined as follows.

$$\Delta T_r = A\sin\left(2\pi\frac{z-z_0}{\lambda}\right) + az + b$$

$$A = 79 \pm 5 \text{ [K]}\ ,\ \lambda = 50.9 \pm 3.2 \text{ [km]},\ z_0 = 113.88 \pm 1.6 \text{ [km]}\ ,\ R = 0.886$$

Where R is correlation coefficient. This scale of wavelength is similar to that of S(2,4) mode of semidiurnal tidal wave ~53km [Forbes 1995].

V-3-3 Consistency Between the Density and Temperature Measurement

We discuss the consistency of the density measurement and temperature measurement in the light of the basic gas equation . The ideal gas for perturbation state shows

$$(P_0 + \Delta P) = k\,(N_0 + \Delta N)(T_0 + \Delta T)$$

where P_0, N_0, T_0 are pressure , number density of N_2 and temperature of the mean state atmosphere respectively and ΔP, $\Delta N, \Delta T$ are purturbations in number density and temperature of N_2,

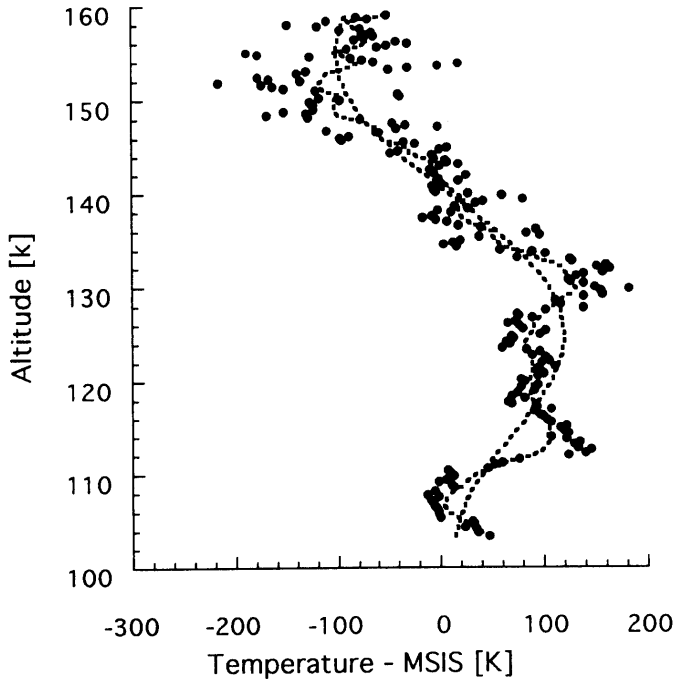

Fig. 5-14: Difference of temperature of 1NG(0,0) band and MSIS values. Sinusoidal function was fitted for the data as follows.

$$\Delta T r = A \sin\left(2\pi \frac{Z - Z_0}{\lambda}\right) + az + b$$

A=79±5[K], λ=50.9±3.2[km], Z_0=113.88±1.6[km], R=0.886
a=2.2, b=318K

respectively. k is Bltzmann's constant. Because the pressure fluctuation in the lower thermosphere are negligible in comparison with the associated density and temperature fluctuation, the ideal gas low can be used to show that [Bills and Gardner,1993]

$$\frac{\Delta N}{N_0} = -\frac{\Delta T}{T_0} \tag{5-1}$$

We defined $\Delta N = N - N_0$, $\Delta T = T - T_0$ where N and T are observed number density and temperature respectively . MSIS model values were assumed as mean state temperature and number density of N_2. Thus $N_0 = N_{MSIS}$ and $T_0 = T_{MSIS}$, where N_{MSIS} and T_{MSIS} are number density and temperature of MSIS values, respectively. Therefore it is possible to determine temperature perturbation from density perturbation and vice versa. Bill and Gardner [1993] derive temperature perturbation from number-density perturbation observed by a Na lider by using this relation. Now, we got the both number density data and temperature data by the rocket experiment , the relation of Equation (5-1) can be examined. Figure 5-15 shows the relation of Equation (5-1) using by the obtained data. Temperature determined from 1NG(0,0) was used in Figure 5-15. Figure 5-15 shows these two perturbation had

anti-correlation and satisfied the relation of Equation (5-1). Therefore temperature measurement and number density measurement were consistent. The temperature perturbation and density perturbation intersected at 138km, the same altitude as the ionization intermediate layer appeared. Figure 5-15 shows there was the large-scale perturbation with the vertical scale of 50km in the observation altitude region. It happened that semidiurnal tide existed in the observation region , and the intermediate layer was produced at the node (~138 km) of the semidiurnal tidal wind.

We also calculate in the light of the hydrostatic equilibrium equation in order to examine the consistency of the measurement.

Hydrostatic equilibrium : $$N_0 mg = -\frac{\partial P}{\partial z} \quad (5\text{-}2)$$

Ideal gas law : $$P = N_0 k T \quad (5\text{-}3)$$

Where m is molecular mass of N_2 in unit of [kg], P is pressure, g is gravitational acceleration and k is Boltzmann's constant. Combined with Equation (5-2) and (5-3),

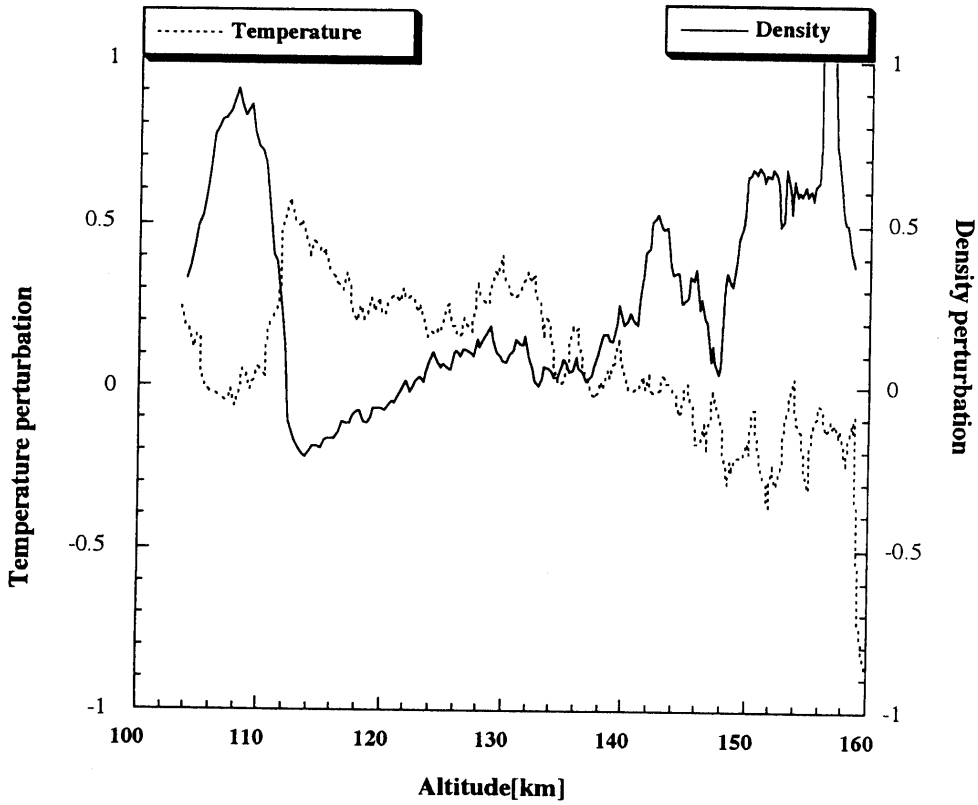

Fig. 5-15: Correlation between temperature perturbation defined as $(T-T_{MSIS})/T_{MSIS}$ and density perturbation defined as $(N-N_{MSIS})/N_{MSIS}$.
Solid line shows density perturbation and dotted line shows temperature perturbation.
Temperature data were taken from 1NG(0,0) band. Clear anti-correlation between two vriables was seen.

$$\frac{1}{N_0}\frac{\partial N_0}{\partial z} = -\left(\frac{1}{H} + \frac{1}{T}\frac{\partial T}{\partial z}\right) \tag{5-4}$$

Where H is the scale height defined as kT/mg.

Therefore we can calculate the observed altitude profile of density from that of temperature by using Equation (5-4). Figure 5-16 shows the result. The solid line shows density obtained from spectrum intensities of 1NG(0,1) band average over 10 spectra. The dotted line shows density calculated from Equation (5-4), in which the temperature data obtained from 1NG(0,0) band average over 20 spectra was used for the calculation. The slope of the observed altitude profile of the density was smaller than MSIS model. The density calculated from hydrostatic equilibrium equation also shows small slope corresponding to the high rotational temperature as shown in Figure 5-11(a) below 140km.

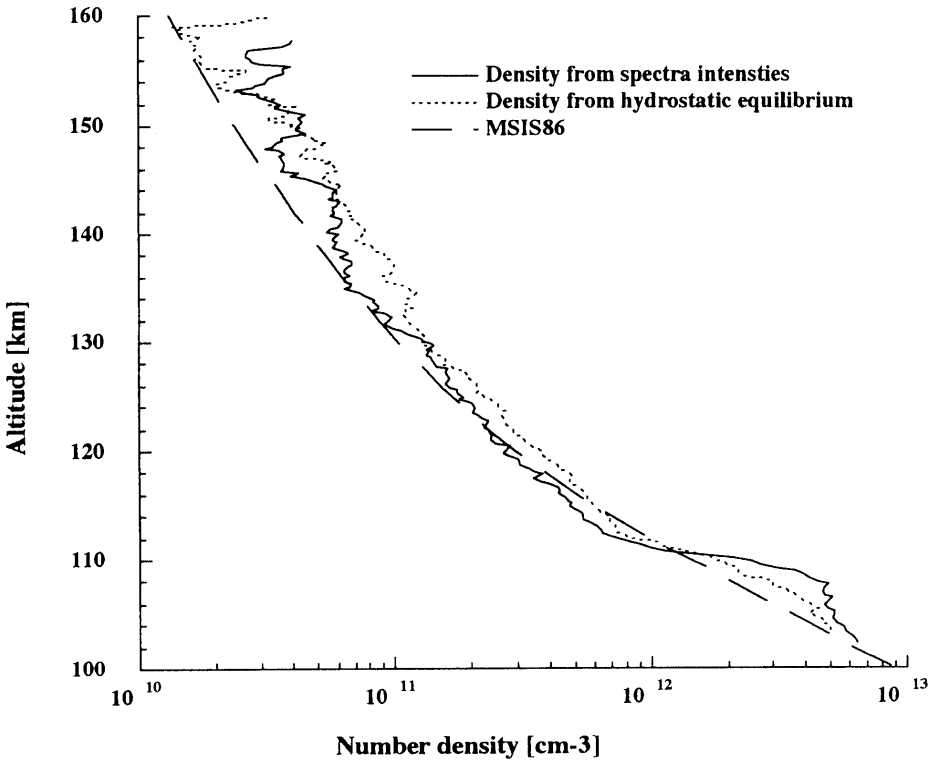

Fig. 5-16: Altitude profile of number density on rocket ascent.
Solid line is density obtained from spectra intensities. Dotted line is calculated from temperature altitude of 1NG(0,0) band.

V-3-4 Disturbance by the Shock Wave

Determination of number density and rotational temperature of N_2 should be done with great care to avoid shock wave disturbance as mentioned in Chapter Ⅳ-3. The shock wave disturbance is highly dependent on the rocket attitude , such as the attack angle and the spin phase angle as defined in Figure 4-24. We discussed the outline of the temperature and density measurement so far with altitude resolution of 3km - 7km, but we should discuss the obtained data with higher time resolution at the cost of accuracy because the spin phase angle was changing cyclically over a period of 1s. Figure 5-17 shows spin phase angle (ϕ) dependence of number density perturbation ($\Delta N/N_0$) in the altitude range of 100.59km - 107.52km on rocket ascent. The spin phase angle were determined by using the magnetic filed sensor (GAH) , which was set up perpendicular to the rocket axis. The exposure time of a image sensor for one spectrum image was 240ms, thus about 4 data were obtained during 1 spin. The shock wave front generally extends toward the down stream region with respect to the rocket body as discussed in Chapter Ⅳ-3, and hence the observation point is most severely

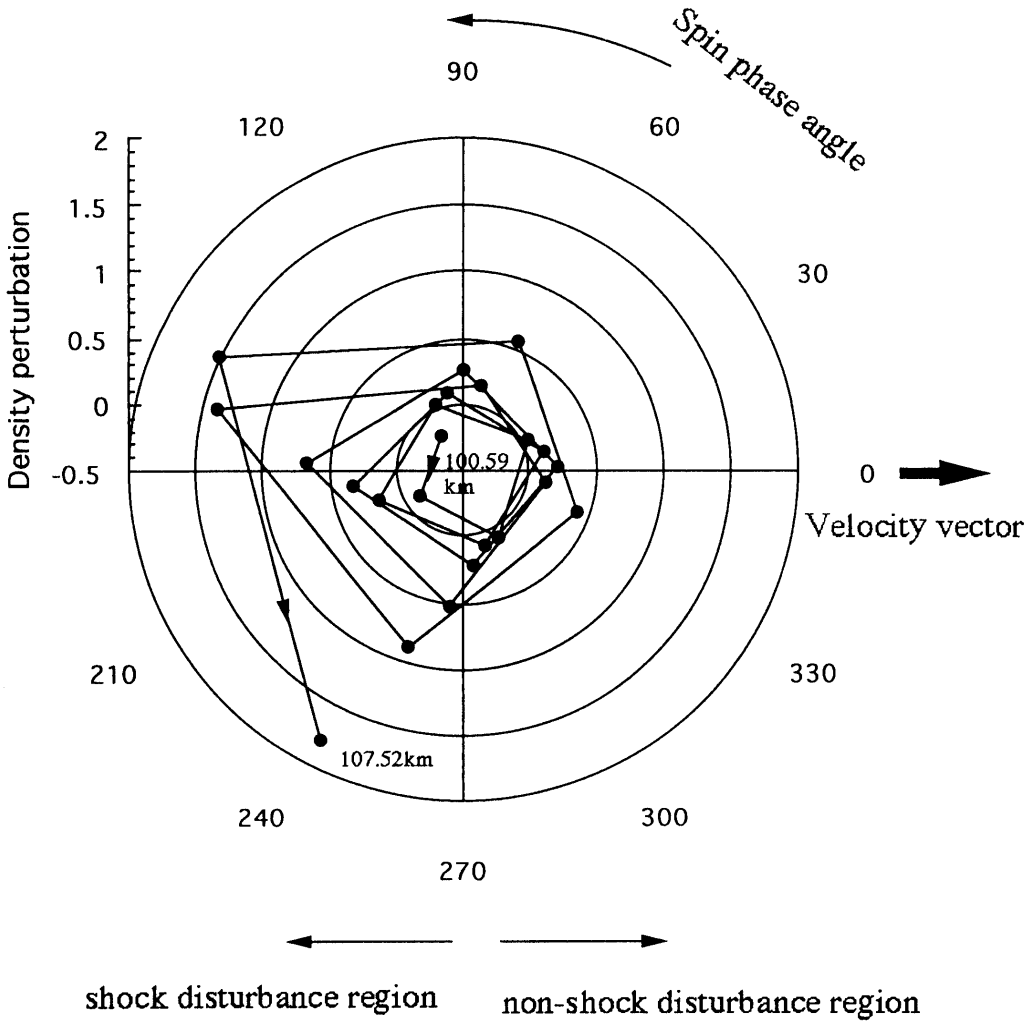

Fig. 5-17: Spin phase dependence of number density in the altitude range of 100.59 - 107.52km.
The number density shows large values in the down stream region.

affected by the shock wave disturbance when the spin phase angle is near 180°. Figure 5-17 shows the spin dependence of the number density perturbation deterimined from the peak intensity of 1NG(0,1) band without summing the spectra. The density perturbation was large in the down stream region ($90° < \phi < 270°$) but small or nearly equal to zero in the up-stream region. The density perturbation increased with increasing altitude. Figure 5-18 shows altitude profile of the number density obtained from 1 spectrum. Below 110km, densities changed periodically with altitude. It suggests that the measurement was affected by the shock wave disturbance. Figure 5-19 shows the same profile as Figure 5-18 but divided into the upstream region (solid line) and the downstream region (dotted line). Below 110km, number densities in the downstream region was always larger than those in the upstream region but there was no spin dependence at higher altitude. Above 120km the disturbed region becomes more diffuse and collisionless flow conditions have been reached at about 120km altitude. In such a free molecular flow, molecules which have bounced on surface of the instrument can reach the point of observation and therefore constitute disturbance. Therefore number density is lower in the rocket down stream region or so-called *wake region* [Bird, 1988]. This effect was not so important on the rocket ascent because of the small attack angle in the range of 10° - 30°, thus the observation point was little shaded by the rocket body. But this effect was more significant on the rocket descent when the attack angle in the range of 140° - 170°.

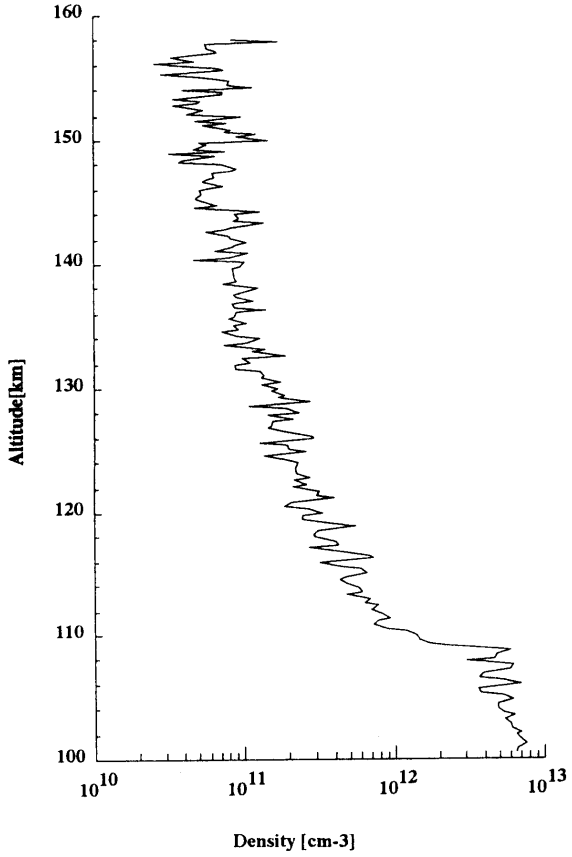

Fig. 5-18: Altitude profile of number density on rocket ascent.
Below 110km, densities changed periodically with altitudes. It suggests that the measurement was affected by shock disturbance.

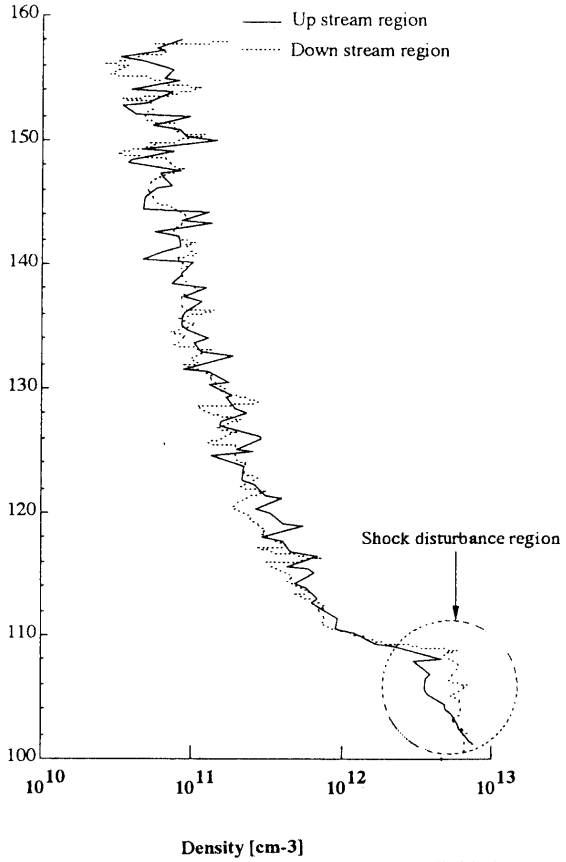

Fig. 5-19: The same figure as Fig. 5-18, but divided into up-stream region data (solid line) and down-stream region data (dotted line). Below 110km, the dotted line always larger than the solid line, while, there was no difference above 110km.

We also examined the shock disturbance effect to rotational temperature measurement. Below 110km, the signal-to-noise ratio of the spectra were large enough to determine the rotational temperature from only 1 spectrum without summing 10 or 20 spectra in altitude. Figure 5-20 shows the same figure as Figure 5-17 but for the rotational temperature. Figure 5-20 shows Tr was not so dependent on the spin phase as the number density. It was due to the fact that rotational - translational energy exchange process is not so fast as translational - translational energy exchange process. Thus Tr was relatively indifferent to the shock wave disturbance. But in detail, Tr enhancement was shown at the spin phase of 0°, 120° and 230°. The reason was not understood, but the configuration relation of the Faraday collector and the observation region perhaps had something with the Tr enhancement at these spin angles. Figure 5-21 shows relation of density and temperature at the altitude region of 100 - 110km. The density shows anti-correlation with temperature. This means Equation (5-1) also can explain the disturbance by the shock wave. If Rankine-Hugoniot theorem is valid, temperature and number density had positive correlation. Because adiabatically compression results in increase of the inertial energy. Thus the disturbance in the rarefied gas perhaps does not obey the simple shock wave theory which is valid in the dense flows.

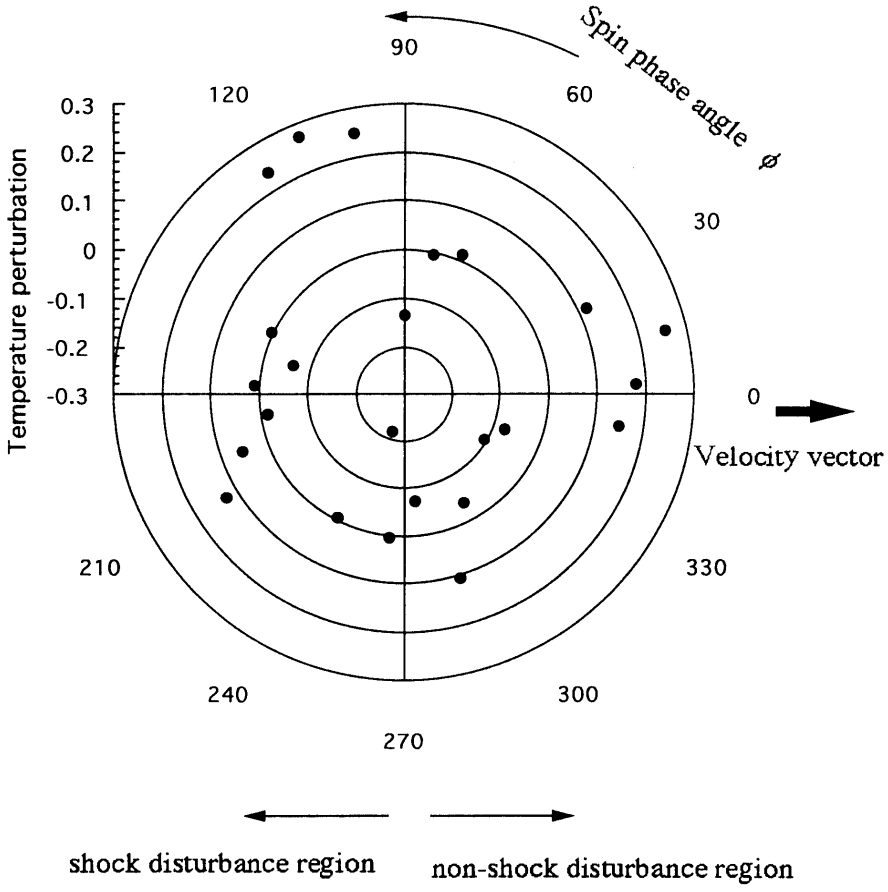

Fig. 5-20: Spin phase dependence of rotational temperature in the altitude range of 100.59 - 107.83km.

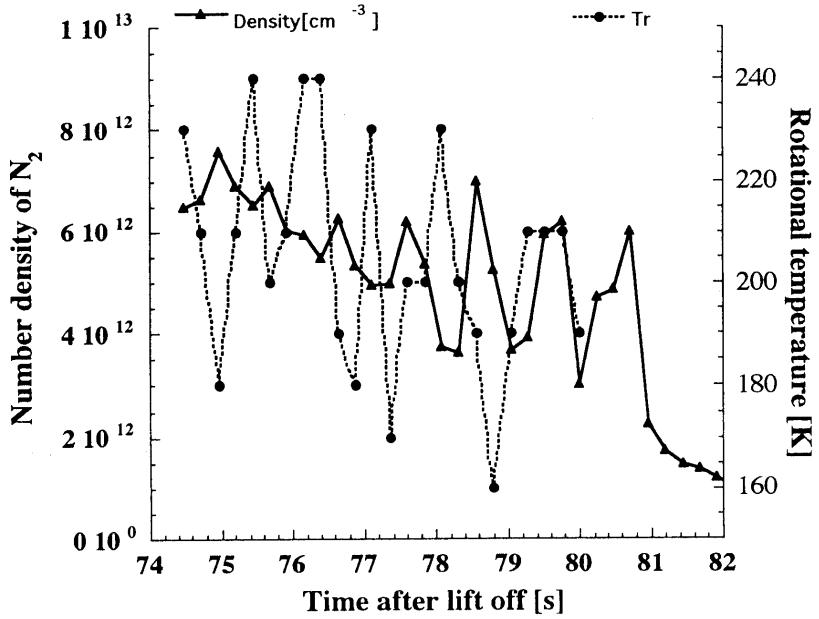

Fig. 5-21: Correlation between temperature and density in the altitude region of 100.59 - 109.76km. Solid line shows density and dotted line shows temperature. Temperature data was taken from 1NG(0,0) band. Clear anti-correlation between tow variables was seen.

V-4 Vibrational Temperature Measurement

Determination of Tv should be done with great care to avoid excitation of the N_2 gas target by secondary electrons as mentioned in chapter Ⅲ. Figure 4-19 suggests N_2 second positive (2PG) band intensities appear relatively large for the pressure range 8.0×10^{-4} Torr $\sim 1.0 \times 10^{-4}$ Torr corresponding altitude of 95km $\sim$ 105km. As 2PG bands have a large emission cross section for low energy electrons (Figure 3-6), appearance of relatively strong 2PG bands suggests that the target gas might be excited by low energy electrons. Under the situation, vibrational temperature estimated to be higher than the real value because of the break down of Franck - Condon theorem. This process was also observed on the rocket experiment. Figure 5-22 shows the spectra in the whole wavelength region of the spectrometer at about 100km on ascent. The spectra of 1NG bands were only observed in the upper panel (a), while 2PG bands were also clearly observed in the lower panel (b). Figure 5-23 shows the ratio of the intensities of 2PG (0,2)/1NG(0,1)) in the altitude range of 100km$\sim$110km on ascent. In these altitudes, 2PG bands were most prominently observed during the rocket experiment. As the number density of N_2 in the observation region had spin modulation, the 2PG/1NG ratio which is dependent on gas pressure was also modulated. Vibrational temperature derived from 1 spectrum by using the least square fitting method is also plotted in Figure 5-23. Figure 5-23 shows good correlation between 2PG/1NG ratio and vibrational temperature. When 2PG/1NG ratio is high , Tv was also determined to be high around 1000K. Real values were estimated to be under 500K for the case of low 2PG/1NG ratio in Figure 5-23 in these altitude range.

Next, the error of determined Tv is considered. As Tv is determined by the ratio 1NG(0,1)/1NG(1,2), the error of Tv is attributed to the error of the ratio. If the noise of the spectra is not so large, the error of the ratio is described as follows.

$$\frac{I_{01}}{I_{12}} \pm \Delta\frac{I_{01}}{I_{12}} = \frac{(I_{01} \pm \Delta I_{01})}{(I_{12} \pm \Delta I_{12})} = \frac{I_{01}\left(1 \pm \dfrac{\Delta I_{01}}{I_{01}}\right)}{I_{12}\left(1 \pm \dfrac{\Delta I_{12}}{I_{12}}\right)} \cong \frac{I_{01}}{I_{12}}\left(1 \pm \frac{\Delta I_{01}}{I_{01}}\right)\left(1 \mp \frac{\Delta I_{12}}{I_{12}}\right)$$

$$\cong \frac{I_{01}}{I_{12}}\left(1 \pm \frac{\Delta I_{01}}{I_{01}} \mp \frac{\Delta I_{12}}{I_{12}}\right) \cong \frac{I_{01}}{I_{12}}\left(1 \pm \frac{\Delta S}{S}\right)$$

Where I_{01} and I_{12} are peak intensities of the 1NG(0,1) band and 1NG(1,2) band respectively, and ΔI_{01} and ΔI_{12} are noise of the 1NG(0,1) band and 1NG(1,2) band respectively. S is the area enclosed with the synthetic spectrum profile and ΔS is the difference area between the synthetic spectrum profile and the observed spectrum profile.

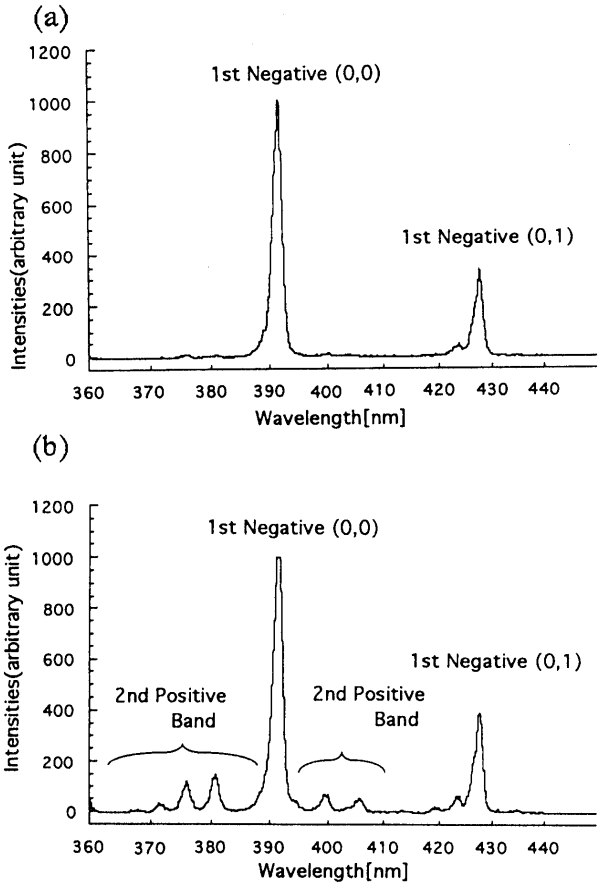

Fig. 5-22: Spectrum obtained in the altitude range of 100 - 110km.
Upper panel (a) shows spectrum produced by pure primary beam electrons.
Lower panel (b) shows spectra produced by secondary electrons besides by primary beam electrons.
2nd Positive band notably appeared in panel (b) corresponding to the existence of low energy electrons.

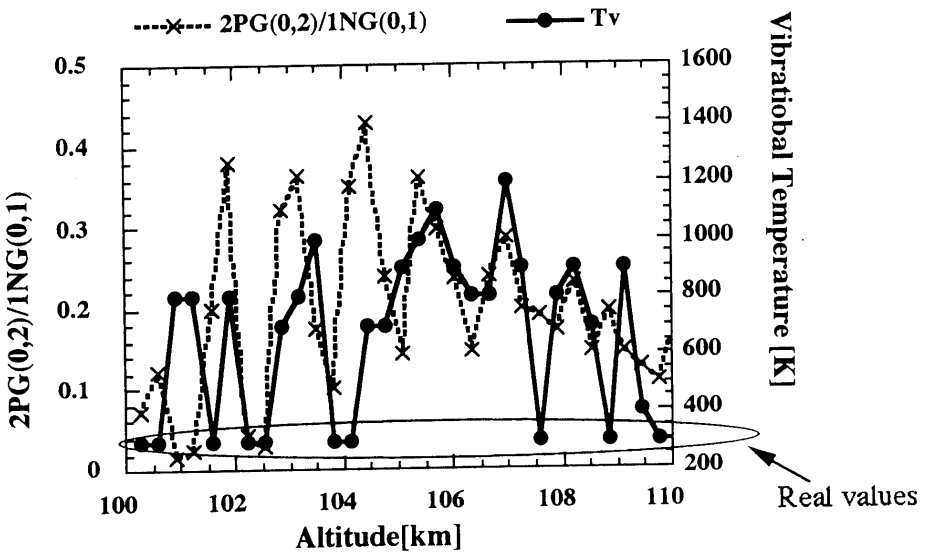

Fig. 5-23: Correlation between vibrational temperature and ratio of 2PG(0,2)/1NG(0,1) in the altitude region of 100. - 110km.
When 2PG(0,2) band appeared, vibrational temperature determined to be higher than real value. As 2nd positive band intensities are much dependent on the gas pressure in this altitude shown in Fig. 4-19, subsequently dependent on shock wave disturbance, their intensities were also modulated by the spin rotation of the rocket body.

As mentioned in Chapter Ⅱ-2, the fitting error is nearly equal to the ratio $\Delta S/S$. Therefore,

$$\Delta\left(\frac{I_{01}}{I_{12}}\right) = \frac{I_{01}}{I_{12}} \times \text{fitting error}$$

The error of Tv can be estimated by means of the fitting error. The ratio I_{01}/I_{12} is almost invariant below 600K. Thus if Tv is determined to be below 600K, the lower limit of Tv is nearly equal to 0 K. The upper limit of Tv mainly depends on the fitting error. The result is shown in Figure 5-24. Above 110km Tv was determined from running average over 20 spectra for the reason that 2PG bands were not observed any more and that signal-to-noise ratio was too low to determine from only one spectrum. There was region where Tv ($\sim$800K) is moderately high with small error bars at 110 - 120km. As 2PG bands were not observed in this altitude region, the excitation by the low energy electrons did not occur. There is no idea whether this moderately high Tv is attributed to the measurement error or not. At higher altitudes ($>$125km) , the small signal-to-noise ratio, as evidenced by the fact that determined Tv were scattered with large error bar, does not permit any conclusion. But the upper limit of Tv was determined to be 1000$\sim$1600K at 125-150km. Figure 5-25 shows the result of Tv measurements along with the summary of previous theoretical values. The spectra which are affected by the low energy electrons are omitted in the altitude region of 100 - 110km in producing Figure 5-25. The bold shaded line is the smoothing curve of the present results. The present results are consistent with other calculations done in 80's and 90's which include all possible process of excitation and quenching of vibrationally excited N_2, and are also consistent with O'neil [1974] 's upperlimit.

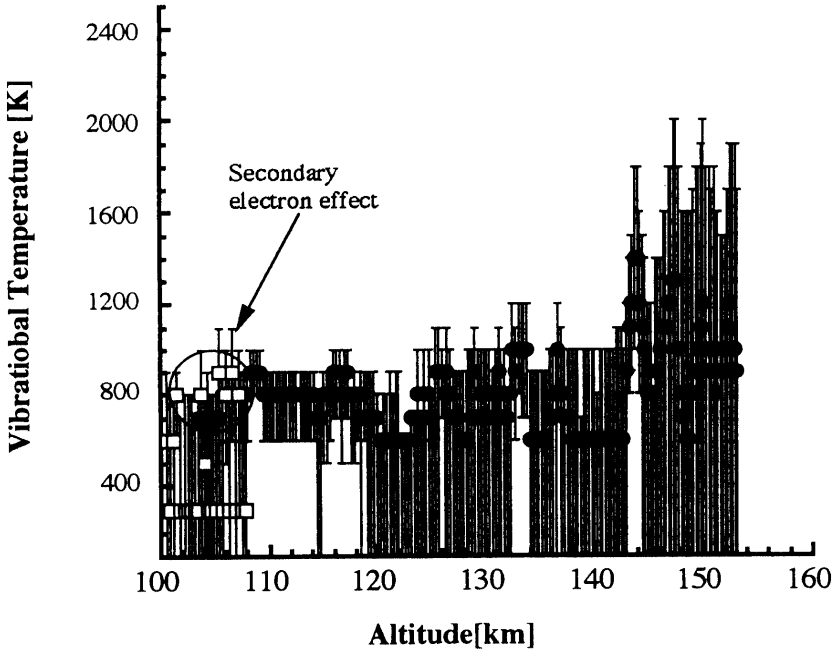

Fig. 5-24: Altitude profile of the vibrational temperature with error bars Rectangular points (□) are determined from 1 spectrum and circle points (●) are determined from 20 averaging spectrum. Below 110km, removed the data which determined from spectra affected by secondary electrons, Tv was estimated to be lower than 800K. At higher altitude, SN ratio of spectra became so small that determined Tv were scattered with a large error bar.

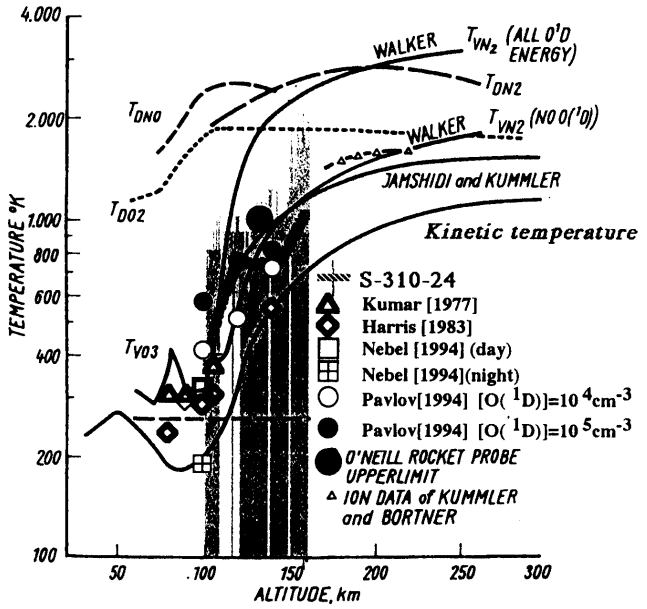

Fig. 5-25: Summary of vibrational temperatures including our results (bold shaded line with the gray error bars). Our results was not inconsistent with any calculation in 80's and 90's.

VI DISCUSSION

VI-1 Temperature Fluctuation Induced by the Vertical Wind

We observed anomalously large temperature fluctuation. These kind of fluctuation may be caused by the vertical wind. Hernandez [1982] obtained high time-resolution measurements at mid-latitude which revealed an oscillatory behavior with an amplitude 20ms^{-1}. This was attributed to passage of the gravity wave through the observed region. Wardrill and Jacka [1986] measured temperature and vertical wind simultaneously by measuring O I [λ =630nm] emission in the night airglow with a Fabry-Perot spectrometer at high-latitude. They described that downward winds with the amplitude of 50m/s produce temperature enhancements of 200K. Figure 6-1 shows their result. The temperature data show temperature enhancement from 1820 to 1930UT and around 2200UT, which were periods of sustained downward wind .

In the lower thermosphere region, the results of ion temperature observation by the incoherent scatter radar show dominant semidiuranl modes as shown in Figure 6-2. Harper [1981] reports large temperature amplitude of 50-100K by semi-diurnal tidal wave. Figure 6-3 shows measured ion temperatures at Arecibo on 3 October 1970 for the altitude 103 to 130km [Wand, 1976]. The temperature is almost constant at the lowest altitudes, but at higher altitudes the temperature fluctuations are evident whose amplitude reaches 100K. Forbes [1982] developed tidal wind model including model parameterizations of background winds, temperature, composition, hydromagnetic

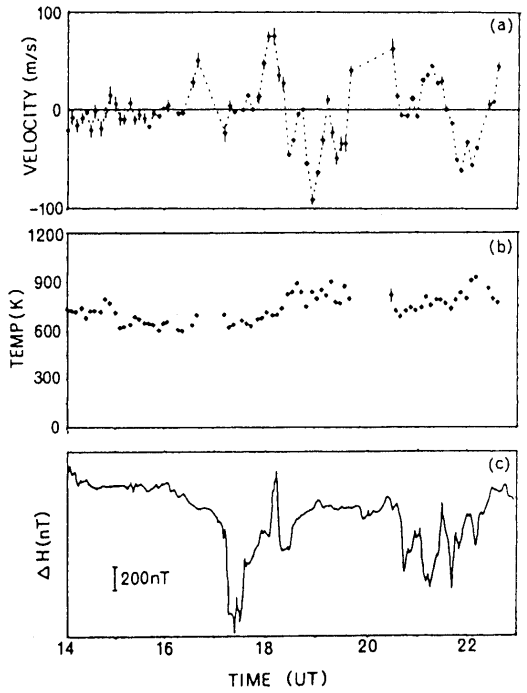

Fig. 6-1: Thermospheric vertical wind velocity (a), temperature (b) and deviation of horizontal component of the local magnetogram (c) for 24 May 1983. Velocity and temperature were determined from OI emission[λ =630nm] at approximate altitude of 250km. [Wardill, 1986]

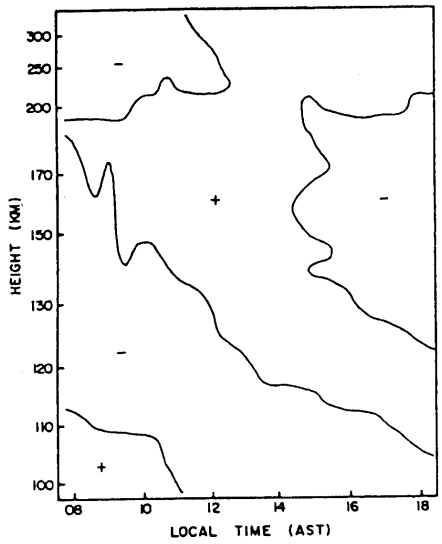

Fig. 6-2: Contour plot of region of positive and negative deviation from the daytime mean ion temperature at each height above Arecibo. Systematic deviation from mean temperature of ±50-100K are inferred. [Harper, 1981].

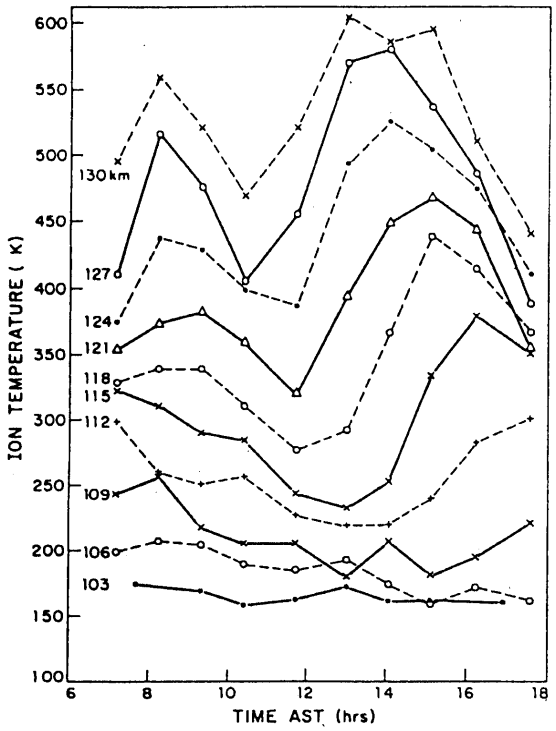

Fig. 6-3: Measured ion temperatures at Arecibo on 3 October 1970 for the altitude range 103 to 130km [Wand, 1976].

coupling , Newtonian cooling, eddy and molecular diffusion, and tidal forcing mechanism. Figure 6-4 (a)-(d) shows the calculation of the altitude profile of amplitude and phase of (a) northerly wind , (b) westerly wind (c) vertical wind and (d) temperature respectively for the solar semidiurnal tide at various altitude. The phase means the hour of maximum of the oscillation. The panel (d) shows temperature amplitude is about 10K at 100km but it reaches 60K at 120km at equator. The vertical wind reaches 1m/s above 120km.

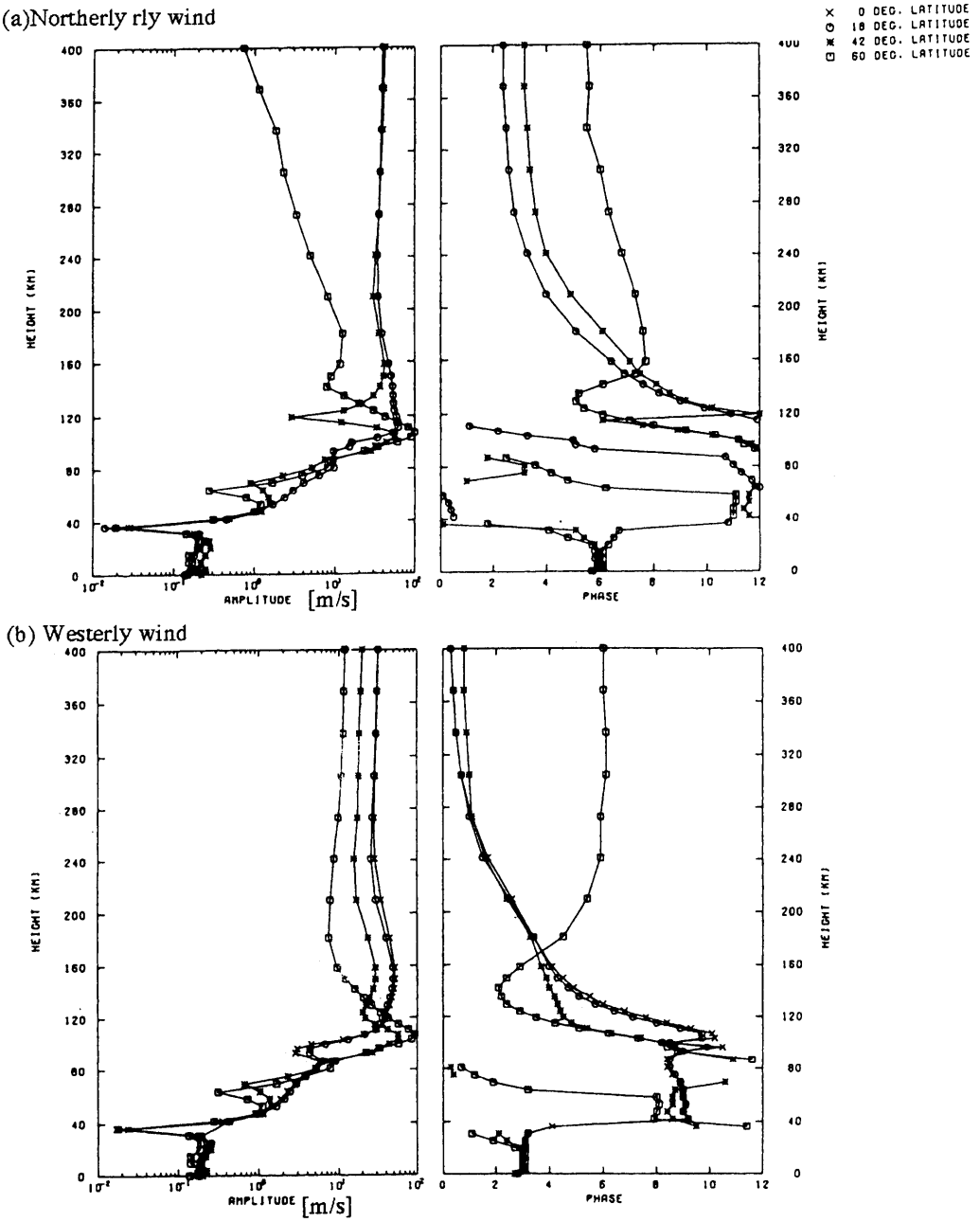

Fig. 6-4: Amplitude and phase for the semidiurnal tide at various altitude
(a) amplitude (left) and phase (right) vertical structures of northerly wind.
(b) same as (a) but for westerly wind [Forbes, 1982].

(c) Vertical wind

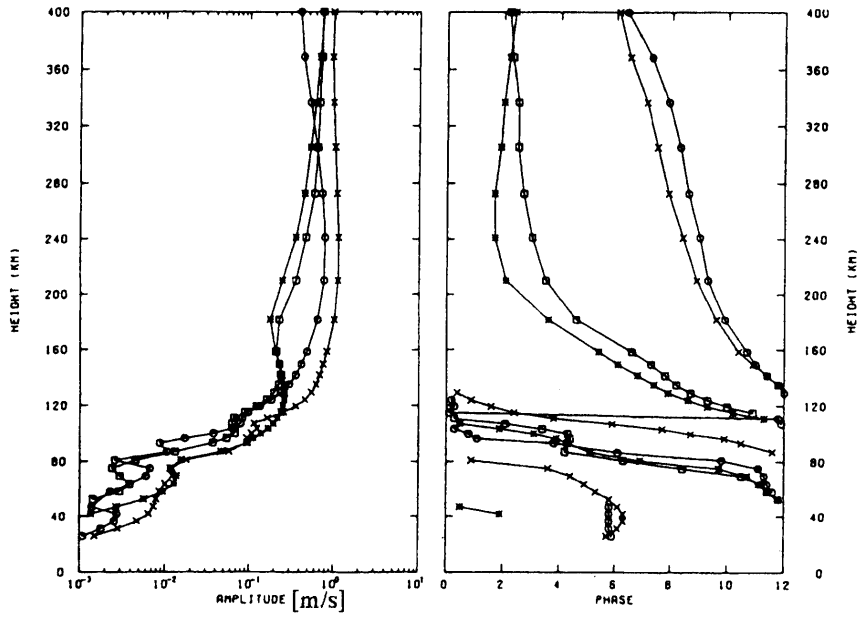

(d) Temperature

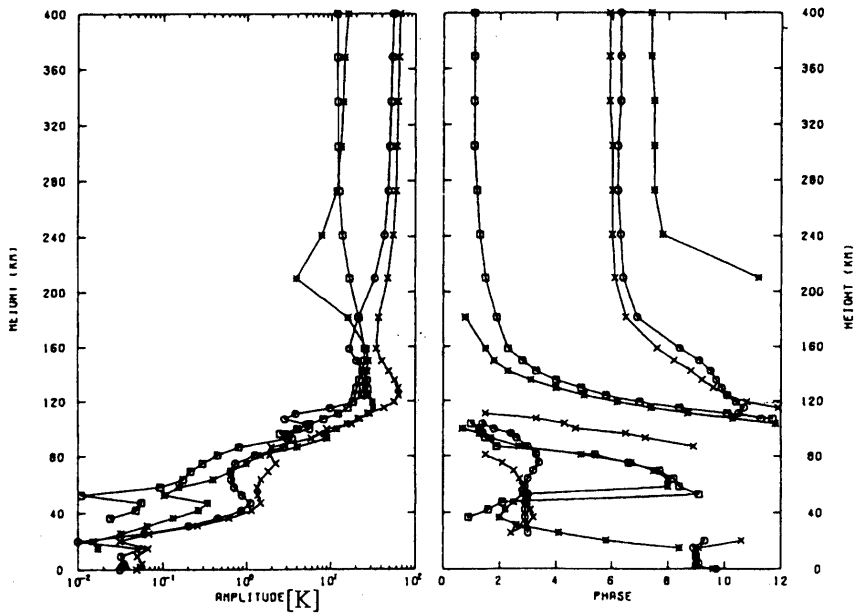

Fig. 6-4: Amplitude and phase for the semidiurnal tide at various altitude (continued from previous page).
(c) same as Fig. 6-4 (a) but for vertical wind, and
(d) same as Fig. 6-4 (a) but for temperature.

In the altitude range between 90 and 120km, the semidiurnal (2,4) mode is dominant whose vertical wavelength is 53.8km for an isothermal atmosphere at 256K [Forbes 1995]. We estimate the temperature fluctuation induced by the vertical wind.

The conservation of potential temperature is [Andrews Holton and Leovy 1987] ,

$$\frac{D\theta}{Dt} = 0 \qquad \left[\theta \equiv T\exp\left(\frac{R\,z}{C_pH}\right)\right] \tag{6-1}$$

where z is altitude, R is gas constant, C_p is specific heat at constant pressure. D/Dt is the time rate of change following the fluid motion in the stratified atmosphere (Horizontal derivative term is neglected) ,

$$\frac{D}{Dt} \equiv \frac{\partial}{\partial t} + V_z\frac{\partial}{\partial z} \tag{6-2}$$

Equation (6-1) is written using the temperature T instead of potential temperature θ [Rishbeth 1969],

$$\frac{\partial T}{\partial t} = -V_z\left(\frac{g}{C_p} + \frac{\partial T}{\partial z}\right) \tag{6-3}$$

The first term of the right member describes adiabatic heating (cooling) induced by downward (upward) wind, and the second term describes advective term.

Introducing the buoyancy frequency N defined as

$$N^2 = g\frac{\partial \ln\theta}{\partial z} \tag{6-4}$$

Equation (6-3) results in

$$\frac{\partial T}{\partial t} = -\frac{T}{g}N^2V_z \tag{6-5}$$

Assuming the vertical wind to be a sinusoidal function,

$$V_z = \hat{V}_z\exp(-i\omega + k_x x + k_y y + k_z z) \tag{6-6}$$

The temperature fluctuation is derived,

$$\frac{\Delta T}{T} = \frac{N^2}{g}\int V_z dt \approx -i\frac{2N^2V_z}{g\omega} \tag{6-7}$$

Substituting the typical value for the buoyancy frequency of N=2×10^{-2} [s^{-1}], frequency of the internal gravity wave of about ω=1.7×10^{-3} [s^{-1}] (period is 1 hour) and vertical wind velocity of 5m/s

$$\frac{\Delta T}{T} \approx 0.23 \tag{6-8}$$

Therefore observed temperature fluctuation of 70 - 80K may occur if there was atmospheric wave which had a strong vertical wind field or a long period. Figure 6-5 shows the numerical solution of time evolution Equation (6-3). The initial condition is given by the kinetic temperature altitude profile of MSIS86 after subtracting the base line of az+b described in Figure 5-14 for the present calculation. The temperature of MSIS model is quite reliable as a mean state of the atmosphere in the lower thermosphere. Kirwood [1996] determined mean seasonal temperature in the altitude region of 90 -120 km by the European Incoherent Scatter (EISCAT) radar and showed quite good agreement with the MSIS90E model. Therefore we can take the MSIS value as a mean or initial condition without no perturbation induce by the wind -field. The vertical wavelength is assumed to be 50km according to the result of the temperature measurement as shown in Figure 5-14. The vertical wind field of 5m/s is applied to Equation (6-4) for 15 minutes. The integral of amplitude of the vertical

wind over applied time is important and we can derive the same result if the amplitude is 1m/s and applied time is 75 minutes. The declination of the temperature between 120km and 150km is the similar value of the adiabatic lapse rate of Γ_d =g/ C_p=9.76K/km. If the declination of the temperature is larger than Γ_d, the convective instability is induced and the declination will be kept to be Γ_d . Therefore temperature fluctuation may not be so large when the radiative dumping or the turbulence induced by convection instability are included [Hodges,1967; Akmaev, 1996] .

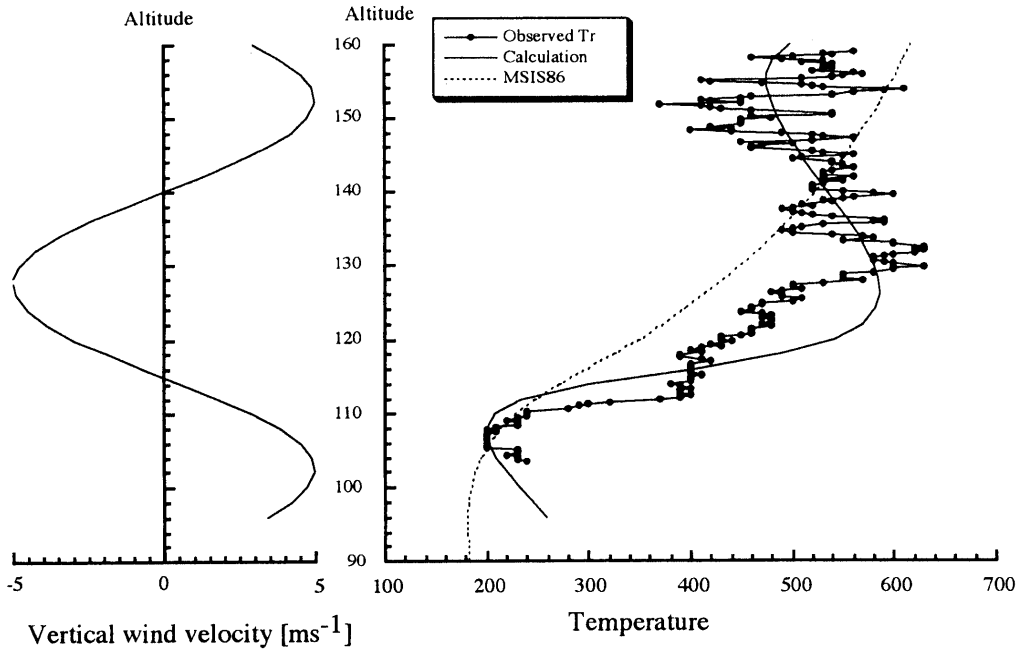

Fig. 6-5: Temperature fluctuation induced by the vertical wind.
Left panel shows vertical wind field with amplitude of 5m/s and vertical wavelength of 50km. Right panel shows comparison of Tr determined from 1NG(0,0) band on rocket ascent (line with points) with calculated values for the vertical wind field applied for 15 minutes (solid line). Dotted line is the MSIS value and this value is assumed to be initial condition for calculation. Down ward wind heats (cools) the atmosphere by adiabatic compression (expansion).

VI-2 The Intermediate Layer

The ionization intermediate layer was observed during rocket flight. This section is devoted to interpreting the intermediate layer from a point of view of Internal Gravity Wave (IGW) or Semi-diurnal tidal wave (ST) .

VI-2-1 Introduction of the Ionization Descending Intermediate Layer

At midlatitudes the bottomside F region and E region ionosphere decays rapidly at night by dissociative recombination and may reach an equilibrium number density between 10^2 - 10^3 cm^{-3}. Intermediate layer of ionization can appear as enhancements in the total ion concentration. The layers is considered to be the result of the vertical ion convergence induced by meridional wind shear of semi-diurnal tidal wind [Fujitaka and Tohmatsu, 1973]. The recent work of Osterman, Heelis and Bailey [1994] and Osterman and Heelis [1995] showed neutral wind effect for various wavelengths to the formation of the layers by using the one dimensional ion continuity equation. Related work has been continuing in the radar studies of Mathews et al. [1993] who have shown that the layers are a regular and persistent feature of the lower ionosphere above Arecibo. Their study also provided evidence of a coupled neutral and ion-layer mechanism that can deposit lower-ionospheric metallics into the upper mesosphere as a result of descending layers and the associated wind-shear nodes which converge and transport the ions [Kane et al., 1993]. With regard to intermediate and descending layers, Miller et al. [1993] have analyzed low perigee passes (140-200 km) of the Atmospheric Explorer E ion mass spectrometer data. They found ion composition waves, intermediate layers of enhanced ionization, and ionization depletions similar to equatorial ionization bubbles. NO and O dominated the enhanced ionization layers without significant metallic ions. This suggests that metallic ions are not required to produce the intermediate layers at altitudes above 140 km. But Osterman and Heelis [1995] shows metallic ions, if present in the valley region, will be transported into any layer formed and cause the enhancements to assume altitude profiles that are significantly different from those expected when layers are populated solely by molecular ions.

VI-2-2 Observation

The altitude of the intermediate layers including the present data compared with the altitude of the ion convergent or divergent node are shown in Figure 6-6 modified from Fujitaka [1973]. The altitudes of the present data were determined from the ionogram obtained at Yamagawa (31.2° N, 130.6° E) on 11 February 1997 at intervals of 15 minutes as shown in the 1st column in Figure 6-8. The layer appeared at 153km altitude at 19:45, descended at a rate of 6.9m/s, and disappeared at 120km altitude at 21:00. This descending layer was observed only above Yamagawa and not observed above other ionosonde stations in Japan. Thus this layer was local phenomenon above Kagoshima. Figure 6-7 shows calculated iso-velocity contour map of meridional wind of semidiurnal tidal mode S(2,4) compared with the observation by HARDI flown abroad the Upper Atmosphere Research Satellite (UARS). The data obtained by HARDI was limited at daytime above 110km, but the meridional wind shear node is seen in local evening in the altitude range of 100 - 130km. As the northward (southward) wind induces the downward (upward) ion drift , the ions converge at the node where the wind changes its direction from northward to southward with decreasing altitude. Thus the midnight wind shear node is the convergent node and evening wind shear node is the divergent node. The present intermediate layer appeared along with the ion divergent node of the semidiurnal tidal mode S(2,4). It is difficult to explain the present case by the classic wind shear model. But there were some cases that intermediate layers was observed in the evening.

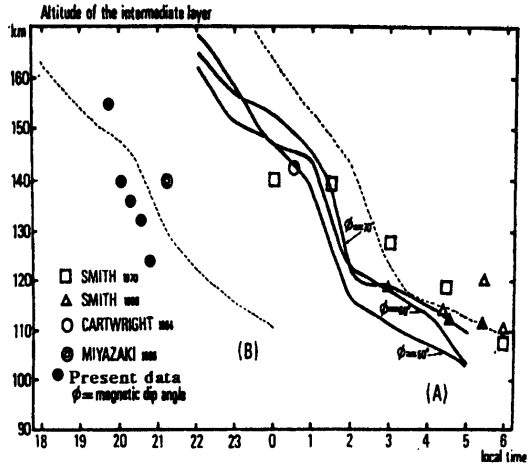

Fig. 6-6: The altitude of the intermediate layers observed by sounding rockets compared with the altitude of the ion convergent or divergent nodes; Dashed line shows S(2,4) mode wind: Solid line shows S(2,4) mode plus Sq-field drift effect (modified from Fujitaka [1973]).

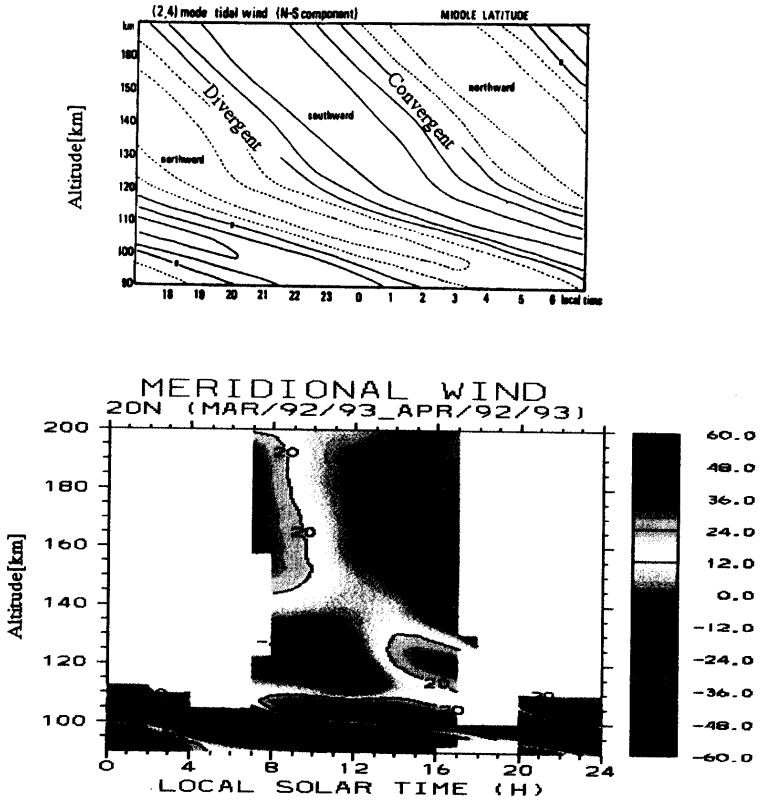

Fig. 6-7: Calculated iso-velocity contour map(top) of semidiurnal S(2,4) mode [Fujitaka, 1973] compared with observation by UARS HARDI [modified from the picture in UARS home page].

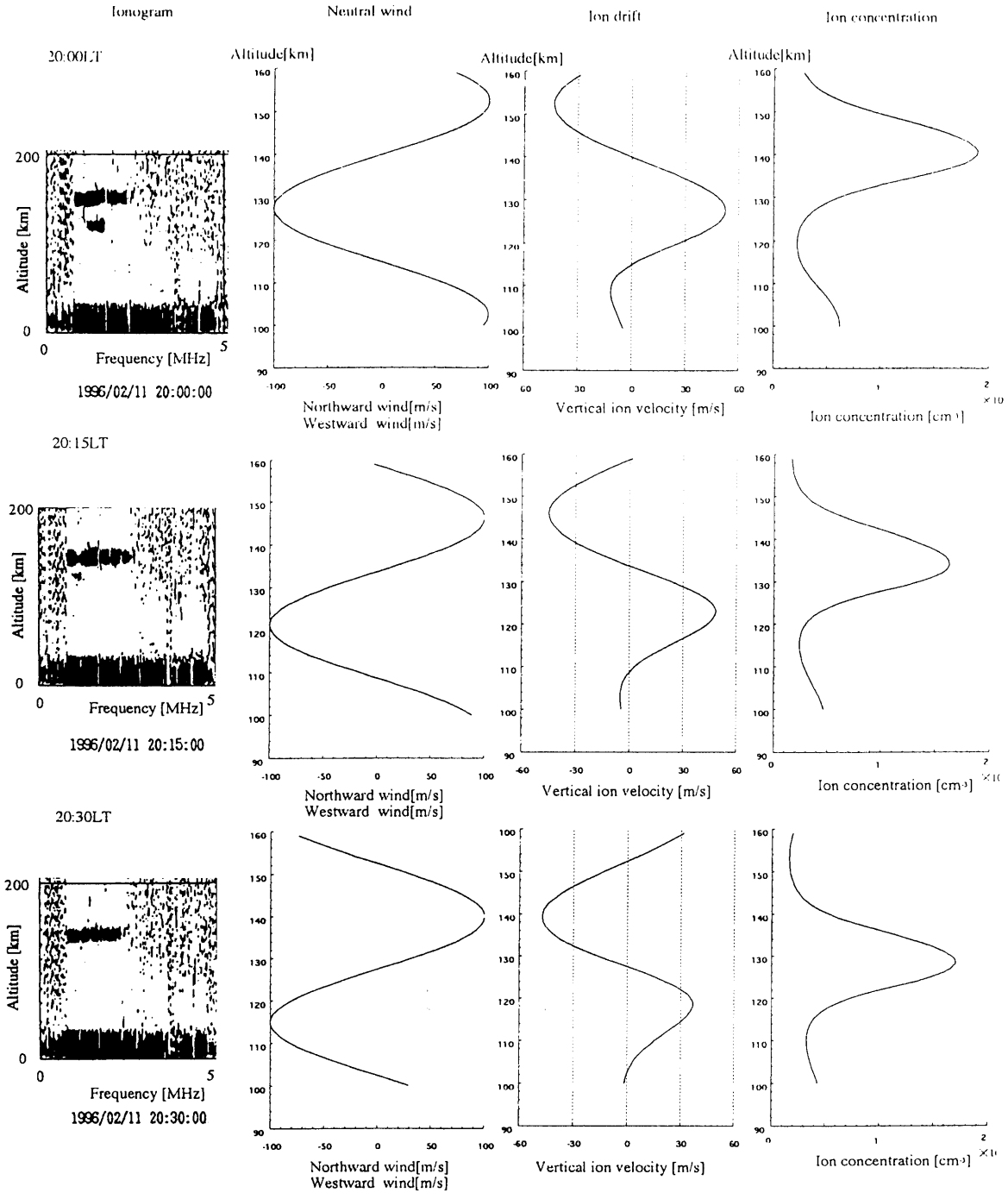

Fig. 6-8: Numerical results of the intermediate layers.

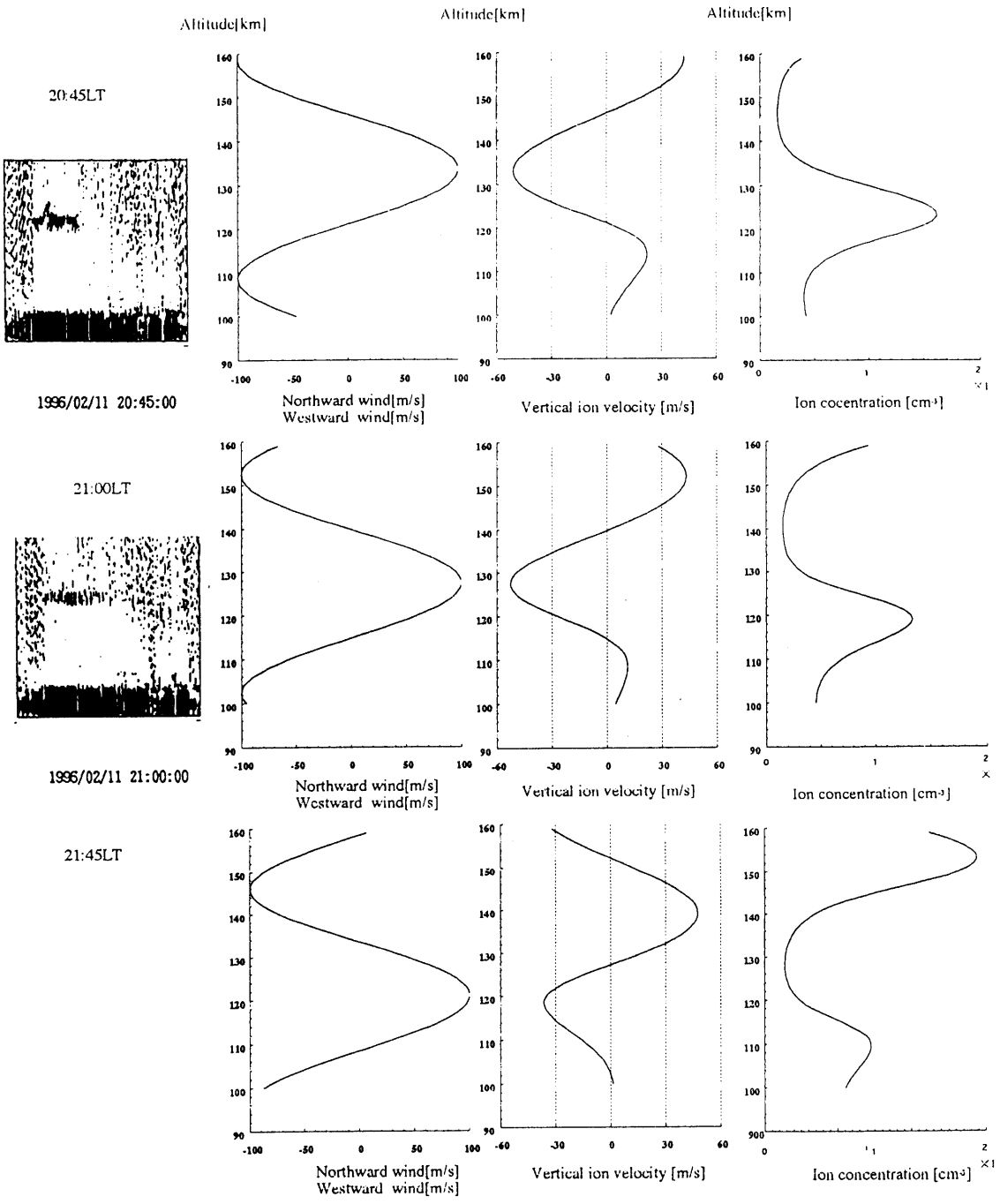

Fig. 6-8: Numerical results of the intermediate layers (Continued from previous page).

VI-2-3 Model calculation

A one-dimensional model calculation is introduced. For the present calculation, intermediate layer is thought to be formed at the convergent node of the large-scale wind field. The ion drift velocity induced by neutral wind is introduced by Chimonas [1973]. The vertical ion drift velocities are determined by both the neutral winds and the electric fields. For simplicity, we neglect the effect of the electric fields, that means ion velocities equal to electron velocities. The neutral vertical wind effect which was neglected in Chimonas[1973] is also included in the present study.

$$w_i = -V_x \frac{Q_i^2}{1+Q_i^2}\cos I \sin I - V_y \frac{Q_i}{1+Q_i^2}\cos I + V_z \frac{(1+\sin^2 I Q_i^2)}{1+Q_i^2} \tag{6-9}$$

Define a right-handed coordinate system with z vertically upward and x to the magnetic north. Where V_x, V_y and V_z are the meridional, zonal and vertical wind velocity respectively, I is magnetic dip angle and Q_i is the ratio of the ion gyro-frequency to the ion - neutral collision frequency as

$$Q_i = \frac{eB}{m_i \nu_i} \tag{6-10}$$

Q_i increases with altitude corresponding to density decreasing with altitude, and passes through unity at a height of about 118km above earth's surface. Therefore Q_i is described as

$$Q_i = e^{z/H} \tag{6-11}$$

where z is measured in kilometers from the altitude 120km and H is scale height [km]. This approximation is the same as used by Chimonas [1973]. Equation (6-9) denotes the northward wind or the westward wind induce down ward ion drift. Equation (6-9) denotes also altitude dependence of the relative weighting of the meridional and zonal components through the factor of Q_i. Above 120km, Q_i is much greater than unity, therefore the meridional component is dominant because ion drift velocity is dependent on meridional wind by Q_i squared in Equation (6-9). But below 120km, zonal wind is dominant because Q_i is smaller than unity. That is why the intermediate layer is usually induced by the meridional wind shear and usually disappears at 120km while typical Sporadic E layer which is usually observed at $\sim$100km is induced by the zonal wind shear. We assumed V_x and V_y as sinusoidal functions in altitude with a vertical wavelength of 50km in accordance with the observed temperature difference from MSIS model (Figure 5-14) and the amplitude of 100m/s. The amplitude is in accordance with the value in Figure 6-4. The continuity equation of the ion is

$$\frac{\partial n_i}{\partial t} + \frac{\partial}{\partial z}(n_i w_i) = P - L \tag{6-12}$$

where n_i is total ion density and W_i is vertical ion velocity. P and L is production rate and loss rate of ion respectively. Because NO is dominant in the region of layer formation, NO^+ concentration is approximately equal to the electron concentration. Thus the loss rate is proportional to the square of electron concentration.

$$L = \alpha [e]^2 \tag{6-13}$$

Where α is the chemical constant of the recombination reaction [Rees 1987],

$$NO^+ + e \rightarrow N + O \qquad \alpha = 4.2 \times 10^{-7}(300/T_e)^{0.85} \tag{6-14}$$

The main source of nighttime ionization is ultraviolet radiation in the form of H I Lyman α (121.6nm), H I Lyman β (102.6nm), He I (58.4nm) and He II (30.4nm). The formation of the intermediate layer is almost independent on initial ion concentration profile as the result of the significant vertical ion transport induced by the neutral wind. Thus the same initial ion concentration profile as Osterman et al. [1994] is introduced in this thesis. But the production rate, P is significantly

important in determining the peak ion density of the layer. P is assumed to be the value of 10 $cm^{-3}s^{-1}$. The result are shown in Figure 6-8. The first column shows ionogram above Yamagawa, second column shows assumed meridional and zonal wind field, third column shows vertical ion drift and the last column shows altitude profile of the ion concentration. The same horizontal wind field as the vertical wind as shown in the left panel of Figure 6-5 is assumed for calculation. But the descending rate of 7m/s is also included as a vertical phase velocity of the wave in this case. The enhancement of the ion density occurs at the ion convergent altitude designated in the third column of Figure 6-8. The peak density is 1.8×10^4 cm^{-3} , which agrees with the observation value of 2×10^4 cm^{-3}. The peak density calculated by Osterman, Heelis and Bailey [1994] is 4×10^3 cm^{-3}. Their value was smaller than ours because they introduce smaller production rate of 3 $cm^{-3}s^{-1}$ and smaller wave amplitude of 20m/s than ours. The observed thickness of the layer was about 20km indicated by the impedance probe measurement (Figure 5-5) and by the collector current measurement (Figure 5-4). This fact also agreed with the present calculation of the altitude profile of the ion concentration as shown in Figure 6-8. The ion concentration decreases as it is approaching the altitude of 120km as shown in Figure 6-8. It reflects that the meridional wind is no more effective for the ion convergence at 120km. Corresponding to the calculation, the intermediate layer disappeared at the altitude of 120km in the ionogram at 21:00 LT.

We can explain the formation of the intermediate layer without the metallic ion, which is the major ion in the sporadic E layer at lower altitude about 100km , by introducing the horizontal windfield with an amplitude of 100m/s and with a vertical wavelength of 50km. But there is still an open question why the present layer appeared at the probable divergent node of the semidiurnal tide. There might be a interaction between gravity wave and tidal wave.

VI-3 Critical Level of the Gravity Wave

We observed the density perturbation such as shown in Figure 5-8 or Figure 6-10. We can divide the density perturbation into three component : (1) Shock wave disturbance component below 110km. (2) Major tendency of smaller values than MSIS below 135km and of larger value than MSIS above 135km. (3) Minor component of the wave like structure above 120km with the vertical wave length of 5 - 20km. The character (2) probably reflects the large-scale wind field induced by the semidiurnal tide S(2,4) mode. While character (3) is probably attributed to the passage of gravity wave in the observation altitude. The fact that the vertical wavelength become smaller while perturbation amplitude become larger with increasing altitude is similar to the behavior of the gravity wave reaching the *critical level*, where the wave saturates by the interaction between the background mean wind field with the gravity wave itself. Figure 6-9 shows schematic illustration of a wave packet propagating upward toward the critical level [Gossard and Hook, 1975] . The back ground mean wind corresponded to the large-scale tidal wind in the present case. The critical level is defined as the level where the horizontal phase velocity equals to the mean wind velocity.

The upper panel of Figure 6-10 shows the altitude profile of the density perturbation , the same figure as Figure 5-8. As mentioned in Chapter V-3, the densities during rocket descend are significantly lower than MSIS values perhaps because the observation region entered the rocket wake region. Nevertheless even in the wake region, the measurement reflected the background density. Figure 6-10 shows the shape of altitude profile have good mutual relationship between ascent and descend except for shifting of 4km. The lower panel of Figure 6-10 shows plots of the peak and dip of the density perturbation along the cross sectional plane of the rocket flight course. The wave front was determined by drawing lines between correspondent points. Solid line shows the peak and dashed line shows the dips of the wave. The slope of the wave front was determined to be 1/40 , which is equal to the ratio of vertical wavelength to horizontal wavelength along the cross sectional plane of

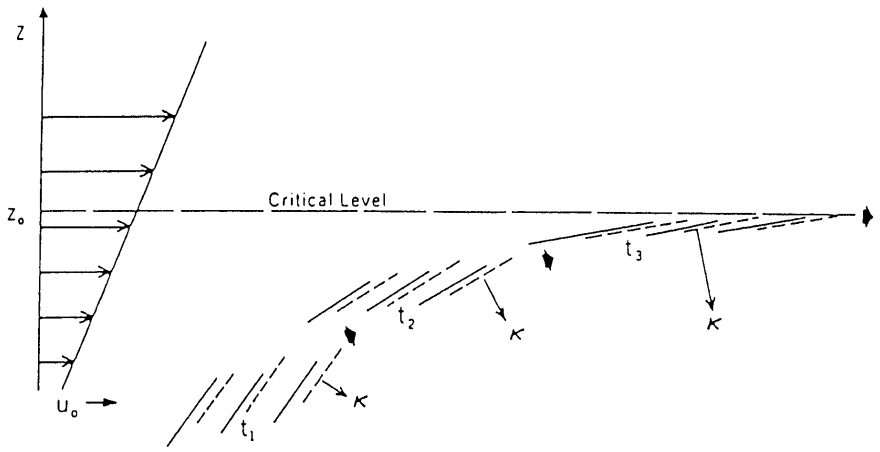

Fig. 6-9: Schematic illustration of a wave packet propagating upward toward a critical level, z_o, at successive times t_1, t_2 and t_3. Dashed lines represent the new positions of equiphase contours a moment after that represented by the solid lines [Gossard and Hook, 1975].

the rocket flight course . Thus

$$\frac{\lambda_z}{\lambda_h} = \frac{k_h}{k_z} \cong \frac{1}{40} \tag{6-15}$$

Where k_h and k_z are horizontal and vertical wavenumber respectively , λ_h and λ_z are horizontal and vertical wavelength respectively . The dispersion relation of the gravity wave is [Andrew and Holton, 1987],

$$\omega^2 = N^2 \frac{{k_h}^2}{{k_z}^2 + 1/4\mathrm{H}^2} \tag{6-16}$$

Where ω is frequency of the gravity wave and N is buoyancy frequency and H is scale height. As H is 10 - 15km at the altitude range of 100 - 150km, the condition of ${k_z}^2 >> 1/4\mathrm{H}^2$ is realized. Therefore Equation (6-16) results in ,

$$\frac{\omega}{N} \approx \frac{k_h}{k_z} \tag{6-17}$$

As N is 0.02 s^{-1} in these altitudes, $\omega = 5 \times 10^{-4}$ s^{-1} is derived. We introduce the horizontal phase velocity defined as $C_p = \omega / k_h$, Equation (6-17) results in

$$k_z = \frac{N}{C_p} \tag{6-18}$$

So we can derive the horizontal phase speed of the gravity wave of 77m/s from the observed vertical wavelength of 20km at the altitude of 125km , where the gravity wave probably was not influenced by the background wind field. When back ground mean flow exists, Equation (6-18) should be described as,

$$k_z = \frac{N}{C_p - U} \tag{6-19}$$

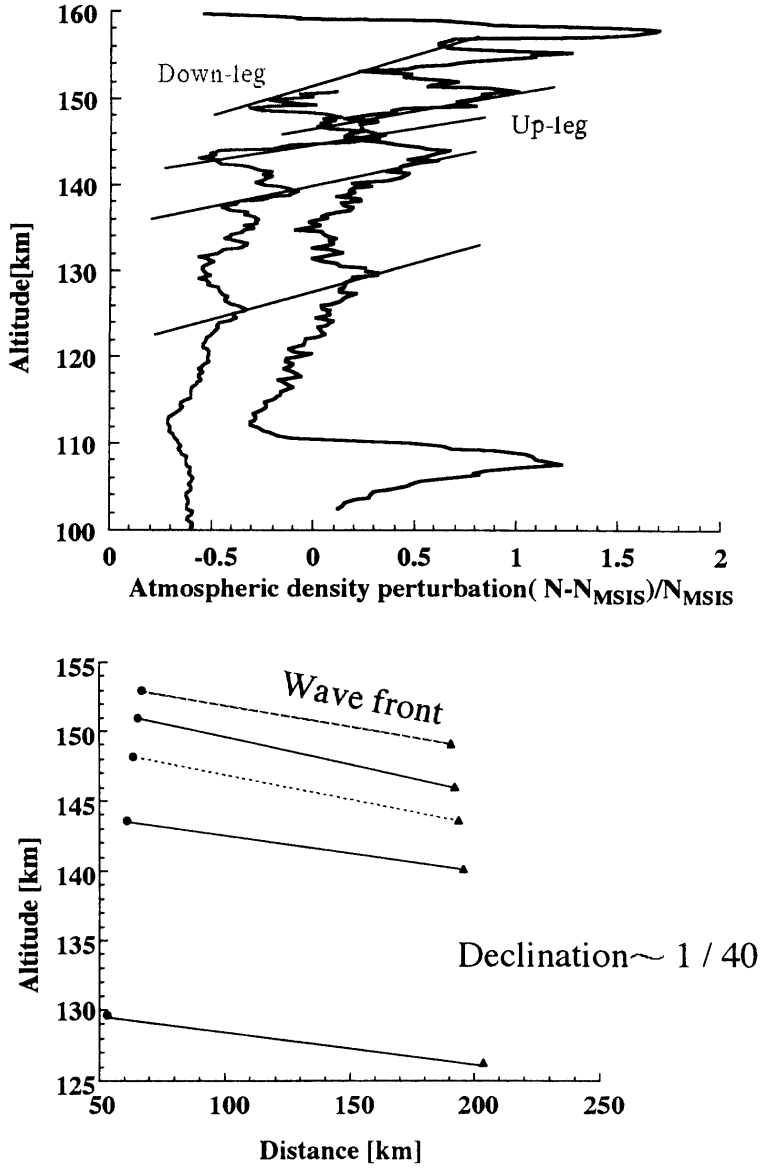

Fig. 6-10: Wave front deduced from number density observation.

where U is the mean flow velocity. When wave reaches the critical level ($C_p - U = 0$), the vertical wave number becomes infinite, and vertical wavelength becomes zero. As the amplitude of the horizontal wind of the semidiurnal tide will be 100m/s, which is larger than the horizontal phase velocity of the present gravity wave , the critical condition will be satisfied where back ground horizontal wind is nearly at the maximum. To see this feature, we can determine the difference ($C_p - U$) from the observed vertical wavenumber by using Equation (6-19). The results are shown in Figure 6-11. The vertical wave number were determined from the density perturbation as shown in upper panel of Figure 6-10. The velocity difference decreased with altitude increasing, perhaps reflects the existence of the vertical wind shear induced by large-scale wind field of semidiurnal tide and its horizontal wind velocity became comparable to the horizontal phase velocity of gravity wave around 150-160km. Horizontal velocity of assumed tidal wind field in the previous calculation in

Chapter VI-1 becomes maximum at the altitude of 152.5km. Thus this altitude perhaps corresponded to the critical level. The velocity difference $(C_p - U)$ become large at the altitude of 135 - 140km , corresponding to the node of the semidiurnal wind. Therefore the present result is consistent with the assumed large-scale tidal wind deduced from the number density or temperature measurement.

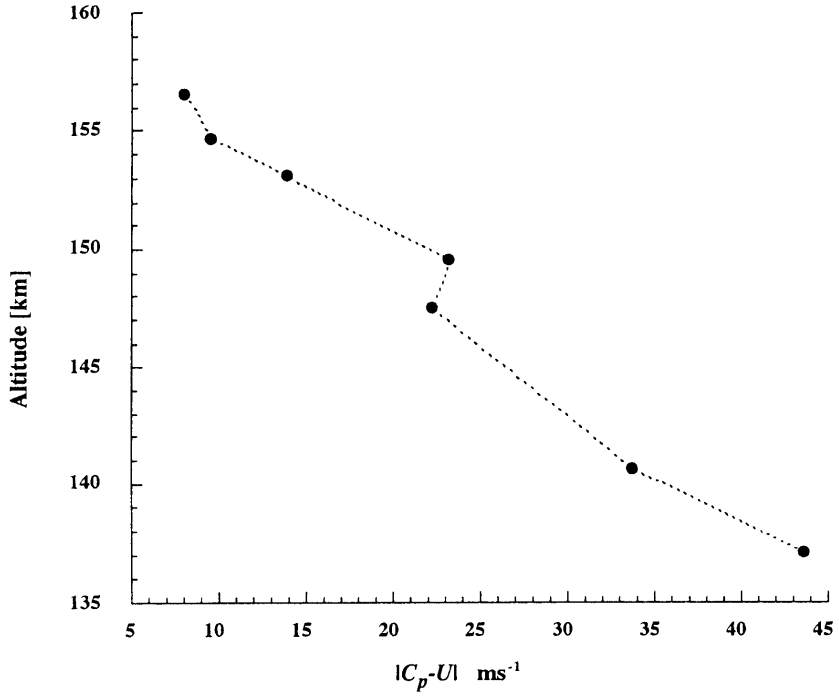

Fig. 6-11: Difference of the phase velocity and the mean wind velocity deduced from the vertical wavelength.

CONCLUDING REMARKS

We have developed a rocket-borne instrument to simultaneously observe the vibrational temperature , rotational temperature and number density of molecular nitrogen. We obtained electron beam induced luminescence of N_2^+ by using a modern technology, that is, we used a 768 channel image sensor and measured the complete spectrum profile. The measurement technique have not been well established before and this method was applied to atmospheric temperature measurement only twice before us. One was rotational temperature measurement by Deleeuw [1972] and the other was vibrational temperature measurement by O'neil [1974]. Therefore we carefully examined the measurement technique , especially for the secondary electron effect to vibrational temperature measurement and for the effect of the shock wave disturbance effect to rotational temperature and number density measurement. We calculated the synthetic spectrum and fitted to observation data, which enable us to determine rotational temperature and vibrational temperature from the rotationally

unresolved spectrum . The error of rotational temperature was about 10K at the gas pressure of simulated altitude of 100km by this spectral fitting method. We made a special calibration system for vibrational temperature measurement, which realized the gas environment of high vibrational temperature and of relatively low rotational temperature simultaneously in order to avoid overlap of 1NG(0,1) band on 1NG(1,2) band. We obtained good agreement of temperature indicated by the thermocouple and vibrational temperature determined from the photospectroscopy.

The instrument was flown abroad a sounding rocket S-310-24 at the Kagoshima Space Center in Japan on February 11 1996 at 20:00 JST. The measurement was successful and we obtained the altitude profile of rotational temperature and number density and the upper limit of vibrational temperature of molecular nitrogen. Density measurement was affected by the shock wave disturbance below 110km but the values above that altitude showed reasonable agreement with MSIS values. In detail, density perturbation $(N-N_{MSIS})/ N_{MSIS}$ showed two kinds of structures diffrenent in vertical scale. The major structure shows that density was lower than MSIS value below around 140km, but higher than MSIS value above around 140km. Fine structure shows wave structure with vertical wavelength of 20km at 130km altitude. But the wavelengths became smaller while perturbation amplitude became larger with increasing altitude. This fact might show the behavior of the Internal Gravity Wave propagating upward into the critical level where the wave saturated by the interaction between the background mean wind and gravity wave wind filed itself. Rotational temperature was determined from 1NG(0,1) band and 1NG(0,0) band coincidentally, and these two temperatures agreed below 120km on rocket ascent. But at the higher altitude, the fitting error of 1NG(0,1) band became larger because of low signal - to - noise ratio of the spectra , Tr obtained from 1NG(0,1) band permitted any conclusion at these altitudes. On the contrary, Tr obtained from 1NG(0,0) band was meaningful even in the altitude range of 120 - 150km, and it showed a wavy structure with the vertical wavelength of about 50km. This value was similar to that of semidiurnal tide S(2,4) mode. The number density measurement and rotational temperature measurement were consistent not only in the light of ideal gas low but also in the light of hydro-static equilibrium.

Vibrational temperature was determined to be 400K with upperlimit of 800K at 100km, 800K with upperlimit of 1000K at 130km and 1000K with upperlimit of 2000K at 150km.

At lower altitudes, in the range of 100 - 110km, secondary electrons were produced much and affected the vibrational temperature measurement. But we carefully avoid the spectra contaminated with the secondary excitation process and then determined the values of vibrational temperature from the spectra purely excited by primary beam electrons. The upper limit did not contradict with past calculations done in 80's and 90's. It meant there was no special vibrational excitation mechanism of N_2 , except for previously proposed mechanisms by recent researchers.

We believe that the rotational temperature we measured is more reliable than that of Deleeuw [1972], because they obtained the rotational temperature from the outputs of the only two photomultipliers with the interference filters. Also, our measurement of the vibrational temperature is much reliable than that of O'Neil [1974], because they did not take into account the effect of low energy electrons on the measurement of vibrational temperature, as well as overlapping effect between 1NG (0,1) and 1NG (1,2).

In addition, the ionized intermediate layer was also observed at altitude of 140km during rocket ascent. The layer appeared not only at the intersection of the observed temperature with MSIS values but also at the intersection of the observed number density with MSIS values. This fact suggested the sinusoidal wind field of semidiurnal tide had a node at the 140km , which induced the ion convergence and consequently formed the ionized intermediate layer.

As mentioned above we have established a powerful instrument to detect in situ the neutral atmosphere parameter which has been difficult to measure directly so far, in spite of its significant importance for the thermosphere dynamics.

ACKNOWLEDGMENTS

The author would like to express his sincere thanks to Prof. Ogawa for his discussion of development activity especially for the technique of the photospectroscopy, and Prof. Mukai for his discussion of the technique of the electron gun and of high-voltage circuit design. The authors also express his thanks to Porf. Ichikawa and Dr. Nakajima for discussion of the electron impact excitation phenomena of molecules, and Prof. Abe for the discussion of the shock wave in the supersonic flow. The authors also express their thanks to Dr. Raghavarao and Dr. Imamura for discussion of the atmospheric wave phenomenon. The authors also express their thanks to all technicians in the Institute of Space and Astronautical Science (ISAS): Mr. Watanabe who is responsible for the impedance probe, Mr. Sato who helped the authors with producing the electron gun electrodes, Mr. Hongou who helped the authors with the supersonic wind tunnel test, and Mr. Aihara who helped the authors with the Space chamber experiments. The authors are indebted to all the staff of ISAS for conducting a sounding rocket experiment. The authors also express their thanks to their colleague: Mr. Noda, Mr. Fukuyama and Miss Okita for their countless efforts during development activities and on rocket launching. The instrument was manufactured by AD electronic company and an electron gun was designed by Apco Co. Ltd.

REFERENCES

Akmaev R. A., J. M. Forbes and M. E. Hagan, Simulation of tides with a spectral mesosphere / lower thermosphere model, *Geophys. Res. Lett.*, **23**, 2173 - 2176, 1996.

Amemiya, H., K. Oyama and K. Hirao, Observation of the mid-latitude ionosphere, *Planet. Space. Sci.*, **33**,875 - 890, 1985.

Andrew, D.G., J. R. Holton and C. B. Leovy, *Middle atmosphere dynamics*, ACADEMIC PRESS, *INC.*, 1987

Axford W. I., D. M. Cunnold and L. J. Glesson, Magnetic field variations in temperate zone sporadic-E layers, *Planet. Space. Sci.*, **14**, 909 - 919, 1966.

Axford W. I., The wind shear theory of the formation of temperate zone sporadic E layers, Space Res. Ⅶ, 126 - 134,

Bates, D. R., 'The intensity distribution in the nitrogen band systems emitted from the earth's upper atmosphere, *Proc. Roy. Soc (London)*, **196,** 217 - 250, 1949.

Barth, C. A., and F. G. Epavier, A method of measuring the temperature of the lower thermosphere, *J. Geophys. Res.*, **98**, 9437 - 9441, 1993.

Bertin, F., J. Testud, and L. Kersley, and P. R. Rees, The meteorological jet stream as a source of medium scale gravity waves in the thermosphere: An experimental study, *J. Atmos. Terr. Phys.*, **40**, 1161 - 1189, 1978.

Breig, E. L., M. E. Brennan, and R. J. McNeal, Effect of atomic oxygen on the N_2 vibrational temperature in the lower thermosphere , *J. Geophys. Res.*, 78, 1225 - 1228, 1973.

Bills, R. E., and C. S. Gardner, Lidar observations of the mesopause region temperature structure at Urbana, *J. Geophys. Res.*, **98**, 1011 - 1021, 1993.

Bird, G. A., Aerodynamic effects on atmospheric composition measurements from rocket vehicles in the thermosphere, *Planet. Space. Sci.*, **36**, 921 - 926, 1988.

Bristow W. A. and B. J. Watkins, Numerical simulation of the formation of thin ionization layers at high latitudes, *Geophys. Res. Lett.*, **18**, 404 - 407, 1991.

Broadfoot, A. L. and D. M. Hunten, N_2^+ emission in the twilight, *Planet. Space. Sci*, **14**, 1303 - 1319, 1966.

Broafood, A. L., Resonace scattering by N_2^+, *Planet. Space. Sci*, 15, 1801 - 1815, 1967.

Borst, W. L., and E. C. Zipf, Cross section for electron-impact excitation of the (0, 0) first negative band of N_2^+ from threshold to 3 k ev, Phys. Rev., **A1**, 834 - 840, 1970.

Burns, D. J., F. R. Simpson, and J. W. Mocconkey, Absolute cross sections for electron excitation of the second

positive bands of nitrogen, J. Phys., **B2**, 52 - 64, 1969.

Chimonas G. and W. I. Axford, Vertical Movement of Temperate-Zone Sporadic E layers, *J. Geophys. Res.*, **73**, 111-117, 1968.

Chimonas G., Enhancement of Sporadic E by Horizontal Transport within the Layer, *J. Geophys. Res.*, **76**, 4578 - 4586, 1971.

Chimonas, G., Wind component exchange and the rapid vertical movement of a sporadic E layer, *J. Geophys. Res.*, **78**, 5636 - 5639, 1973.

Chiu Y. T. and B. K. Ching, The response of atmospheric and lower ionospheric layer structures to gravity waves, *Geophys. Res. Lett.*, **5**, 539 - 542, 1978.

Crickmore R. I., A comparison between vertical winds and divergence in the high- latitude thermosphere, Ann. Geophysicae, **11**, 728 - 733, 1993.

Culp G. and A. T. Stair Jr., Effective rotational temperature of N_2^+(3914Å) excited by monoenergetic electrons in a crossed beam, *J. Chem. Phys.*, **1**, 57 - 62, 1967.

Degen V., Modeling of N_2^+ first negative spectra excited by electron impact on N_2, *J. Quant Spectrosc. Radiat. Transfer*, **18**, 113 - 119, 1977.

Degen V., Vibrational Enhancement and the Excitation of N_2^+ and the First Negative System in the High-Altitude Red Aurora and the Dayside Cusp, *J. Geophys.Res.*, **86**, 11372 - 11378, 1981.

Deleeuw, J. H., and W. E. R. Davies, Simultaneous measurement of temperature and density by an electron beam luminescence technique, Small Rocket Instrumentation Techniques, North-Holland Publ. Comp., 144 - 151, 1969.

Deleeuw, J. H.,and W. E. R. Davies, Measurement of temperature and density in the upper atmosphere using an elecron beam, *Can. J. Phys.*, **50**, 1044 - 1051, 1972.

Dick, K. A., W. Beneshe, H. M. Crosswhite et al,. High resolution spectra of bands of the first negative group of ionized molecular nitrogen, *J. Molecular Spectroscopy*, **69**, 95 - 108, 1978.

Doering, J. P., L. Goembel, and J. Yang, Vibrational distribution of N_2^+ $A_2\Pi_u$ from 100 eV electron impact on N_2, *J. Geophys. Res.*, **99**, 3931 - 3933, 1994.

Dothe Hoang and F. von Esse, Rotational temperatures and production mechanisms of some infrared radiators in the daylit terrestrial thermosphere, *J. Geophys. Res,* **101**, 19715 - 19721, 1996.

Dufayard, J., J. M. Negre, and O. Nedelec, Perturbation effects on lifetimes in N_2^+, *J. Chem. Phys.*, **61**, 3614 - 3618, 1974.

Ennis, A. E., G. J. Bailey, and R. J. Moffett, Vibrational nitrogen concentration in the ionosphere and its dependence on season and solar cycle, *Ann. Geophys.*, **13**, 1164 - 1171, 1995.

Fennelly J. A., D. G. Torr, M. R. Torr and S. Yung, Retrival of thermospheric atomic oxygen, nitrogen and temperature from the 732nm emission measured by the ISO on ATLAS 1, *Geophys. Res. Lett.*, **20**, 527 - 530, 19, 1993.

Fennelly J. A. and D. G. Torr, Simultaneous retrieval of the solar EUV flux and neutral thermospheric O, O_2, N_2, and temperature from twilight airglow, *J. Geophys. Res,* **99**, A4, 6483 - 6490, 1994.

Fontanari, J. and D. Alcayde, Observation of neutral temperature tidal-type oscillations in the F_1 region, *Radio Sci.*, **9**, 275 - 280, 1974.

Forbes J. M., Atmospheric Tides 1. Model Description and Results for the Solar Diurnal Component, *J. Geophys. Res.*, **87**, A7, 5222 - 5240, 1982.

Forbes J. M., Atmospheric Tides 2. The Solar and Lunar Semidiurnal Component, *J. Geophys. Res.*, **87**, 5241 - 5252, 1982.

Forbes J. M.,Tidal and planetary waves, in *The upper mesosphere and lower thermosphere: A review of experiment and theory (Geophysical Monograph 87)* edited by R. M. Johson and T. L. Kileen, 67-87, American Geophysical Union, 1995.

Fox J. L. and A. Dalgarno, The Vibrational Distribution of N_2^+ in the Terrestrial Ionosphere, *J.Geophys.Res.*, **90**, 7557 - 7567, 1985.

Fujitaka, K., and T. Tohmatsu, A tidal theory of the ionospheric intermediate layer, *J. Atmos. Terr. Phys.* **35**, 425 - 438, 1973.

Gavrilov N. M., Distributions of the intensity of ion temperature perturbations in the thermosphere, *J. Geophys. Res.*, **100**, 23835 - 23843, 1995.

Gardner C. S., J. D. Shelton, Density Response of Neutral atmosphere layers to gravity wave perturbations, *J. Geophys. Res.*, **90**, 1745 - 1754, 1985.

Gilmore, F. R., R. R. Laher, and P. J. Espy, Franck-Condon factor, r-centroid, electronic transition moments and Einstein cofficient for many nitrogen and oxygen band systems, *J. Phys. Chem. Ref. Data*, **21**, 1005 - 1121, 1992.

Goembel, L., J. Yang., and J. P. Doering, Direct experimental measurement of electron impact ionization-excitation branching ratios 2. Angular distribution of secondary electrons from N_2 at 100eV, *J. Geophys. Res.*, **99**, 17477 - 17481, 1994.

Gossard, E. E. and W. H. Hooke, *Waves in the atmosphere*, 456pp., Elsevier, New York, 1975.

Hall R. I., I. Cadez, M. Landau, F. Pichou and C. Shermann, Vibrational excitation of hydrogen via recombinative desorption of atomic hydrogen gas on a metal surface, *Phys. Rev. Lett.*, **60**, 337 - 340, 1988.

Harris, R. D., and G. W. Adams, Where does the $O(^1D)$ energy go?, *J. Geophys. Res.*, **88**, 4918-4927, 1983.

Harper R. M., Some results on mean tidal structure and day-to-day variability over Arecibo, *J. Atmos. Terr. Phys.*, **43**, 255 - 262, 1981.

Hedin, A. E., MSIS-86 Thermospheric model, *J. Geophys. Res.*, **92**, 4649 - 4662, 1987.

Hernandez, G., Vertical motions of the neutral thermosphere at midlatitudem, *Geophys. Res. Lett.*, **9**, 555 - 557, 1982.

Hernandez, S. P., P. J. Dagdigian, and J. P. Doering, Experimental verification of the breakdown of the electric dipole rotational selection rule in electron impact ionization-excitation of N_2, *J. Chem. Phys.*, **77**, 6021 - 6026, 1982.

Herzberg, G., *Molecular spectra and molecular structure 1 Spectra of diatomic molecules*, D. Van Nostrand Company, Inc., 208, 1950.

Herzberg, G., *Molecular spectra and molecular structure 4 Constants of diatomic molecules*, D. Van Nostrand Company, Inc., 1979.

Hines, C. O., Internal atmospheric gravity waves at ionospheric heights, *Can. J. Phys.*, **38**, 1441 - 1481, 1960.

Hines C. O., Dynamical heating of the upper atmosphere, *J. Geophys.. Res.*, **70**, 177 - 183, 1965.

Hodges R. R., Generation of Turbulence in the Upper Atmosphere by Internal Gravity Waves, *J. Geophys. Res.*, **72**, 3455 - 3458, 1967.

Hook W H., Radar Thomson scatter observations of E-region temperatures interpreted as revealing reversible heating by atmospheric tides, *J. Geophys.. Res.*, **74**, 1870 - 1872, 1969.

Hooke W. H., Elctron, ion and neutral-gas temperatures in tempearate latitude sporadic-E layers, *Planet. Spce Sci.* **17**, 737 - 748, 1969.

Huang, C. S., and M. C. Kelley, Numerical simulations of gravity wave modulation of midlatitude sporadic E layers, *J. Geophys. Res.*, **101**, 24533 - 24543, 1996.

Hunter, W. W. Jr., Investigation of temperature measurements in 300° to 1100°K low-density air using an electron beam probe, NASA TN D-4500 (internal report), 1968.

Hunten, D. M. and G. G. Shepherd, Vibrational temperatures from second positive bands, *J. Atmos. Terr. Phys.*, **6**, 64 - 65, 1955.

Imamura T., K. Kita, N. Iwagami and T. Ogawa, Gravity wave Characteristic Derived from Structured Atomic Oxygen Profile and Multiple Es Layers, *J. Geomag. Geoelectr.*, **47**, 961 - 972, 1995.

Johnson F. S.and B.Gottlieb, Composion changes in the lower thermosphere, Space Res, IV, 442 - 446, 1969.

Kane T. J., C. S. Gardner, Q. Zhou, J. D. Mathews and C. A. Tepley, Lider,radar and airglow observations of a prominent sporadic Na/sporadic E layer event at Arecibo during AIDA-89, *J. Atmos. Terr. Phys.*, **55**, 499 - 511, 1993.

Kawashima T., K.-I.Oyama, K.Suzuki, S.Tei, N.Iwagami, A Measurement of vibrational, rotational temperature of N2 and the number density in the lower thermosphere - Instrumentation and preliminary results, *Adv. Space Res.*, **19**, 663 - 666, 1997.

Kawashima T., K.-I. Oyama, K. Suzuki, S. Tei, N. Iwagami,Measurement of vibrational temperature of N_2 at the height of $\sim$ 100km, Instrumentation and preliminary results, *Proceedings of the 20th ISTS*, 96-j-10, 1996.

Kirwood S., Lower thermosphere mean temperatures, densities, and winds measured by EISCAT: Seasonal and solar cycle effects, *J. Geophys. Res.*, **101**, 5133 - 5148, 1996.

Kumer, J. B., Atmospheric CO_2 and N_2 vibrational temperatures at 40-to 140-km altitude, *J. Geophys. Res.*, **82,** 2195 - 2202, 1977.

Kummler, R. H., and M. H. Bortner, Vibrational temperature in the E and F regions, *Space Res.* **XII,** 711 - 719, 1972.

Knudsen, W. C., and G. W. Sharp, Evidence for temperature stratification in the E region, *J. Geophys. Res.*, **70**, 143 - 160, 1965.

Lee, J. S., J. P. Doering, T. A. Potemra, and L. H. Brace, Measurements of the ambient photoelectron spectrum from atmosphere explorer: . AE-E measurements below 300 km during solar minimum conditions, *Planet. Space Sci*, **28**, 947 - 971, 1980.

Linson, L.M., Current - voltage characteristics of an electron - emitting satellite in the ionosphere, *J. Geophys. Res* ., **74**, 2368 - 2375, 1969.

Lopez-Puertas, M. and R. Rodrigo, A. Molina and F. W. Taylor, A non-LTE radiative transfer model for infrared bands in the middle atmosphere. I . Theoretical basis and application to CO_2 15 μ m bands, *J. Atmos. Terr. Phys.*, **48**, 729 -748, 1986.

Mathews J. D., Y. T. Morton and Q. Zhou, Observations of ion layer motions during the AIDA campaign, *J. Atmos. Terr. Phys.*, **55**, 447 - 457, 1993.

McNeal, R. J., M. E. Whitson, and G. R. Cook, Temperature dependence of the quenching of vibrationally excited nitrogen by atomic oxygen, *J. Geophys. Res* ., **79**, 1527 - 1531 , 1974.

Miller N. J., J. M. Grebowsky and A. E. Hedin, Equatorial ion composition, 140 -200km, base on Atmosphere Explorer E data, *J. Geophys. Res* ., **98**, 15685 - 15692, 1993.

Minami S. and Y. Takeya, Ion temperature determination in the ionosphere by retarding potential analyzer abroad sounding rocket, *J. Geophys. Res* ., **87**, 713 - 730, 1982.

Moore, J. H., Jr., and John P. Doering, Vibrational excitation in ion-molecule collisions: H^+, H_2^+ , He^+ , N^+, Ne^+, and electrons on N_2 , *Phys. Rev.*, **177** , 218 - 223, 1969.

Muntz, E. P., Static temperature measurement in a flowing gas, *The Phys. Fluids*, **5**, 80-90, 1962.

Nebel H., P. P. Wintersteiner, R. H. Picard, J. R. Winick, and R.D. Sharma, CO_2 non-local thermodynamic equilibrium radiative excitation and infrared dayglow at 4.3 μ m: application to spectral infrared rocket experiment data, *J. Geophys. Res* ., **99**, 10409 - 10419, 1994.

Necrasov A. K., S. L. Shalimov, P. K. Shukla and L. Stenflo, Nonlinear disturbaces in the ionosphere due to acoustic gravity waves, *J. Atmos. Terr. Phys.*, **57**, 737 - 741, 1995.

Newton, G. P., J. C. G. Walker, and P. H. E. Meijer, Vibrationally excited nitrogen in stable auroral red rcs and its effect on ionospheric recombination, *J. Geophys. Res.*, **79**, 3807, 1974.

Nicholls, R. W., Laboratory astrophysics, *J. Quant. Spectrosc. Radiat. Transfer*, **2**, 433 - 439, 1962.

O'neil, R. R. and G. Davidson, Luminous efficiency of electron induced emission in nitrogen, in *Atmospheric Emission*, edited by B. M. McCormac and A. Omholt, 477 - 483, Van Nostrand Reinhold, New York, 1969.

O'neil, R. R., W. R. Pendleton Jr., A. M. Hart, and A. T. Stair, Jr., Vibrational temperature and molecular density of thermospheric nitrogen measured by rocket-borne electron beam induced luminescence, *J. Geophys. Res.*, **79**, 1942 - 1957, 1974.

Opal, C. B., E. C. Beaty, and W. K. Peterson, Table of secondary - electron - production cross section, Atomic Data, Academic Press, **4**, 209 - 253, 1972.

Osterman, G. B. , R. A. Heelis and G. J. Baily, Modeling the formation of intermediate layers at Arecibo latitudes, *J. Geophys. Res.*, **99**, 11357 - 11365, 1994.

Osterman G. B., R. A. Heelis and G. J. Bailey, Effects of zonal winds and metallic ions on the behavior of intermediate layers, *J. Geophys. Res* ., **100**, 7829 - 7838, 1995.

Oyama, K. I. and K. Hirao, Energy gain of supra-thermal electrons form the excited neutral gases, *J. Geomagn.*

Geoelectr., **37**, 913 - 926, 1985.

Oyama, K. I., K. Hirao, P. M. Banks, and P. R. Williamson, Is T_e equal to T_n at the height of 100 to 120km? *Planet. Space Sci.*, **28**, 209 - 211, 1980.

Oyama, K. I., K. Hirao, P. M. Banks, and P. R. Williamson, Non - thermal components of low energy electrons in the ionospheric E- and F- region, *J. Geomagn. Geoelectr.*, **35**, 185 - 200, 1983.

Oyama K-I, T.Kawashima, and K. Suzuki, Rotational temperature of N2 and the number density in the height range of -100km, *Atomic collision Research in Japan 22*, 111, 1997.

Oyama K.-I, T.Kawashima, and K. Suzuki, Vibrational temperature of N2 in the height range of 100 - 140km, will appear in *Progress Report of Atomic collision Research in Japan*, 22, 112, 1996.

Pavlov A. V., Vibrational temperature of N_2 and CO_2 in the mid-latitiude E and D region of the inosphere, *Geomagn. Aeron.*, **27**, 508 - 511, 1987.

Pavlov A. V., A. A. Namgaladze, Vibrationally - Excited Molecular Nitrogen in the Upper Atmosphere (Review), *Geomagn. Aeron.*, **28**, 607 - 620, 1988a.

Pavlov A. V., The role of vibrationally excited nitrogen in the ionosphere,*Pure and Appl. Geophys.*, **127**, 529 - 544, 1988b.

Pavlov A. V., The role of vibrationally excited nitrogen in the formation of the mid-latitude ionisation trough, *Ann. Geophys.*, **11**, 479 - 484, 1993.

Pavlov A. V., The role of vibrationally excited nitrogen in the formation of the mid-latitude negative ionospheric storms, *Ann. Geophys.*, **12**, 554 - 564, 1994a.

Pavlov A. V.,The role of vibrationally excited oxygen and nitrogen in the D and E regions of the ionosphere, *Ann. Geophys.*, **12**, 1085 - 1090 ,1994b.

Pavlov A. V.,Determination of the molecular nitrogen vibrational temperature in the auroral region using intensity measurements of the N_2^+ ion firt negative band system, *Geomagn. Aeron.* **34**, 306 - 310, 1994c.

Pavlov A. V. and M. J. Buonsanto,Using Steady-State Vibrational Temperatures to Model Effects of N_2^* on Calculations of Electron Densities, *J. Geophys. Res* , **101**, 26941 - 26945, 1996.

Pendleton, W. R., Jr., and R. R. O'Neil, Departure of N_2^+ ($B^2\Sigma_u^+$, v'=2 and 3) vibrational population from Franck - Condon prediction in the case of energetic e-$N_2(X^1\Sigma_g^+, v=0)$ collisions, *J. Chem. Phys.*, **56**, 6260 - 6262, 1972.

Phillips, D. M., Determination of gas temperature form unresolved bands in the spectrum from nitrogen discharge, *J. Phys. D: Appl. Phys.*, **8**, 507 - 520, 1975.

Pitteway M. L. V., C. O. Hines, The Reflection and Ducting of Atmospheric Acoustic - Gravity Waves, *Can. J. Phys.*, **43**, 2222 - 2243, 1965.

Raghavarao R. W. R. Hoegy, N. W. Spencer and L. E. Wharton, Neutral Temperature Anomaly in the Equatorial Thermosphere - A Source of Vertical Winds, *Geophys. Res. Lett.*, **20**, 1023 - 1026, 1993.

Raghava Reddi, C. and Geetha Ramkumar, Climatologies of tidal winds in the radio-meteor region over Trivandrum (8N), *J. Atmos. Terr. Phys.*, **59**, 1757 - 1777, 1997.

Rees M. H., *Physiscs and chemistry of the upper atmosphere*, Cambridge University Press, 1987.

Ronald H. Wand, Lower Thermospheric Structure From Millstone Hill Incoherent Scatter Radar Measurements 1. Daily Mean Temperature, *J. Geophys. Res.*, **88**, 7201 - 7209, 1983.

Richards P. G., D. G. Torr and Wedad A. Abdou, Effects of vibrational enhancement of N_2 on the cooling rate of ionosphere thermal electrons, *J. Geophys. Res.*, **91**, 304 - 310, 1986a.

Richards P. G. and D. G. Torr, A factor of 2 reduction in theoretical F2 peak electron density due to enhanced vibrational excitation of N_2 in summer, *J. Geophys. Res.*, **91**, 11331 - 11336, 1986b.

Rinsland C. P., M. R. Gunson, R. Zander and M. Lopez - Puertas, Middle and upper aatmosphere pressure-temperature profiles and the abundances of CO_2 and CO in the upper atmosphere from ATMOS/Spacelab 3 observation, *J. Geophys. Res.*, **97**, 20479 - 20495, 1992.

Rishbeth, H., R.J. Moffett, and G. J. Bailey, Continuity of air motion in the mid latitude thermosphere, *J. Atmos. Terr. Phys.*, **31**, 1035-1047, 1969.

Richmond A. D., E. C. Ridley, and R. G. Roble, A Thermosphere/Ionosphere General Circulation Model with

Coupled Electrodynamics, *Geophys. Res. Lett.*, **19**, 601 - 604, 1992.

Salah J. E., Variability of winds and temperatures in the lower thermosphere, *J. Atmos. Terr. Phys.*, **56**, 1327 - 1337, 1994.

Sharma R. D., Hoang Dothe, F. von Esse, V. A. Kharchenko, Y. Sun, and A. Dalgarno, Production of vibrationally and rotationally excited NO in the night time terrestrial thermosphere, *J. Geophys. Res*, **101**, 19707 - 19713, 1996.

Shaw M. and J. Campos, Emission cross section of the second positive and first negative systems of N_2 and N_2^+ excited by electron impact, *J. Quant. Spectrosc. Radiat. Transfer*, **30**, 73 - 76, 1983.

Schmeltekopf. A. L., F. C. Fehsenfeld, G. I. Gilman, and E. E. Ferguson, Reaction of atomic oxygen ions with vibrationally excited nitrogen molecules, *Planet. Space Sci.*, **15**, 401 - 406, 1967.

Shemansky, D. E., and A. L.Broadfoot, Excitation of N_2 and N_2^+ System by Electrons -1 Absolute transition probabilities, *J. Quant. Spectrosc. Radiat . Transfer.*, **11**, 1385 - 1400, 1971.

Shen, J. S., W. E. Swarts, and D. T. Farley, Ionization layers in the nighttime E region valley above Arecibo, *J. Geophys. Res.*, **81**, 5517 - 5526, 1976.

Senft and Gardner, Seasonal variability of gravity waves, *J. Geophys. Res.*, **96**, D9, 17229 - 17264, 1991.

Slanger T. G. and G. Black, Electronic-to-vibrational energy transfer efficiency in the $O(^1D)$-N2 and $O(^1D)$-CO systems, *J. Cehm. Phys.*, **60**, 468 - 477, 1974.

Smith L.G., A sequence of rocket observations of night-time sporadic-E, *J. Atmos. Terr. Phys.*, **32**, 1247 - 1257, 1970.

Szuszczewicz E. P.,R. G. Roble, P. J. Wilkinson, R. Hanbaba, Coupling mechanisms in the lower ionospheric-thermosphric system and manifestation in the formation and dynamics of intermediate and descending layers, *J. Atmos. Terr. Phys.*, **57**, 1483 - 1496, 1995.

Swift W. R., D. G. Torr, P. G. Richards, P. P. Bhatt, C. M. Hamilton, M. R. Torr and R. L. Goodwin, Twilight Observations and Modeling of the N_2^+ First Negative Bands, presented at the Fall Meeting of the American Geophysical Union, San Francisco, California, December 4-8, 1989; *Abstract published in EOS*, 70, 1249, 1989.

Taylor R. L. and S. Bitterman, Survey of vibrational relaxation data for processes important in the CO_2-N_2 laser system, *Rev. Mod. Phys.*, 41, 26 - 47, 1969.

Torr, M. R. and D. G. Torr, The role of metastable species in the thermosphere, *Rev. Geophys.*, **20**, 91 - 159, 1982.

Torr M. R., D. G. Torr, T. Chang, P. G. Richards, The N_2^+ First Negative System in the dayglow from Spacelab 1, *J. Geophys. Res.*, **97**, 17075 - 17095, 1992.

Torr M. R., D. G. Torr, T. Chang, P. G. Richards, T. W. Baldridge, J. K. Owens, H. Dougani, C. W. Fellows, W. Swift, S. Yung, and J. Hladky, The First Negative Bands of N_2^+ in the Dayglow from the ATLAS 1 Shuttle Mission, *Geophys. Res. Lett.*, **20**, 523 - 526, 1993.

Vallance Jones, A., and D. M. Hunten, Rotational and vibrational intensity distribution of the first negative N_2^+ bands in sunlit auroral rays, *Can. J. Phys.*, **38**, 458 - 476, 1960.

Vincenti W. G. and C. H. Kruger, Jr., *Intorduction to physical gas dynamics*, Krieger Publishing Comapny, Malabar, Florida, 1965.

Vlaskov, B. A., and K. Henriksen, Vibrational temperature and excess vibrational energy of molecular nitrogen in the grount satate derived form N_2^+ emission bands in aurora. *Planet Space Sci* , **33**, 141 - 145, 1985.

Walker, C. G., Electron and nitrogen vibrational temperature in the E-region of the ionosphere, *Planet. Space. Sci.*, **16**, 321 - 327 , 1968.

Walker, C. G., R. S. Stolarski, and A. F. Nagy, The vibrational temperature of molecular nitrogen in the thermosphere, *Ann. Geophys.*, **25**, 831 - 839, 1969.

Waltersheid R. L., Dynamical cooling induced by dissipating internal gravity waves, *Geophys. Res. Lett.*, **8**, 1235 - 1238, 1981.

Wand R. H., Radar Thomson scatter obsevations of temperature and ion neutral collision freqeuncy in the E region, *J. Geophys., Res.*, **73**, 6370 - 6372, 1968.

Wand R. H., Semidiurnal tide in the E region from incoherent scatter measurements at Arecibo, *Radio Sci.*, **7**, 641 - 652, 1976.

Wand R. H., Lower Thermospheric Structure from Millstone Hill Incoherent Scatter Radar Measurement 1. Daily Mean Temperature , *J. Geophys. Res.* **88,** 7201 - 7209, 1983.

Ward W. E., Observations of the two-day wave in WINDII data during January, 1993., *Geophys. Res. Lett.*,**23**, 2923 - 2926, 1996.

Wardill P. and F. Jacka, Vertical motins in the thermosphere over Mawson, Antarctica, *J. Atmos. Terr. Phys.*,**48**, 289 - 292, 1986.

Whitehead J. D., Recent work on mid-latitude and equatorial sporadic-E, *J. Atmos. Terr. Phys.*, **51**, 401 - 424, 1989.

Wilkinson P. J., E. P. Szuszczewicz, R. G. Róble,Measurements and Modelling of intermediate, descending, and sporadic layers in the lower ionosphere: results and implications for global-scale ionospheric-thermospheric studies, *Geophys. Res. Lett.*, **19**, 95 - 98, 1992.